CHARACTERIZATION OF A LAB-SCALE POLYMETHYLMETHACRYLATE AND GASEOUS OXYGEN HYBRID ROCKET

A Thesis
Submitted to the Graduate Faculty
of the
North Dakota State University
of Agriculture and Applied Science

By

Porter Wilkins Dixon

In Partial Fulfillment of the Requirements
for the Degree of
MASTER OF SCIENCE

Major Department:
Mechanical Engineering

November 2022

Fargo, North Dakota

North Dakota State University
Graduate School

Title

Characterization of a Lab-Scale Polymethylmethacrylate and Gaseous Oxygen Hybrid Rocket

By

Porter Wilkins Dixon

The Supervisory Committee certifies that this ***disquisition*** complies with North Dakota State University's regulations and meets the accepted standards for the degree of

MASTER OF SCIENCE

SUPERVISORY COMMITTEE:

Jordi Estevadeordal
Chair

Bora Suzen

Jeremy Straub

Approved:

11/18/2022
Date

Chad Ulven
Department Chair

ABSTRACT

Hybrid rockets are a type of chemical rocket propulsion where the reactants are in different phases. Historically, hybrid rockets have been underutilized in the aerospace industry. However, due to their simple nature, they are easy to construct and test. Research on hybrid rocket propulsion was conducted using optically clear polymethylmethacrylate and gaseous oxygen with a nozzle designed to achieve Mach 2. Characterization was performed using combustion simulations available from NASA and measurements with pressure transducers, thermocouples, a load cell, and high-speed cameras. The test stand and hybrid rocket itself were designed by previous senior design groups. From the results, performance parameters such as the characteristic velocity, thrust coefficient, and specific impulse were calculated for various test times and oxidizer mass flow rates. Testing has shown that the rocket can be run safely and successfully numerous times.

ACKNOWLEDGMENTS

None of the experimental work reported on in this thesis would be possible without the contributions of several individuals. I would like to thank the following: Joshua Yurek, a member of the original design team, who helped design and construct the test stand and the hybrid rocket. He also assisted with testing the rocket and gave suggestions on how to improve the test stand; William Refling for his assistance in conducting hot-fires; Charles Fabijanic for his help in conducting tests, and for setting up and operating the imaging equipment that was used in several of the test fires; Emily Balluff for her help with testing and data processing; Steve Johnson from the North Dakota State College of Science, who generously machined the graphite nozzles free of charge; Rob Sailer and Francisco Valenzuela for machining both the acrylic fuel grains and nozzles, and the Mechanical Engineering Office, especially Kimberly Carlson, for processing countless part orders. Special thanks to my advisor, Dr. Jordi Estevadeordal, for taking me on as a graduate student, and for giving me the opportunity to gain valuable experience in propulsion testing. Finally, I'd like to thank my family for their support throughout my graduate studies.

TABLE OF CONTENTS

LIST OF TABLES

LIST OF FIGURES

LIST OF ABBREVIATIONS

PMMA .....Polymethylmethacrylate

MMA.....methyl methacrylate

GOx.....gaseous oxygen

LH2 .....liquid hydrogen

LOx .....liquid oxygen

RPDT .....Rocket Propulsion Design Team

CD.....converging-diverging

LIST OF SYMBOLS

(O/F) .....oxidizer-to-fuel ratio

$\dot{m}_f$ .....mass flow rate, fuel

$\dot{m}_o$ .....mass flow rate, oxidizer

G_o .....oxidizer mass flux

$\dot{r}$.....regression rate of fuel grain

ρ_f .....fuel grain density

a.....empirical regression coefficient

A^*.....sonic throat area

A_e.....nozzle exit area

n.....empirical regression coefficient

P_{amb} .....ambient pressure

P_c.....chamber pressure

P_o.....stagnation pressure

R.....specific gas constant

R_i .....initial fuel grain port radius

T_c.....chamber temperature

T_e.....exhaust temperature

T_o.....stagnation temperature

v_e.....exhaust velocity

LIST OF APPENDIX FIGURES

1. INTRODUCTION AND RESEARCH OBJECTIVES

Chemical rocket propulsion is currently the only technology that enables access to outer space and has been for the past 60 years. Chemical rocket propulsion will continue to be the main driver of space activity for at least the next few decades. In general, there are 3 types of chemical rocket propulsion. Solid rockets utilize both a solid fuel and solid oxidizer. Liquid rocket propulsion can be divided into two subtypes. Monopropellant liquid rockets utilize a single chemical propellant that can undergo catalytic decomposition. Bipropellant liquid rockets utilize a liquid fuel and a liquid oxidizer. The last type is a hybrid between solid and liquid rocket propulsion systems. A hybrid rocket utilizes a solid fuel and a fluid oxidizer, such as paraffin wax for the fuel, and gaseous oxygen as the oxidizer. A less common configuration is called the reverse hybrid, which uses a liquid fuel but a solid oxidizer. Of these 3 types, hybrid rockets are the least utilized. Although hybrids haven't seen much use commercially compared to the other types of chemical propulsion, many hybrids have been built, tested, and studied in academic and research settings. Some have undergone flight testing in the form of sounding rockets. (Story & Arves, 2006) They have even been used for manned flights, such as when Scaled Composites' SpaceShipOne made history as the first privately built manned spacecraft to reach space using its hybrid rocket motor (Sharp, 2019).

Through the efforts of several senior design groups and research assistants, North Dakota State University has constructed a lab-scale hybrid rocket that utilizes optically clear polymethylmethacrylate and gaseous oxygen as reactants. Since November 2020, the constructed hybrid rocket has been successfully test fired more than a dozen times, with varying amounts of data collected from each test fire. This thesis will focus on characterizing the performance of the rocket from data collected since November 2020 and compare it to the performance predictions

of the previous senior design group, performance figures in the academic literature, and calculations done in the time between November 2020 to the present. Henceforth, the Rocket Propulsion Design Team (RPDT), which was responsible for the initial design and construction of the rocket as it was in November 2020, will be referred to as “the design team”.

2. THEORY

2.1. Hybrid Rocket Propulsion

The history of hybrid rockets is almost as old as modern rocketry itself. John D. Clark's excellent book, "Ignition!: An Informal History of Liquid Rocket Propellants" tells the story of the first hybrid rocket built in the late 1920's by rocket pioneer Hermann Oberth.

> *Oberth designed a rocket which, he hoped, could be developed in a hurry. It consisted of a long vertical aluminum tube with several rods of carbon in the center, surrounded by liquid oxygen. The idea was that the carbon rods were to burn down from the top at the same rate as the oxygen was to be consumed, while the combustion gases were ejected through a set of nozzles at the top (forward) end of the rocket. He was never able to get it going, which was probably just as well, as it would infallibly have exploded. But – it was the first recorded design of a hybrid rocket – one with a solid fuel and a liquid oxidizer. (Clark, 1972)*

Oberth was correct in his assumption that hybrid rockets are relatively easy to develop. Sutton and Biblarz in their Rocket Propulsion Elements textbook give 3 advantages of hybrid rocket propulsion systems. They are: (1) enhanced safety from explosion or detonation; (2) start-stop-restart capabilities; and (3) relative simplicity (Sutton and Biblarz, 2010). To address the first point, some oxidizers such as nitrous oxide, a popular oxidizer choice for hybrid rockets, can present some hazards. Nitrous oxide can undergo sudden decomposition if proper precautions aren't taken, which can drastically increase the pressure in the hybrid rocket system, leading to pressure vessel failure (Campbell et al., 2008). When using gaseous oxygen though, this is not a concern. The 2nd advantage, start-stop capability, is an important feature necessary for launch vehicle upper-stages, which may need to perform multiple engine burns to reach the desired final orbit. The reason hybrid rocket engines can accomplish this is because the fuel will only burn in the presence of the oxidizer. Hence, if the flow of oxidizer can be controlled, then the engine can be started and stopped, given a reliable ignition source of course. The 3rd

advantage, relative simplicity, is perhaps the reason why hybrid rocket engines are a popular choice for universities to build. The complexity and cost of liquid-fueled rocket engines, especially turbo-pump driven ones, is out of reach both financially and technically for a lot of schools. The most basic hybrid rocket, however, only requires a pressurized source of oxidizer and a well-designed fuel grain to function. This is the type of hybrid rocket we will be focusing on because the hybrid rocket that is the subject of this thesis utilizes this method of delivering oxidizer to the motor.

The basic layout of a pressure-driven hybrid rocket is simple. Oxidizer, in our case gaseous oxygen, flows from the oxidizer tank to the fuel grain, driven by the pressurized reservoir. The fuel grain is the solid fuel portion of the hybrid rocket. Some popular choices for fuel grain materials are paraffin wax and Hydroxyl-terminated polybutadiene (HTPB). The simplest way to create a fuel grain is to make a cylinder and drill a hole through the center. This hole through the center is called the fuel port. More complex fuel grain geometries exist, such as helical fuel port channels, but we will focus on the simple case. As the oxidizer is flowing through fuel grain, a flammable gas is injected into the rocket and ignited to start the combustion process. The oxidizer combusts with the fuel grain port surface as it travels down the length of the fuel grain. The combustion products, now very hot, and under a lot of pressure, are expelled out of a converging-diverging nozzle to convert the hot, high-pressure gases into thrust. Figure 2.1 (Dyer, 2009) shows the general system diagram for a hybrid rocket system.

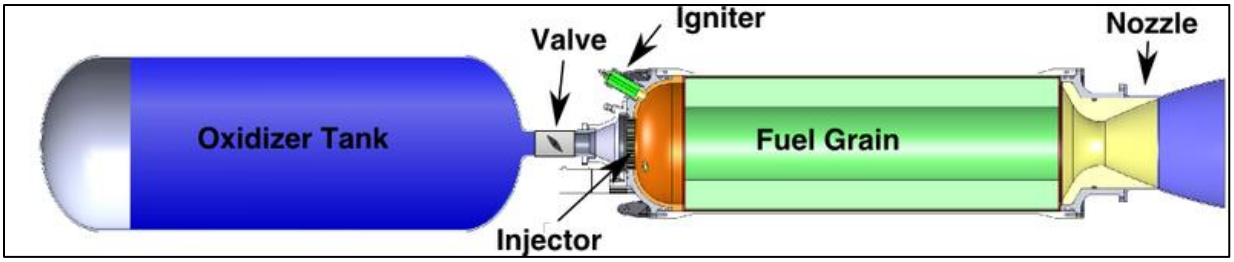

Figure 2.1. General System Diagram for a Hybrid Rocket (Dyer, 2009)

Figure 2.1 shows the 3 most essential parts of a simple hybrid rocket and the description that follows also describes how the NDSU hybrid rocket operates. The three essential parts of most hybrid rocket systems are the oxidizer delivery system, the fuel grain, and the nozzle. The theory and principles of each will be discussed in the next few sections.

2.2. Nozzle Theory

The nozzle is an essential part of any conventional rocket propulsion system, excluding technologies like ion propulsion. The purpose of the nozzle is to convert high pressure, high temperature, low velocity gases created by the combustion process into low pressure, (relatively low) temperature, high velocity gases, thereby producing thrust. Just as a classical heat engine extracts mechanical work from a high temperature reservoir and rejects waste heat to a low temperature reservoir, an ideal nozzle can be thought of as extracting thrust from a high temperature, high pressure reservoir by exhausting it to a low-pressure environment. This is achieved through a converging-diverging (CD) nozzle, which through a pressure differential accelerates gases from subsonic to supersonic. Figure 2.2 is an illustration of a general CD nozzle. (Sharaitzdeh et al., 2015)

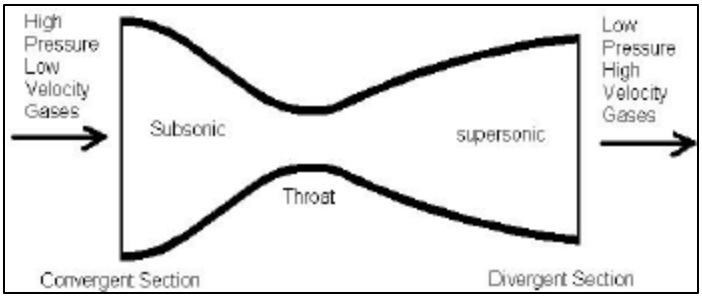

Figure 2.2. General Depiction of a Converging-Diverging (CD) Supersonic Nozzle (Shariatzadeh et al., 2015)

The CD nozzle consists of three parts; the converging section, the throat, and the diverging section. The expansion ratio of the nozzle is defined as

$$\epsilon = \frac{A_{exit}}{A^*} \tag{2.1}$$

where A^* is the area of the throat. Using continuity through a control volume (i.e the nozzle), we can derive a relationship that describes the Mach number as a function of the area of the nozzle. (Anderson, 2017) This relationship, known as the Area-Mach relation is

$$\left(\frac{A}{A^*}\right)^2 = \frac{1}{M^2}\left(\frac{2}{\gamma+1}\left(1+\frac{\gamma-1}{2}M^2\right)\right)^{\frac{\gamma+1}{\gamma-1}} \tag{2.2}$$

where γ is the heat capacity ratio (sometimes called the adiabatic index), defined as $\gamma = C_p/C_v$, A^* is the area of the throat of the nozzle, where the flow becomes "choked" at a sufficient pressure ratio, and M is the Mach number. Using Equation 2.2, we can determine what the Mach number of the flow will be at the exit of the nozzle. This, of course, requires that Equation 2.2 be solved numerically. Choked flow is a condition where the mass flow rate will not increase any further for a given downstream pressure. The critical pressure ratio is defined as (Anderson, 2017)

$$\frac{P^*}{P_0} = \left(\frac{2}{\gamma + 1}\right)^{\frac{\gamma}{\gamma-1}} \tag{2.3}$$

and is only dependent on the adiabatic index. For example, air, which has an adiabatic index of 1.4, has a critical pressure ratio of 0.5283. This means that for a nozzle utilizing air as the working fluid, the ratio of the nozzle exit pressure to the chamber pressure must be less than 0.5283 in order for the flow to become sonic at the throat and then supersonic through the diverging section of the nozzle. But how is the pressure ratio across the nozzle calculated? This is done through the isentropic relation (Anderson, 2017)

$$\frac{P}{P_0} = \left(1 + \frac{\gamma - 1}{2} M^2\right)^{\frac{-\gamma}{\gamma-1}} \tag{2.4}$$

where P_o is the stagnation pressure, which in the case of an ideal nozzle, is the chamber pressure, which sits at the very beginning of the converging section of the nozzle. Equation 2.3 is a special case of 2.4, where the Mach number is set to 1. We can derive two more isentropic relations for temperature and density (Anderson, 2017), which are

$$\frac{T}{T_0} = \left(1 + \frac{\gamma - 1}{2} M^2\right)^{-1} \tag{2.5}$$

$$\frac{\rho}{\rho_o} = \left(1 + \frac{\gamma - 1}{2} M^2\right)^{\frac{-1}{\gamma-1}} \tag{2.6}$$

Of course, ρ can also be calculated from the ideal gas relation

$$P = \rho R T \tag{2.7}$$

We can also relate the temperature, pressure, and density ratios together with the following relation (Anderson, 2017)

$$\frac{P}{P_o} = \left(\frac{\rho}{\rho_0}\right)^{\gamma} = \left(\frac{T}{T_o}\right)^{\frac{\gamma}{\gamma-1}} \tag{2.8}$$

From the stagnation conditions T_o, P_o, and ρ_o, we can calculate T, P, and ρ at any point in the nozzle, provided we have calculated the Mach number for every point in the nozzle, which we can easily do with Equation 2.2. Figure 2.3 shows how the temperature, pressure, and density generally change through the nozzle from the chamber to the exit for a Mach 2 nozzle.

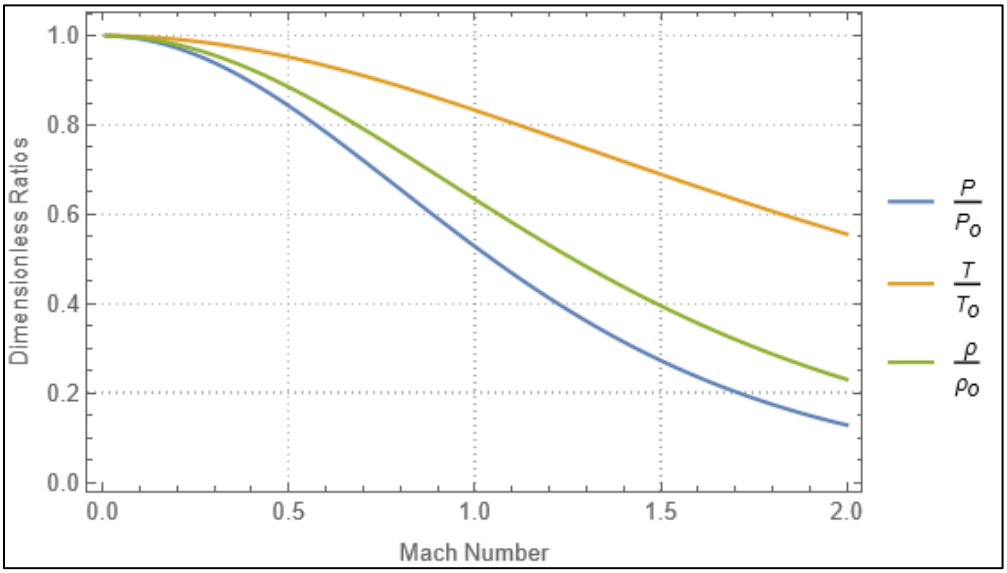

Figure 2.3. Chart of Temperature, Pressure, and Density Through a Mach 2 Nozzle, γ = 1.4

This leads into the next part of how the exhaust velocity of a nozzle is calculated. Since we have the Mach number at the nozzle exit from Equation 2.2, we can use the definition of the speed of sound to calculate the actual velocity. (Benson, 2021)

$$v_e = M_e\sqrt{\gamma R T_e} \tag{2.9}$$

where R is the gas constant for the working fluid. Now that we have the means of calculating the exhaust velocity of the nozzle, we now need to calculate the mass flow rate through the nozzle. The closed-form expression for calculating the mass flow rate through the nozzle is (Anderson, 2017)

$$\dot{m} = \frac{P_c A^*}{\sqrt{T_c}} \sqrt{\frac{\gamma}{R} \left(\frac{2}{\gamma + 1} \right)^{\frac{\gamma+1}{\gamma-1}}} \tag{2.10}$$

Now that we have expressions for both the mass flow rate and the velocity, we can calculate the thrust that the nozzle produces. Using the control volume approach in gas dynamics (Sutton and Biblarz, 2010), we arrive at the expression (Benson, 2021)

$$F = \dot{m} v_e + (P_e - P_{atm}) A_e \tag{2.11}$$

The term $\dot{m} v_e$ in Eq. 2.11 is known as the momentum thrust and the second term represents the pressure thrust (Sutton and Biblarz, 2010). When the exit pressure of the nozzle equals the ambient pressure, the pressure thrust term zeros out and we are just left with the first term of Equation 2.11. When this occurs, the nozzle is said to be perfectly expanded. When the exit pressure is greater than ambient pressure, the nozzle is said to be *underexpanded*. If the exit pressure is lower than the ambient pressure, then the nozzle is said to be *overexpanded*. Gross overexpansion can cause flow separation from the interior of the nozzle. Therefore, it is important to consider the environment when designing a nozzle. Using Equations (3-16), (3-21) and (3-23) from Sutton and Biblarz, we can write Eq 2.11 as (Sutton and Biblarz, 2010)

$$F = A_t P_c \sqrt{\frac{2\gamma^2}{\gamma - 1} \left(\frac{2}{\gamma + 1} \right)^{\frac{\gamma+1}{\gamma-1}} \left(1 - \left(\frac{P_e}{P_c} \right)^{\frac{\gamma-1}{\gamma}} \right)} + (P_e - P_{atm}) A_e \tag{2.12}$$

A useful figure of merit we can define is called the coefficient of thrust and is defined as (Sutton and Biblarz, 2010)

$$C_F = \frac{F}{A_t P_C} \tag{2.13}$$

According to Sutton and Biblarz, "The thrust coefficient can be thought of as representing the amplification of thrust due to the gas expanding in the supersonic nozzle as compared to the thrust that would be exerted if the chamber pressure acted over the throat area only." (Sutton and Biblarz, 2010)

Now that we can calculate the thrust a nozzle produces, we must consider how we measure the efficiency of a rocket in general. The goal of a rocket is to produce a change in velocity or Δv. The Tsiolkovsky rocket equation governs all types of rockets that use reaction mass and is written as

$$\Delta v = v_e \ln\left(\frac{m_0}{m_f}\right) \tag{2.14}$$

where m_0 is the fully loaded mass of the rocket and m_f is the empty weight of the rocket after all the propellant has been expended. Space missions are often stated in terms of delta-v. For example, the delta-v needed to achieve a circular, low Earth orbit is around 9.4 km/s, which includes losses from gravity and atmospheric drag. So, we can see that from Equation 2.14, the higher the exhaust velocity is, the more delta-v will be available for a given amount of reaction mass. However, it more common to express exhaust velocity in terms of specific impulse, which is defined as

$$I_{sp} = \frac{F}{\dot{m} g_0} \tag{2.15}$$

where g_0 is 9.81 m/s^2. The units are in seconds. This can be thought of as the thrust divided by the weight flow of the propellant (Clark, 1972). This definition, using Eq. 2.11 without the pressure term, can be reduced to

$$I_{sp} = \frac{v_e}{g_0} \tag{2.16}$$

Clark said about this definition "Probably the best way of thinking of specific impulse is as a velocity expressed, not in meters or feet per second, but in units of 9.8 meters per second. That way you retain the concept of mass flow, which is relevant everywhere, and doesn't depend upon the local properties of one particular planet" (Clark, 1972). To give a comparison of some specific impulse figures, SpaceX's 1st stage Merlin engine, which uses RP-1 and liquid oxygen, can achieve a vacuum specific impulse of 311 s. Aerojet Rocketdyne's RS-25 engine, which uses liquid hydrogen and liquid oxygen, can achieve a vacuum specific impulse of 452.3 s. 470 s represents the upper limit for rocket engines using liquid hydrogen and liquid oxygen, and is basically the upper limit for chemical propulsion. Some propellant combinations that use exotic oxidizers such as fluoride have achieved specific impulses of around 500 s, but the hazardous and difficult nature of these exotic oxidizers has prevented their use in flight service. For higher specific impulses, alternate technologies must be employed, such as the solid-core nuclear thermal rocket, which can theoretically achieve specific impulses of up to 1000 s, if hydrogen is utilized as the working fluid.

The Space Shuttle Solid Rocket Booster, which uses polybutadiene acrylonitrile and ammonium perchlorate composite propellant, has a specific impulse of 242 s at sea level. Hybrids, naturally, fall somewhere in between solids and bipropellant liquid engines in terms of specific impulse. A hybrid that used a metallized fuel grain consisting of lithium and lithium hydride embedded in a PBAN fuel grain and a fluorine/oxygen mixture achieved a specific

impulse of 400 s in testing.(“A brief history of hybrid rocket technology”) However, looking at Figure 2.4 (Sutton and Biblarz, 2010), which plots the specific impulse of HTPB and variety of oxidizers against their mixture ratios, around 300 s is more common for HTPB and conventional oxidizers. Figure 2.5 (Tarifa and Pizzuti, 2019) shows some theoretical specific impulses for a few different combinations of fuels and oxidizers

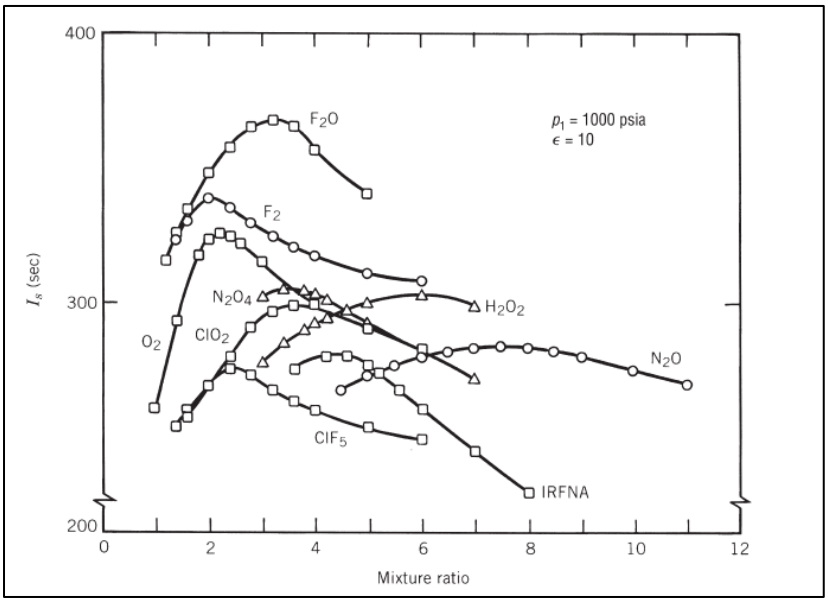

Figure 2.4. Theoretical Vacuum Specific Impulse of Selected Oxidizers Reacted with HTPB Fuel (Sutton and Biblarz, 2010) (Reprinted with Permission)

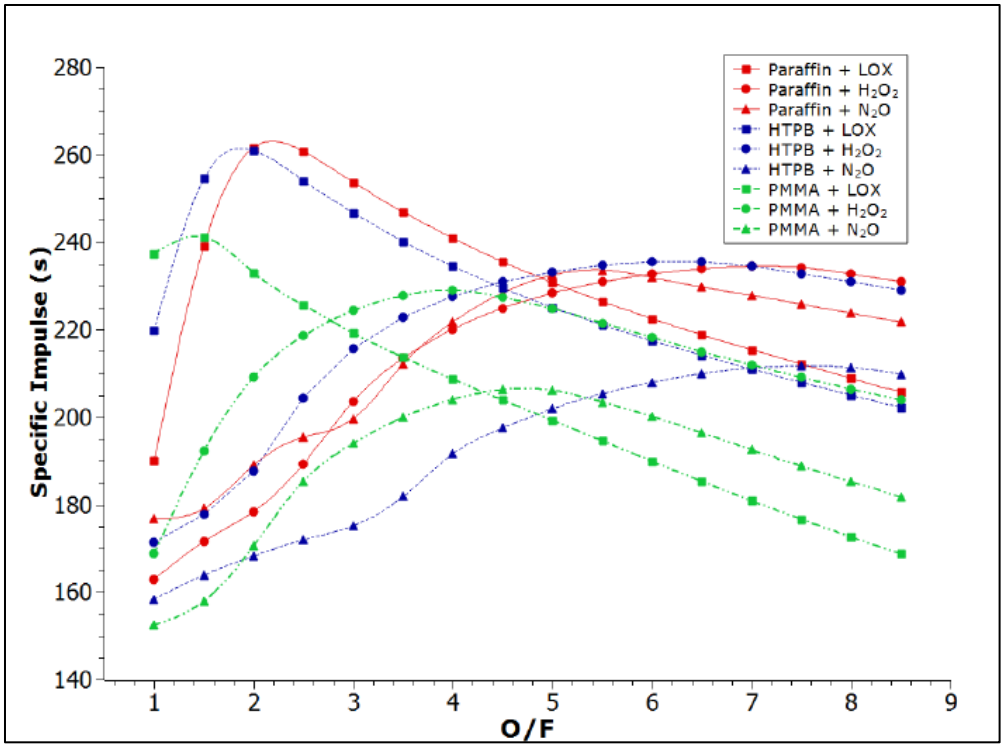

Figure 2.5. Specific Impulse of Different Combinations of Reactants as a Function of Mass-Based O/F (Tarifa and Pizzuti, 2019)

Comparing the HTPB specific impulse figures in Figures 2.4 and 2.5, one sees that Figure 2.5 reports a lower range of specific impulses for HTPB and its various oxidizers. This is because specific impulse calculations primarily depend on three things: the chamber pressure, the nozzle expansion ratio, and the ambient pressure. If a very high expansion ratio nozzle is used in specific impulse calculations, then the calculated specific impulse will be higher compared to specific impulse calculations that use a low expansion ratio nozzle. This can make comparing specific impulses of different fuel and oxidizer combinations difficult. Hence, the need for a figure of merit that is independent of nozzle expansion ratio. This is where the characteristic velocity, or c*, is introduced. The characteristic velocity is defined as (Sutton and Biblarz, 2010) (Werling et al., 2019)

$$c^* = \frac{P_c A_t}{\dot{m}} \tag{2.17}$$

where A_t is the area of the nozzle throat. The c* parameter lends itself well to calculating combustion efficiency, which can be calculated as (Werling et al., 2019)

$$\eta_{c^*} = \frac{c^*_{exp}}{c^*_{theo}} \tag{2.18}$$

where c^*_{exp} is the c* value calculated in Equation 2.17 through experimental measurements of the mass flow rate and the chamber pressure, and c^*_{theo} is calculated by using a program such as NASA's Chemical Equilibrium with Applications (CEA).

One final thing that should be noted is the process of designing a nozzle shape. While Equation 2.2 can tell us the area ratio needed to achieve a certain Mach number, it doesn't tell us what shape the nozzle should be or how long it should be. There are two methods that can be used to determine an optimum nozzle profile. There is the Method of Characteristics, which can be used to create a minimum length nozzle, and there is Rao's Method. The nozzle that was designed for the NDSU hybrid rocket utilized Rao's method (Estevadeordal et al., 2021) Figure 2.6 is a dimensioned cutaway view of the nozzle design that was used for all tests and is taken from the design team's body of CAD drawings for the rocket and test stand.

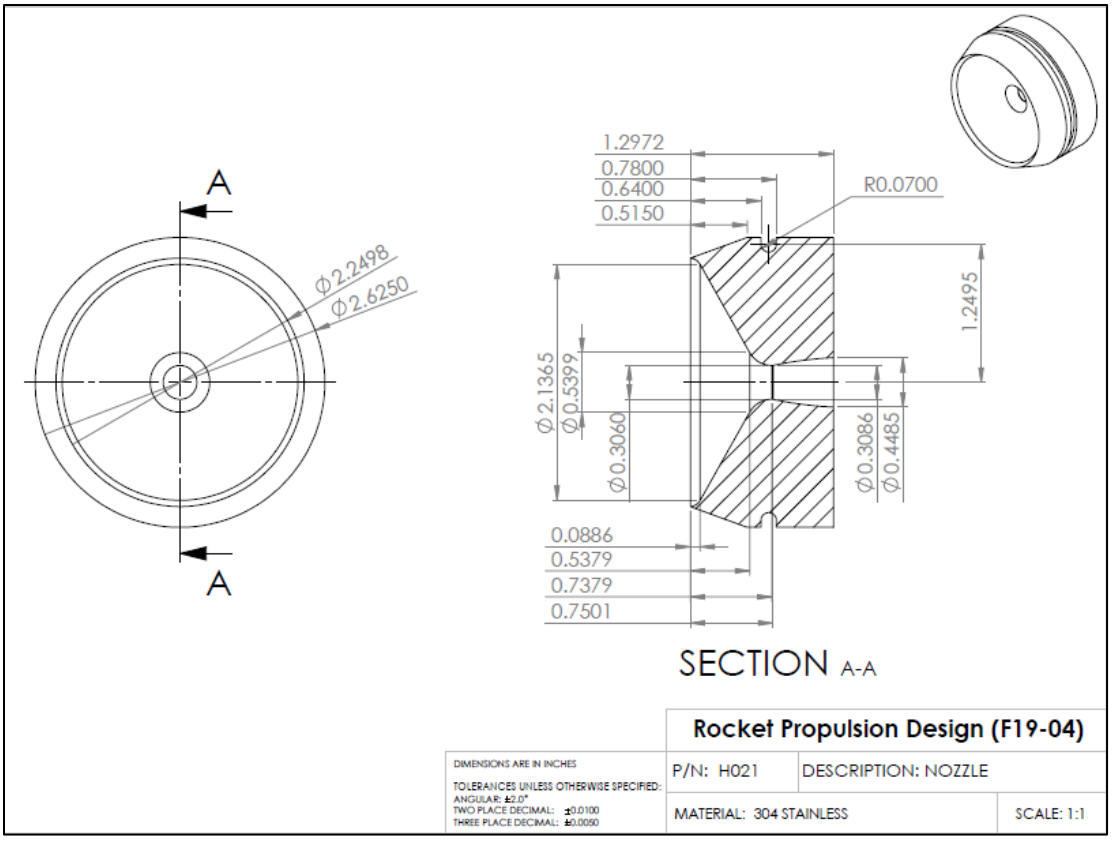

Figure 2.6. Dimensioned Drawing of NDSU Hybrid Rocket Nozzle (Courtesy of NDSU RPDT)

Over the course of the NDSU testing program, 3 nozzle materials have been used. They are stainless steel, coarse graphite, and ultrafine graphite. Nozzles, especially in hybrid rockets, have the problem of throat erosion (Narsai, 2016). When the throat area grows, the expansion ratio of the nozzle decreases, and therefore the exhaust velocity of the rocket decreases. So, the nozzle throat diameters were measured before and after each test, to quantify the amount of erosion and assess the severity. Figures 2.7 and 2.8 show the difference between coarse graphite and ultrafine graphite.

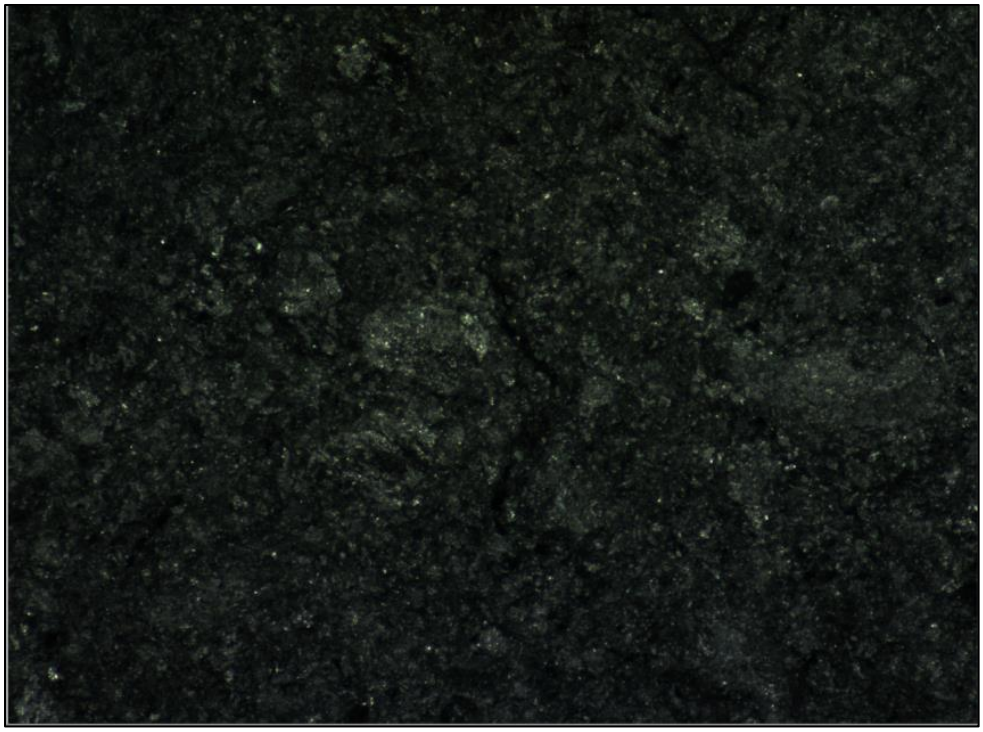

Figure 2.7. Coarse Graphite as Viewed Under Computer Microscope

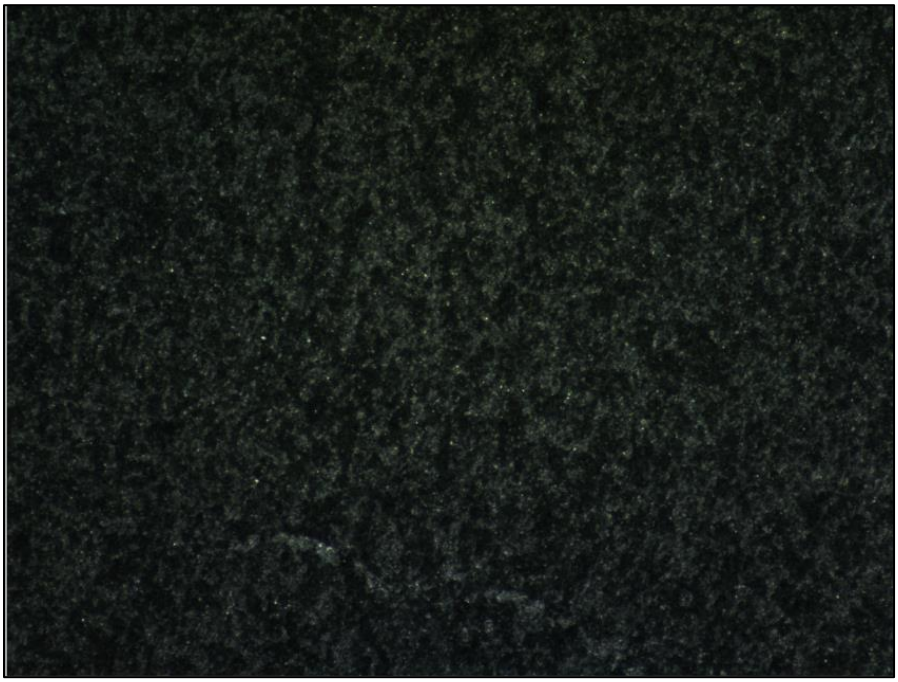

Figure 2.8. Ultrafine Graphite as Viewed Under Computer Microscope

2.3. Theory of Fuel Grain Combustion

2.3.1. Fuel Grain Combustion

The NDSU hybrid rocket utilizes optically clear polymethylmethacrylate (PMMA), otherwise known as acrylic. As implied in the name, PMMA is a polymer made up of repeating units of the monomer methyl methacrylate (MMA) (Rabinovitch et al, 2018). The combustion process of the fuel grain, greatly simplified, can be written as (Estevadeordal et al., 2021)

$$aC_5H_8O_2 + bO_2 \rightarrow n_{CO_2}CO_2 + n_{H_2O}H_2O + n_{O_2}O_2 \tag{2.19}$$

where a is the number of moles of fuel, b is the number of moles of oxygen, and n_{O_2} is the number of moles of oxygen left over after the oxidizer-rich combustion process. The stoichiometric chemical reaction can be written as

$$C_5H_8O_2 + 6O_2 \rightarrow 5CO_2 + 4H_2O \tag{2.20}$$

So, the stoichiometric (O/F) molar ratio for the combustion of MMA is 6. Equation 2.19 greatly simplifies the combustion process and does not consider things such as pyrolysis of the fuel grain (Dhandapani et al., 2019). It also does not consider dissociation products such as O, H, OH, C, CO (Estevadeordal et al., 2021). It also does not consider other combustion products that are theoretically possible, such as methane, solid phase carbon, and hydrogen. We will investigate these in the computational studies section of this thesis. It was on the basis of Equation 2.19 that the hybrid rocket was designed by the original design team. More details on the design process can be found in the reference listed in the References section (Estevadeordal, 2021).

2.3.2. Fuel Grain Regression

Fundamental to hybrid rocket theory is describing how the fuel port diameter burns over time. Consider a circular fuel grain with a single port drilled down the center of an initial radius

R_i. As the combustion process proceeds, the channel radius increases in size over time. We can characterize this process with the following regression law (Sutton and Biblarz, 2010)

$$\dot{r} = a(G_o)^n \tag{2.21}$$

where *a* and *n* are empirical coefficients, G_o is the oxidizer mass flux, and $\dot{r}$ is the regression rate. Although Equation 2.21 is valid for intermediate oxidizer mass flux regimes (Sutton and Biblarz, 2010), it is standard practice in hybrid rocket design to start with Equation 2.21 (Rabinovitch et al, 2018). Equation 2.21 can be recast as (Sutton and Biblarz, 2010)

$$\dot{r} = a\left(\frac{\dot{m}_o}{\pi R^2}\right)^n \tag{2.22}$$

Equation 2.22 can be simply integrated to give combustion port radius, instantaneous fuel flow rate and the instantaneous mixture ratio. These are, in order (Sutton and Biblarz, 2010)

$$R(t) = \left(a(2n+1)\left(\frac{\dot{m}_o}{\pi N}\right)^n t + R_i^{2n+1}\right)^{\frac{1}{2n+1}} \tag{2.23}$$

$$\dot{m}_f(t) = 2\pi N \rho_f L a \left(\frac{\dot{m}_o}{\pi N}\right)^n \left(a(2n+1)\left(\frac{\dot{m}_o}{\pi N}\right)^n t + R_i^{2n+1}\right)^{\frac{1-2n}{1+2n}} \tag{2.24}$$

$$\frac{\dot{m}_o}{\dot{m}_f}(t) = \left(2\pi\rho_f L a\right)^{-1}\left(\frac{\dot{m}_o}{\pi N}\right)^{1-n}\left(a(2n+1)\left(\frac{\dot{m}_o}{\pi N}\right)^n t + R_i^{2n+1}\right)^{\frac{2n-1}{2n+1}} \tag{2.25}$$

where *L* is the length of the fuel grain, ρ_f is the density of the fuel grain, R_i is the initial port radius, and *N* is the number of ports in the fuel grain. When designing a hybrid rocket, it may be necessary to know what the average fuel mass flow rate is and what the average O/F is. In this case, we can use the integral definition of an average, provided here for convenience

$$f_{avg} = \frac{1}{b-a}\int_a^b f(x)dx \tag{2.26}$$

Applying Eq 2.26 to Eq 2.24 and Eq 2.25, we get

$$\overline{\dot{m}_f} = \frac{1}{t_2 - t_1}\int_{t_1}^{t_2} 2\pi N\rho_f La\left(\frac{\dot{m}_o}{\pi N}\right)^n \left(a(2n+1)\left(\frac{\dot{m}_o}{\pi N}\right)^n t + R_i^{2n+1}\right)^{\frac{1-2n}{1+2n}} dt \tag{2.27}$$

$$\left(\frac{O}{F}\right)_{avg,molar} = \frac{M_{PMMA}}{M_{O_2}}\frac{1}{t_2 - t_1}\int_{t_1}^{t_2}\left(2\pi\rho_f La\right)^{-1}\left(\frac{\dot{m}_o}{\pi}\right)^{1-n}\left(a(2n+1)\left(\frac{\dot{m}_o}{\pi}\right)^n t + R_i^{2n+1}\right)^{\frac{2n-1}{2n+1}} dt \tag{2.28}$$

Both Equations 2.27 and 2.28 have no neat closed-form solutions and must be numerically integrated.

In the literature, there have been a few attempts to characterize the regression behavior of fuel grains made up of PMMA. Rabinovitch et al. in 2018 attempted to experimentally determine the regression coefficients for PMMA and oxygen. Depending on what fitting method was used, *n* varied from 0.35 to 0.51, and *a* varied from 4.37E-05 to 8.96E-05. Mechentel et al. in 2019 reported an *a* value of 4.17E-05 and an *n* value of 0.438, while acknowledging that *n* only varied by 4%, while *a* varied by as much as 20%. According to them, *a* is likely to be strongly dependent on experimental conditions. Additionally, Zilliac and Karabeyoglu in 2006 reported from a much older study done in the early 90's an *n* value of 0.615 and an *a* value of 0.087. The reason *a* is much higher than the other reported values is because it is in units of grams/cm^{2}s to produce a regression rate of mm/s. The wide disparity in reported regression coefficients for hybrid rockets highlights the need for test firing in order to gather performance data. Because the PMMA fuel grain used by the NDSU hybrid rocket is optically clear, the regression rate of the

fuel port can directly be measured with imaging equipment. The imaging techniques are discussed later in the paper.

2.3.3. Brief Overview of Heat Transfer Mechanisms Within Fuel Grain

Here, we will briefly discuss the thermodynamics of a combusting fuel grain. Figure 2.9 (Zilliac and Karabeyoglu, 2006) shows a conceptualization of the flow and energy balance within a hybrid rocket motor with a cylindrical port. (Zilliac and Karabeyoglu, 2006)

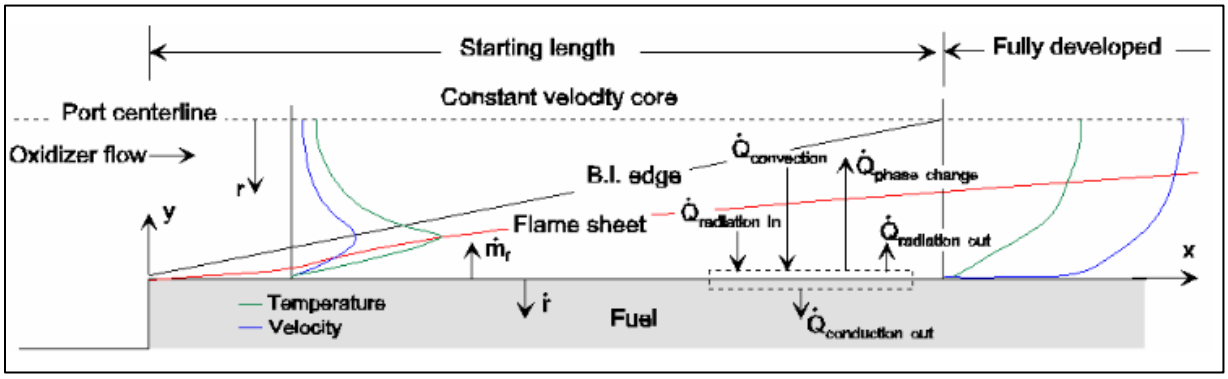

Figure 2.9. Flow and Energy Balance within Fuel Grain (Zilliac and Karabeyoglu, 2006)

At the fuel surface, the steady-state energy balance seen in Figure 2.9 is (Zilliac and Karabeyoglu, 2006)

$$\dot{Q}_{convection} + \dot{Q}_{radiation-in} = \dot{Q}_{conduction-out} + \dot{Q}_{phase\ change} + \dot{Q}_{radiation-out} \tag{2.29}$$

which on a per unit surface area basis, can be written as (Zilliac and Karabeyoglu, 2006)

$$k_g \frac{\partial T}{\partial y}\bigg|_{y=0^+} + \alpha \epsilon_g \sigma T_f^4 = k_f \frac{\partial T}{\partial y}\bigg|_{y=0^+} + \rho_f \dot{r} h_g + \epsilon_s \sigma T_s^4 \tag{2.30}$$

where h_g is the enthalpy of gasification (Zilliac and Karabeyoglu, 2006). At the fuel surface, the rate-of-heat transfer per unit area convected from the flame sheet to the surface is equal to that conducted (Zilliac and Karabeyoglu, 2006). Therefore, the simplified fuel surface energy balance can be written as (Zilliac and Karabeyoglu, 2006)

$$\dot{Q}_s = \rho_f \dot{r} h_g \tag{2.31}$$

2.4. Oxidizer Delivery

So far, we have discussed the theory of rocket nozzles and the theory of fuel grain combustion. From the theory of fuel grain combustion, we can at least attempt to predict the fuel mass flow rate. Now, we turn our attention to the other half of the combustion process, the oxidizer mass flow rate. We wish to supply the hybrid motor with a nearly constant mass flow rate of gaseous oxygen. The pressurized tank of oxygen acts as the driver that pushes the oxidizer though the motor. We place a venturi constriction on the oxidizer line between the oxygen tank and the oxygen injector on the hybrid motor so that the mass flow rate of the oxygen can be calculated. The following derivation was taken from Jens, 2015. The mass flow rate of a gas through a venturi can be written as (Jens, 2015)

$$\dot{m} = C_D \dot{m}_{ideal} \tag{2.32}$$

where the ideal mass flow rate can be calculated as (Jens, 2015)

$$\dot{m}_{ideal} = \rho U A \tag{2.33}$$

The conservation of energy for a 1D flow across an orifice can be written as (Jens, 2015)

$$h_{t1} = h_{t2} \tag{2.34}$$

Assuming that the gas is ideal and calorically perfect, we obtain (Jens, 2015)

$$C_p T_1 + \frac{U_1^2}{2} = C_p T_2 + \frac{U_2^2}{2} \tag{2.35}$$

Inserting equations 2.32, 2.33, and 2.8 into 2.35, we arrive at the result (Jens, 2015)

$$\dot{m}_o = C_d A_2 \sqrt{\frac{2\rho_1 P_1 \left(\frac{\gamma}{\gamma-1}\right)\left(\left(\frac{P_2}{P_1}\right)^{\frac{2}{\gamma}} - \left(\frac{P_2}{P_1}\right)^{\frac{\gamma+1}{\gamma}}\right)}{1-\left(\frac{A_2}{A_1}\right)^2\left(\frac{P_2}{P_1}\right)^{\frac{2}{\gamma}}}} \tag{2.36}$$

where A_2 denotes the area of the narrow part of the venturi, A_1 is the area upstream of the venturi, subscript 1 indicates upstream conditions, and subscript 2 denotes downstream conditions. The discharge coefficient C_d can be derived from data the manufacturer of the venturi publishes, but the discharge coefficient usually takes on a value of at least 0.9. The bottom term in Equation 2.36 usually takes on a value of 0.99 or more, and is often neglected in other sources (*Handbook of Chemical Hazard Analysis Procedures)* so Equation 2.36 can be simplified to

$$\dot{m}_o = C_d A_2 \sqrt{2\rho_1 P_1 \left(\frac{\gamma}{\gamma-1}\right)\left(\left(\frac{P_2}{P_1}\right)^{\frac{2}{\gamma}} - \left(\frac{P_2}{P_1}\right)^{\frac{\gamma+1}{\gamma}}\right)} \tag{2.37}$$

Under choked flow conditions, where $\frac{P_2}{P_1}$ reaches the critical pressure ratio for the working fluid, Equation 2.37 simplifies even further down to (*Handbook of Chemical Hazard Analysis Procedures)*

$$\dot{m}_o = C_d A_2 \sqrt{\gamma P_1 \rho_1 \left(\frac{2}{\gamma+1}\right)^{\frac{\gamma+1}{\gamma-1}}} \tag{2.38}$$

Equations 2.37 and 2.38 are used to calculate the mass flow rate of oxygen into the NDSU hybrid rocket, depending on whether the flow is choked or not.

2.5. Overview of Design Parameters for Hybrid Rocket

Table 2.1 summarizes the design parameters for the NDSU hybrid rocket (Estevadeordal et al., 2021)

Table 2.1. Summary of NDSU Hybrid Rocket Design Parameters

Parameter	**Value**	**Description**
O2 Reaction Ratio	0.87	Fraction of inlet O2 reacting
Adiabatic Temperature Modifier	0.80	Fraction of Adiabatic Flame Temperature
O2 Inlet Mass Flow Rate	0.020 kg/s	O2 flowing into fuel grain
Design Mach Number	2.0739	Assumes nozzle efficiency of 0.93
Modified Adiabatic Flame Temperature	3469 K	Combustion chamber temperature
Exhaust Temperature	2529 K	
Chamber Pressure	864.9 kPa	
Nozzle Expansion Ratio	2.148	
Nozzle Throat Diameter	7.8 mm	
Exhaust Velocity	1744 m/s	Assumes nozzle efficiency of 0.93
Thrust	50.7 N	

The chemical reaction for the NDSU hybrid rocket when it is operating at its design condition is (Estevadeordal et al., 2021)

$$C_5H_8O_2 + 6.8966O_2 \rightarrow 5CO_2 + 4H_2O + 0.8966O_2 \quad (2.39)$$

Table 2.2 shows the expected mole fractions of the exhaust gases based on Equation 2.39

Table 2.2. Composition of Exhaust Gases

$\boldsymbol{O_2}$	0.0906
$\boldsymbol{CO_2}$	0.505
$\boldsymbol{H_2O}$	0.404

Finally, Table 2.3 shows the properties of the PMMA fuel grain used by the NDSU hybrid rocket.

Table 2.3. PMMA Fuel Grain Properties

Length of fuel grain, L	0.3048 m
Fuel grain density, ρ_f	1185 kg/m^3
Initial fuel grain port radius, R_i	0.004765 m
Fuel grain diameter	0.0762 m

3. COMPUTATIONAL STUDIES

3.1. Chemical Equilibrium with Applications (CEA)

3.1.1. Background & Theory

Chemical Equilibrium with Applications (CEA) is a computer program developed by NASA for the purpose of analyzing reacting systems and calculating the properties of complex mixtures. The program is commonly used to analyze combusting systems, including rockets. CEA was used to analyze the combustion process of the NDSU hybrid rocket and predict the theoretical performance. An overview of how the software works, and the steps taken to run the analysis will be detailed here.

NASA Reference Publication 1311 Part 1 (Gordon & Mcbride, 1994) is the NASA technical report that details the mathematics behind how CEA works. The key assumptions for this program are as follows (Sutton and Biblarz, 2010)

- One-dimensional forms of the continuity, energy, and momentum equations.
- Negligible velocity at the forward end of the combustion chamber (stagnation condition)
- Isentropic expansion in the nozzle
- Ideal gas behavior

Generally, according to Gordon & McBride, CEA works by utilizing a minimization of free energy method. This formulation is solved iteratively until the free energy reaches a minimum. For predicting theoretical rocket performance, CEA has two options, each of which use different assumptions under which the program is run. With the infinite area combustor (IAC) formulation, the rocket combustion chamber is treated as being infinite. Figure 3.1 (Gordon and McBride, 1994) is an illustration of the IAC formulation.

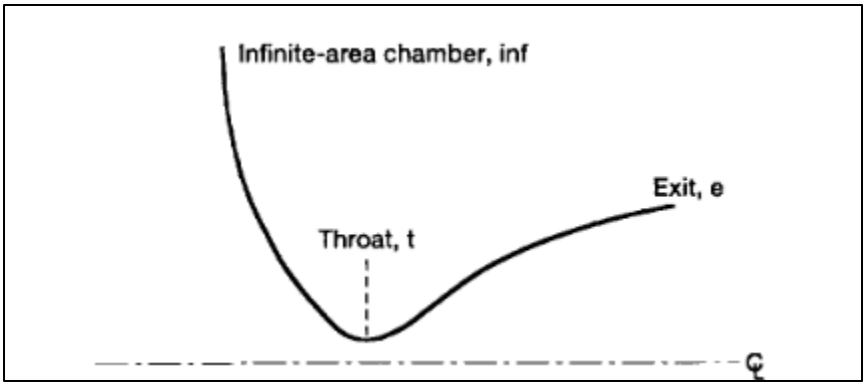

Figure 3.1. Infinite Area Chamber (Gordon and Mcbride, 1994)

For the IAC formulation, there are two further options, equilibrium and frozen. The equilibrium formulation is based on the assumption of instantaneous chemical equilibrium during expansion in the nozzle. Frozen performance is based on the assumption that composition remains frozen at the combustion composition during expansion (Gordon & Mcbride, 1994). With the equilibrium expansion, the chemical composition of the exhaust is shifting as it expands through the nozzle. This means that the average molecular weight and the adiabatic index is changing as well, which affects nozzle performance. With the frozen assumption, the chemical composition of the exhaust can be fixed at a user-defined point, such as the nozzle throat. In addition to the IAC formulation, there is the finite-area combustor (FAC) formulation, which, of course, assumes a finite combustion chamber area. There are two ways to define this finite area. A contraction ratio for the nozzle can be specified, or the ratio of the mass flow rate to chamber area can be specified. For the FAC formulation, the equilibrium assumption is always used. Figure 3.2 (Gordon and McBride, 1994) illustrates the finite area assumption.

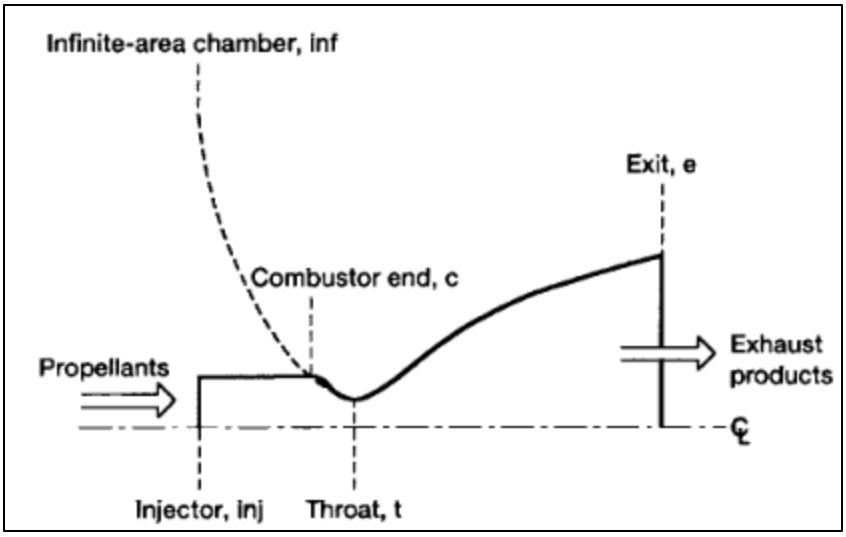

Figure 3.2. Finite Area Combustor Illustration (Gordon and Mcbride, 1994)

Once the chemical composition of the combustion products has been calculated, CEA uses the principle of isentropic flow to calculate performance figures such as the exhaust temperature, specific impulse, and so forth. (Gordon & Mcbride, 1994).

To set up a rocket problem in CEA, the reactants need to be defined. CEA contains a database of the most common reactants used in rocketry but allows for user-defined reactants as well. Since PMMA is not in the database, its molecular formula must be defined, along with its enthalpy of formation, and reference temperature. For this CEA analysis, the PMMA fuel was treated as the MMA monomer in the gas phase. This reflects how PMMA undergoes combustion. PMMA will undergo pyrolysis into products that primarily consists of MMA in the gaseous phase (Dhandapani et al, 2019). The NIST Chemistry WebBook lists several enthalpies of formation for the MMA gas phase, so the lowest value, -331.0 kJ/mol, was chosen. This was also the value used by the original design team for their calculations. The reference temperature assigned was the boiling point of MMA, 373.4 K, which was also taken from the NIST WebBook. This of course, greatly simplifies the combustion process that occurs inside the fuel grain, as the depolymerization, melting, and vaporization of the PMMA is not considered. For

the oxidizer, the chemical formula for gaseous oxygen was specified, the enthalpy of formation set to 0 kJ/mol, and the reference temperature set to 298.15 K, the standard NIST reference temperature. Figure 3.3 shows these settings as they were entered into the program.

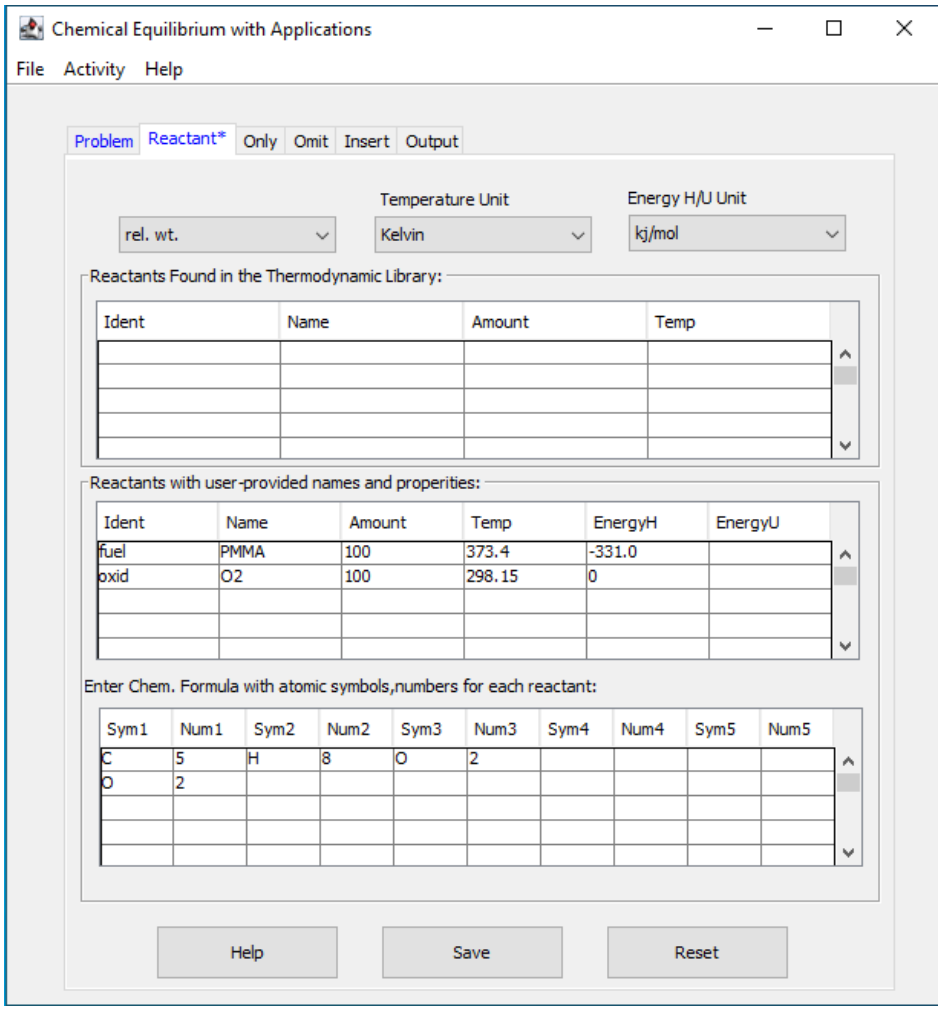

Figure 3.3. CEA Reactant Definitions

Next, after the reactant properties have been defined, the initial conditions for the rocket need to be defined. One of these initial conditions is the chamber pressure. To fully explore how chamber pressure affects the performance of the rocket, 4 different chamber pressures were used, based off both testing experience and the expected chamber pressure taken from initial design specs. Initially, the preliminary calculated chamber pressure of 125.4 psi was used, but this was

changed to 140.1 psi_a since there was uncertainty as to whether the figure of 125.4 psi was gauge pressure or absolute pressure. In any case, a difference of 14.7 psi makes only a small difference in the results. Multiples of the 140.1 psi_a figure were used. There were 70.05 psi_a, 280.2 psi_a, and 420.3 psi_a. The next initial condition to be set is the combustion temperature. This acts as an initial estimate for the program to iterate from. Based on the preliminary performance figures, the initial combustion temperature was set to 3000 K. Next, the supersonic expansion ratio, A_e/A_t, was set to 2.148, which is the ratio the NDSU hybrid rocket nozzle uses. For the FAC case, the contraction ratio, a_c/a_t, is set to 48.75, also the ratio the NDSU hybrid rocket nozzle uses. Figure 3.4 shows the settings as they are entered into the CEA program.

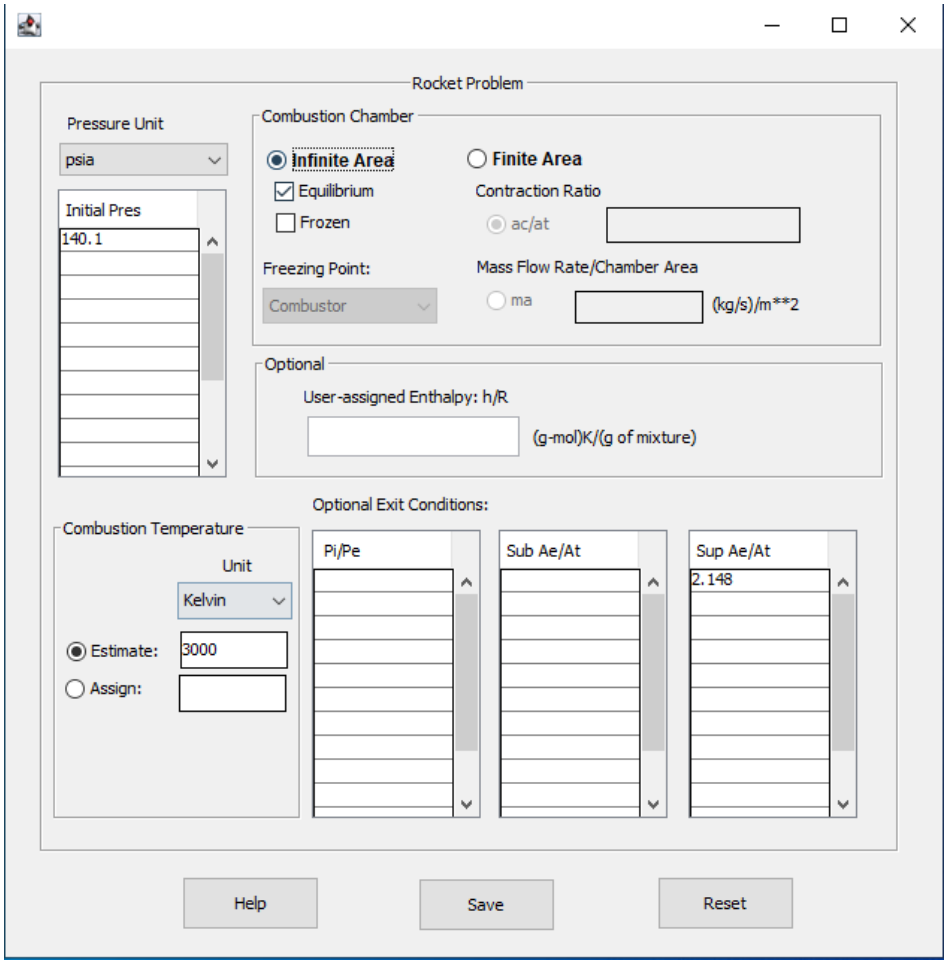

Figure 3.4. CEA Initial Conditions & Settings Window

Finally, a set of mass-based O/F ratios is set. The values used ranged from 0.1 to 3.0. The preliminary expected O/F ratio of the NDSU hybrid rocket sits inside this range.

3.1.2. Results

Figure 3.5 shows the computed chamber temperature as a function of the molar O/F ratio for 4 different chamber pressures. It is interesting to note that the chamber temperature does not quite seem to reach its peak value at the stoichiometric O/F ratio of 6, but instead reaches its peak value at something like 5.75. At an O/F ratio of 6.8966, the design operating condition of the hybrid rocket, we see that the computed chamber temperature for the design chamber pressure of 141.1 psi_a is around 3200 K, which is roughly ~200K lower than what was initially calculated. Notice that the higher the chamber pressure is, the hotter the chamber temperature gets. It is also interesting to note that in the O/F region of 2 to 3, the chamber pressure has no effect on the chamber temperature. We can see this phenomenon with the other charts as well.

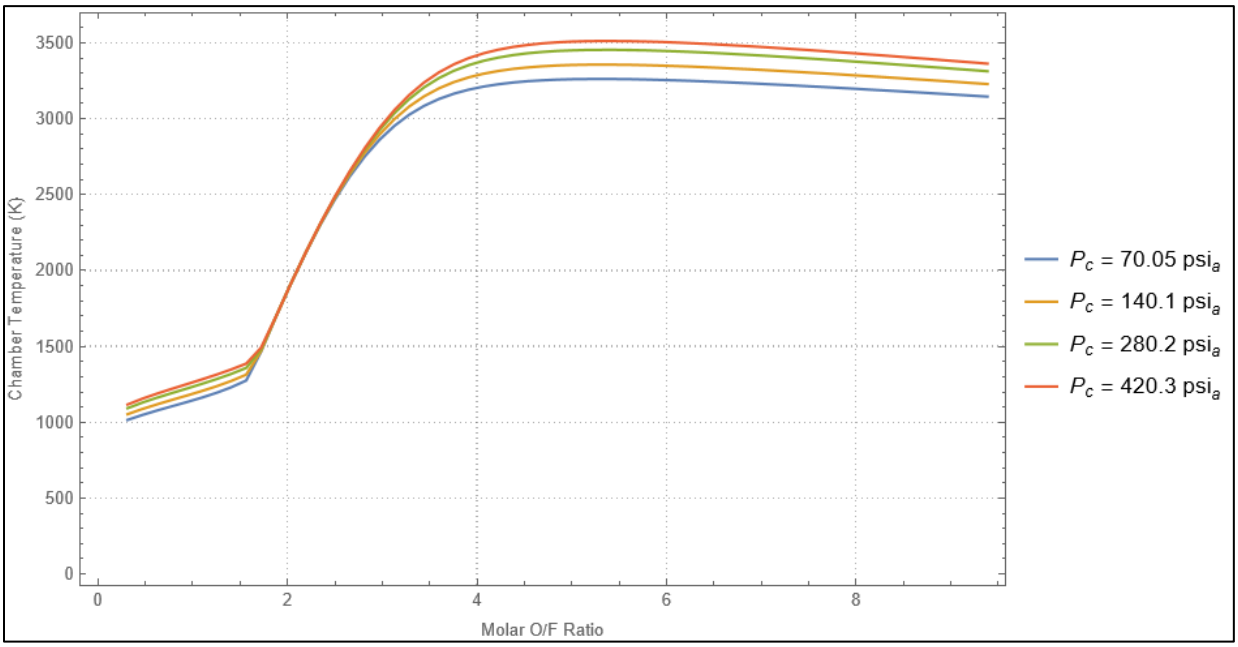

Figure 3.5. Molar O/F Ratio vs. Chamber Temperature for Multiple Chamber Pressures, Equilibrium & Infinite Area Conditions

Figure 3.6 shows the computed exhaust temperature as a function of the molar O/F ratio. It is identical to Figure 3.5, save that it is shifted downwards. For 140.1 psi_a at an O/F ratio of around 7, the exhaust temperature is predicted to be 2700 K, which is ~200 K higher than what was calculated by the design team.

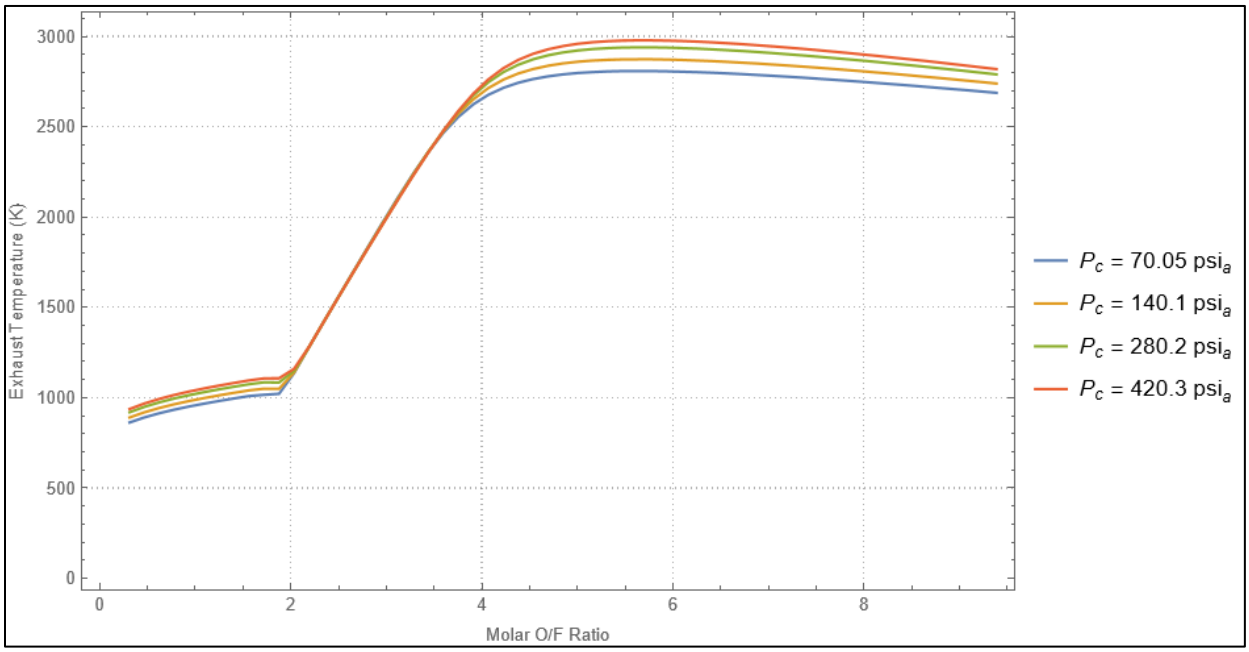

Figure 3.6. Molar O/F Ratio vs. Exhaust Temperature for Multiple Chamber Pressures, Equilibrium & Infinite Area Conditions

Figure 3.7 shows the computed specific impulse as a function of the molar O/F ratio. Note that what CEA reports as the specific impulse in the output file is actually the exhaust velocity, so these values were divided by 9.81 m/s^2 to get the specific impulse as defined in Equation 2.16. At an O/F ratio of ~7 at a chamber pressure of 140.1 psi_a, the specific impulse is almost exactly 200 s, which is somewhat higher than the figure predicted by the design team, which was 177.7 s. Notice that the peak specific impulse does not coincide with the stoichiometric O/F ratio of 6, but rather somewhere around 3.75. This is often the case with

rockets because the mass of the exhaust products also influences the exhaust velocity. This is why LH2/LOx rocket engines often burn fuel-rich instead of stoichiometric, because the unburned LH2 decreases the average molecular mass of the exhaust.

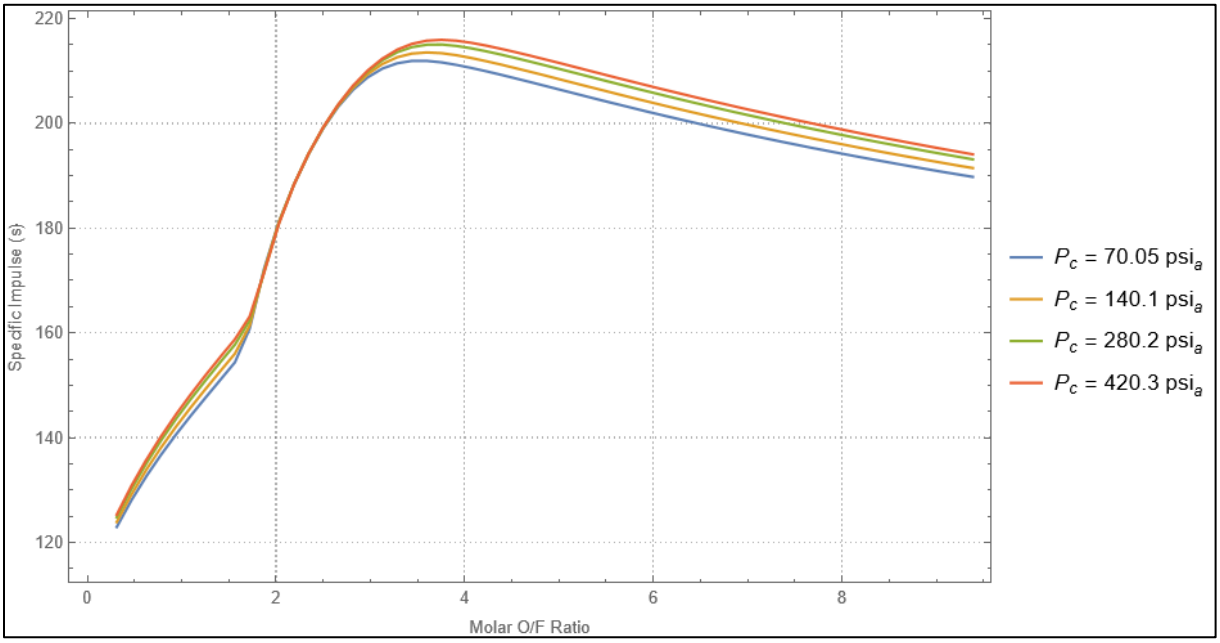

Figure 3.7. Molar O/F Ratio vs. Specific Impulse for Multiple Chamber Pressures, Equilibrium & Infinite Area Conditions

Figure 3.8 shows the c* parameter as a function of the molar O/F ratio. It takes on a profile identical to the specific impulse chart. At an O/F ratio of 7 and chamber pressure of 140.1 psi$_a$, it takes on a value of almost exactly 1600 m/s

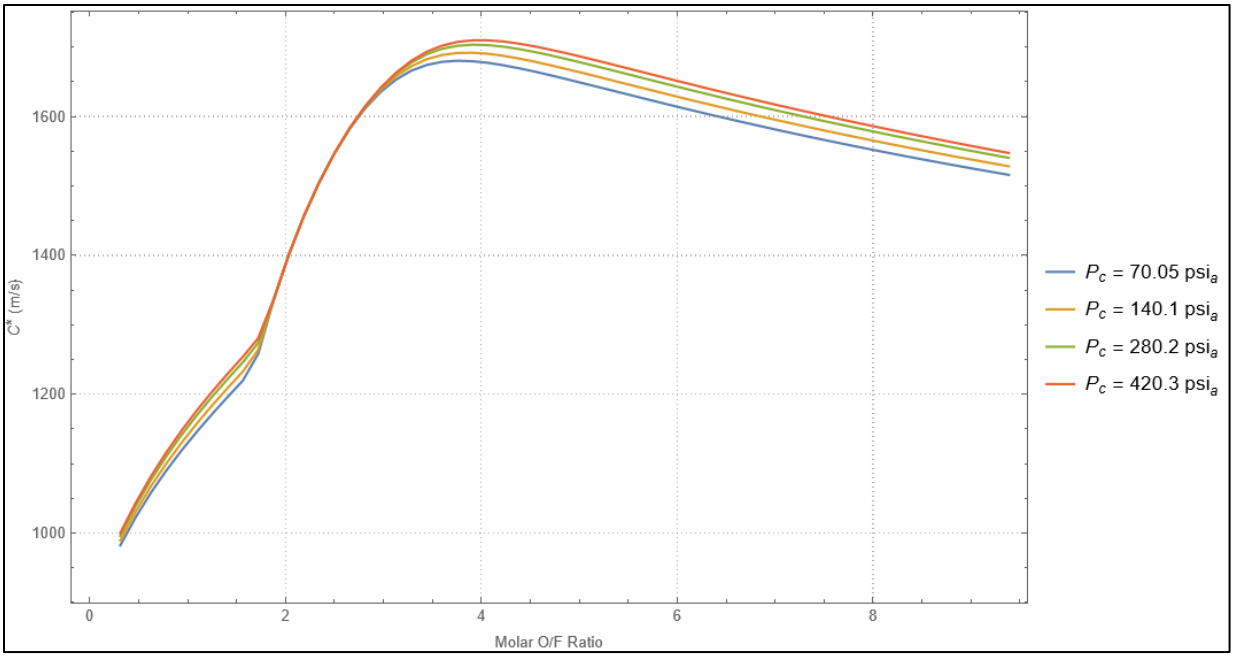

Figure 3.8. Molar O/F Ratio vs. Characteristic Velocity for Multiple Chamber Pressures, Equilibrium & Infinite Area Conditions

Figure 3.9 shows the heat capacity ratio, or the adiabatic index as a function of the molar O/F ratio at the exit of the nozzle. The adiabatic index becomes relatively constant past an O/F ratio of 4. This is most likely because as the combustion goes into the oxidizer rich zone, the combustion products remain relatively unchanged, while more and more excess oxidizer only changes the heat capacity ratio a little bit. As for the heat capacity ratio the design team predicted, there are two conflicting numbers within the documentation they produced. One source states a gamma value of 1.1728, while the MATLAB program they used showed a value of 1.1217. If we take the latter value to be correct, then CEA predicts a slightly lower value of around 1.11 from an O/F value of 6 and onwards.

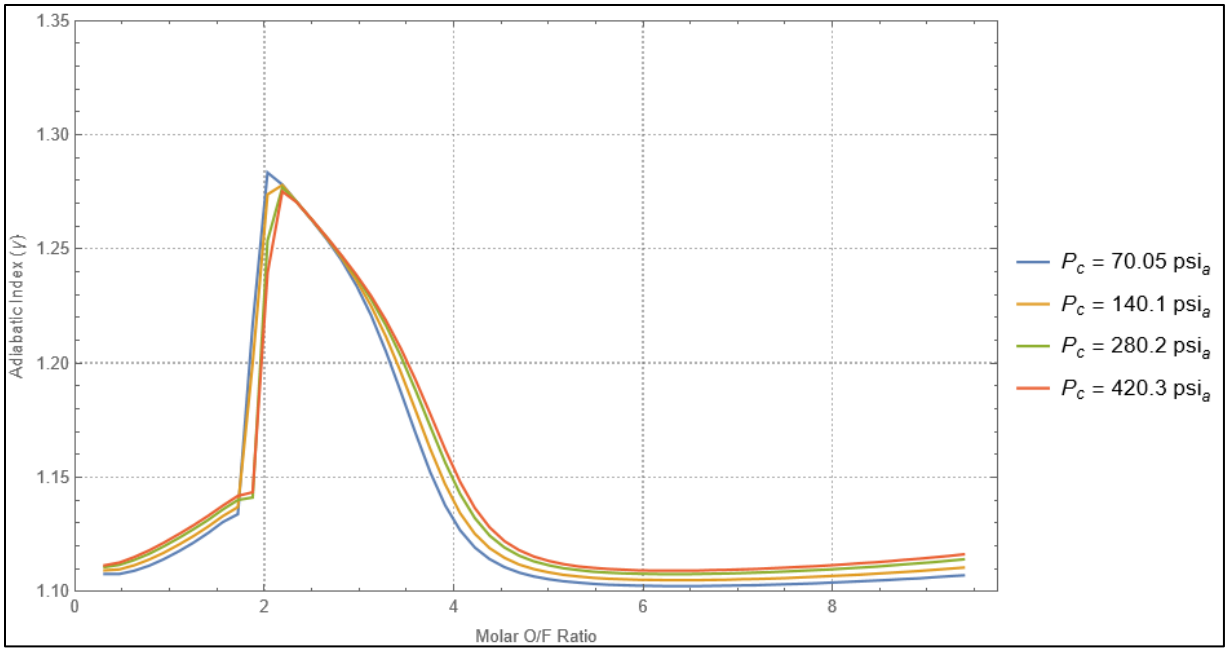

Figure 3.9. Molar O/F Ratio vs Adiabatic Index for Multiple Chamber Pressures, Equilibrium & Infinite Area Conditions

Figure 3.10 shows the thrust coefficient as a function of the molar O/F ratio. It is interesting to note that it shares a similar profile to the adiabatic index. The thrust coefficient remains relatively constant and only varies between a range of 1.23 and 1.27, becoming almost constant beyond an O/F of 4.5.

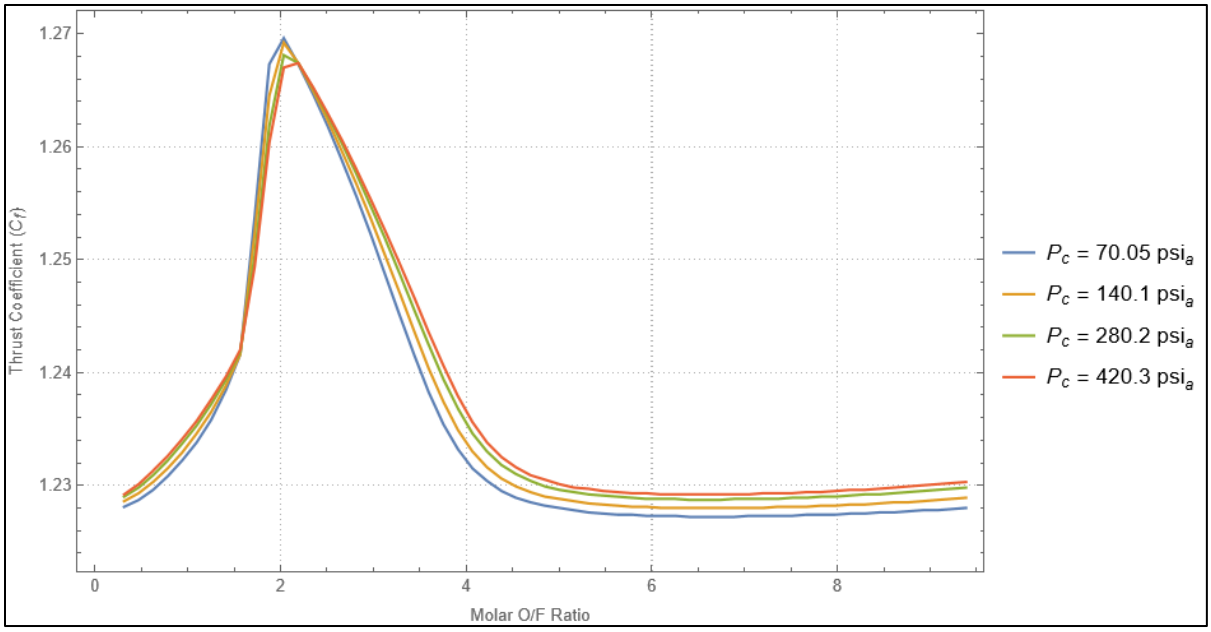

Figure 3.10. Thrust Coefficient as a Function of Molar O/F Ratio, Equilibrium & Infinite Area Conditions

Finally, Figure 3.11 shows the chemical composition of the exhaust at the nozzle exit as a function of the O/F ratio, where free radicals and ionization products are excluded, and only stable chemical species are shown. What is most interesting about this chart is that excess oxygen starts appearing the exhaust mixture much earlier than the theoretical stoichiometric ratio of 6. The design team predicted that at the operating O/F of the NDSU hybrid rocket, the mole fraction of the oxygen in the exhaust mixture would be around 0.09, but CEA predicts a value of around 0.15. Although the design team explicitly acknowledged (Estevadeordal et al, 2021) that they were neglecting carbon monoxide in the exhaust, CEA shows that even at very high O/F ratios, carbon monoxide is present in significant amounts. Although CEA shows that carbon quickly disappears from the exhaust mixture as the O/F rises past 2, testing shows that there is always some soot left over in the hybrid rocket, suggesting that combustion in the fuel grain is not uniform and there are probably different O/F zones within the fuel grain.

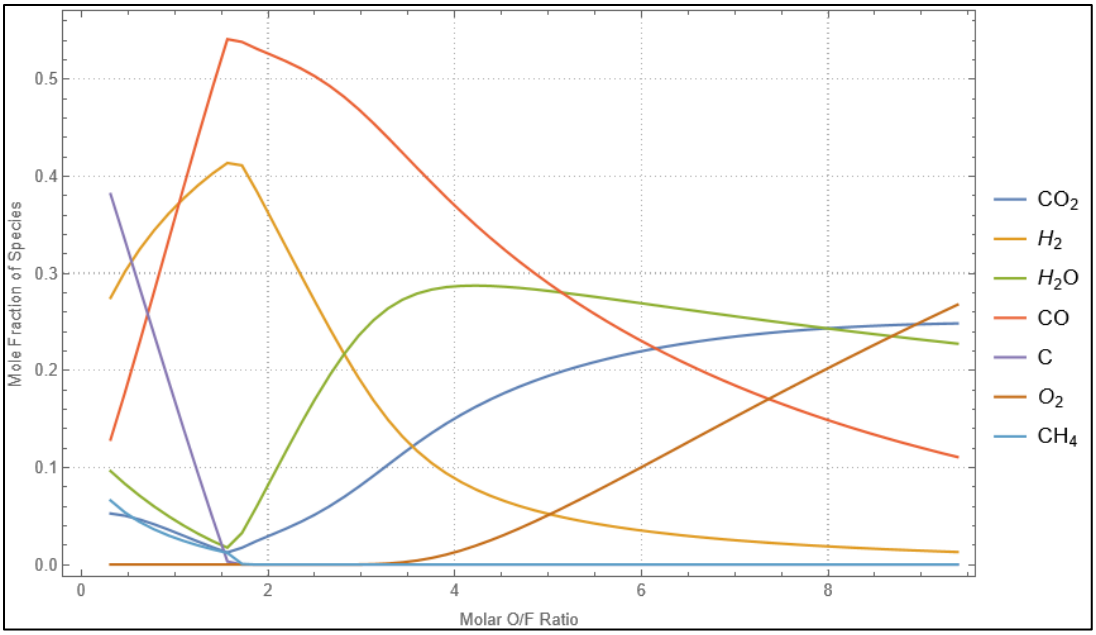

Figure 3.11. Chemical Composition of Exhaust as a Function of Molar O/F Ratio

4. EXPERIMENTAL SETUP

So far, we have discussed the theory of hybrid rocketry and have attempted to predict its performance through theoretical and computational calculations. Now, we reach the 2nd half of this thesis, where we discuss the experimental setup, the testing procedures, and the results.

4.1. Overview of Test Environment

Figure 4.1 (Estevadeordal et al. 2021) shows a labeled schematic of the hybrid rocket itself, while Figure 4.2 shows the test stand, with all the instrumentation labels.

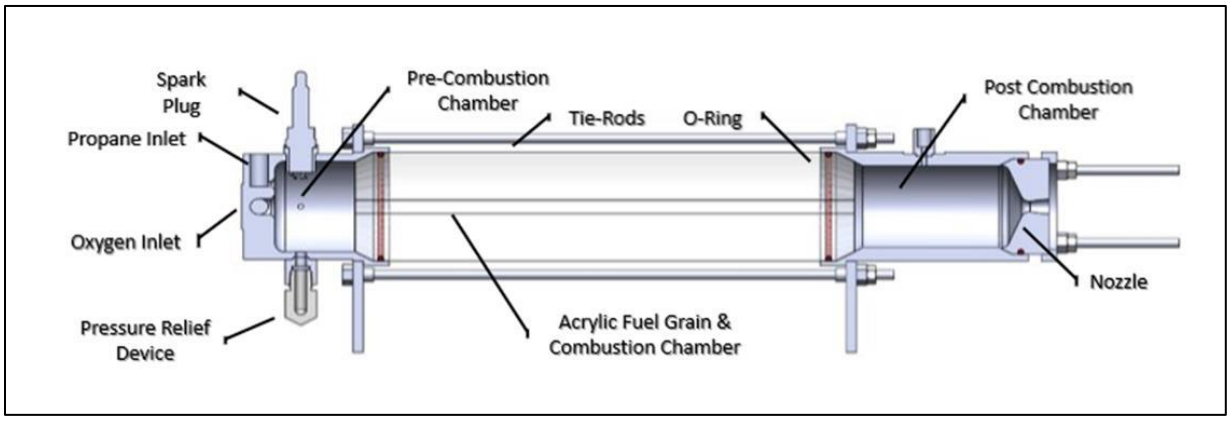

Figure 4.1. Labeled Cutaway View of Hybrid Rocket (Estevadeordal et al., 2021)

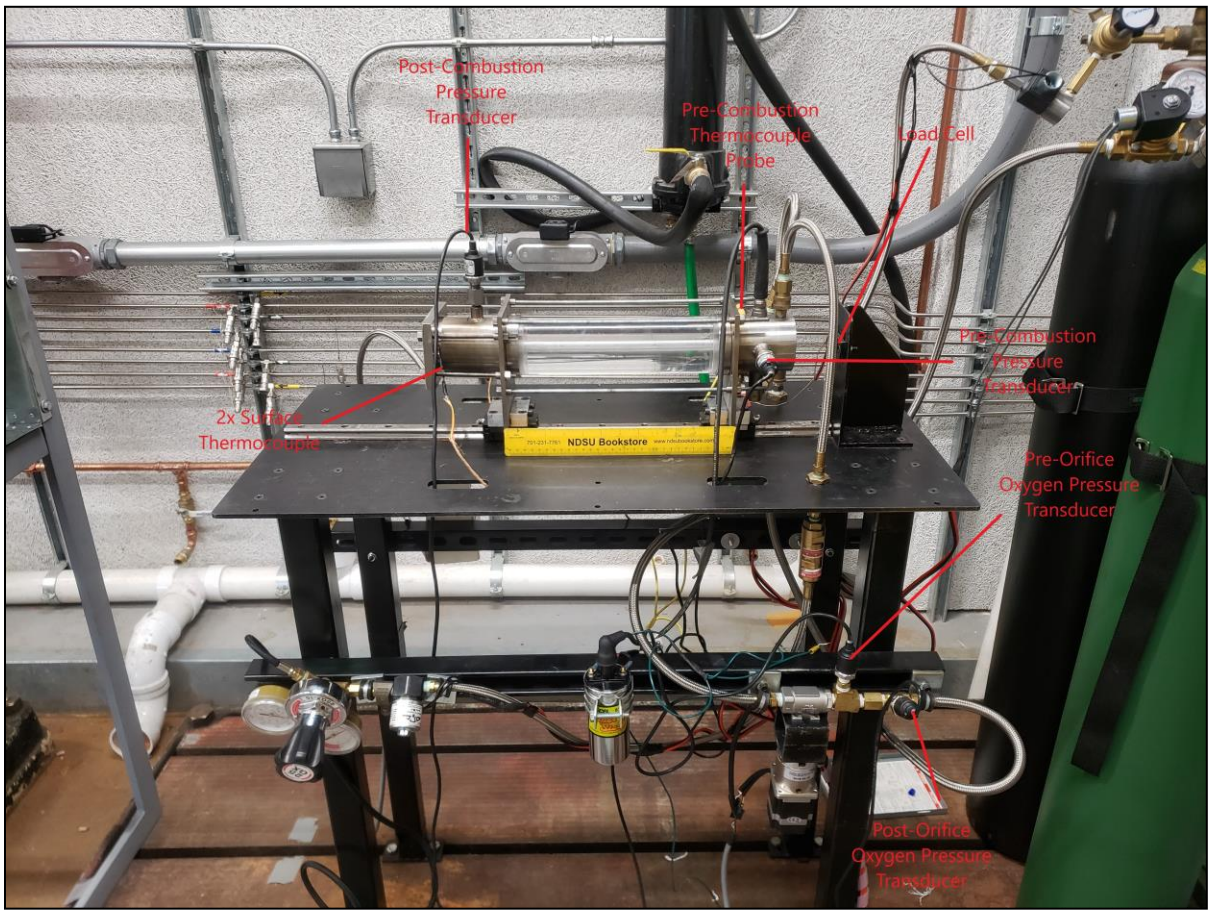

Figure 4.2. Test Stand Without Enclosure with Instrumentation Labels

The test stand was located in a room normally used for engines testing in the NDSU labs. The engine testing bay was ideal for testing a hybrid rocket for a few reasons. The first is that the engines bay comes equipped with an exhaust system that can evacuate 1500 CFM of air from the room. The hybrid rocket was designed to not exceed this volumetric flow rate. (Estevadeordal et al., 2021). The second is that testing can be done remotely from another room so that in the event of a failure or other hazardous event the test participants are relatively safe. There are also pass-throughs from the engine bay to the control room that allow for instrumentation wiring and power cables to be routed through. Additionally, there is a window that allows test participants to

observe the hot-fire from the relative safety of the control room. Finally, the engine bay is equipped with fire extinguishers.

4.2. Oxygen Delivery System

The oxygen feed system has two controllable components, the solenoid on-off switch and a stepper motor attached to a valve which controls the oxygen mass flow rate. The solenoid will close when it is unpowered. The solenoid valve is attached to the oxygen tank regulator so that the flow of oxygen can be stopped at the source. The stepper motor is controlled through an Arduino Uno that uses a 5 V potentiometer as the motor position input. The Arduino takes the potentiometer position and sends the position and velocity data to the stepper motor encoder, which is responsible for providing power to the stepper motor and moving it. There are two parts to the Arduino program, which can be found in its entirety in the Appendix. The first part is the homing sequence, done in the default setup() function. The 2nd part, done in the default loop() function, reads the position of the potentiometer and moves the stepper motor accordingly. The stepper motor has 3 states; closed, partially open, and full open. The limit switch features a plunger with a roller on top of it. The motor shaft has a bushing adapter attached to it such that when the limit switch is installed, the plunger is always depressed. The roller on top of the plunger allows the motor shaft to turn smoothly. There is a machined divot on the bushing where the limit switch plunger can move up enough to trigger the switch. This corresponds to the fully closed position on the valve. It should be noted that although the valve only needs to turn a quarter of a revolution to fully open or close, it can still be rotated 360 degrees. When the Arduino program is executed, the motor will always turn counterclockwise until the limit switch is released, which signals the motor to stop turning. If the motor is already at its zero position, then the homing sequence is skipped.

The oxygen is sourced from a 337 cubic foot, 2400 psi_g oxygen cylinder sourced from Linde. The regulator on the oxygen cylinder allows the low-pressure side to be set up to 500 psi_g. However, for operating the system at a mass flow rate of approximately 0.020 kg/s, the standard operating procedure calls for the regulator to be set to 300 psi_g. The design for the rocket test stand called for a venturi diameter of 0.094 inches, but a venturi diameter of 0.062 inches was installed for unknown reasons. Once this was discovered, the venturi fitting was placed inside an electro-discharge machine and the orifice was increased to a diameter of approximately 0.0955 inches.

4.3. Ignition System

The ignition system consists of two parts, the propane feed system, and the electrical ignition system. The propane feed system uses a simple two-state solenoid to either start or stop the flow propane to the hybrid engine. To get the desired amount of propane flowing into the engine, a single-stage regulator is used to set the pressure to approximately 3.5 psi_g. In the past, a single-stage regulator that went up to 150 psi_g on the low-pressure side was used to set the propane line pressure. However, it was difficult to set the correct working pressure, and too much propane would enter the engine, causing a hard start and bursting the relief valve multiple times. This problem was finally fixed by replacing the burst disc with a resettable poppet valve, which has been used for multiple tests without failing. The electrical ignition system itself is controlled by a 3-position switch. The middle position is a neutral position and is simply a resting state for the switch. The top position charges the electric ignition. The bottom position discharges the ignition system and ignites the propane to start the hybrid rocket.

4.4. Nitrogen Purge System

The nitrogen purge system serves two purposes. It is used to pressurize the hybrid rocket for pressure testing, and it is used to extinguish the rocket when the hot-fire has concluded. The nitrogen purge system is much simpler than the oxygen delivery system and only has an on-off state. The nitrogen source is a 304 cubic foot, 2400 psi_g nitrogen tank sourced from Linde. The regulator on the tank on the low-pressure side goes up to 150 psi_g. When the nitrogen is being used in pressure testing mode, a plug used in placed where the nozzle normally goes to seal the system. The regulator is then opened all the way to pressurize the system to 150 psi_g for leak-checking. After leak checking has concluded, a ball valve is opened to depressurize the system. This ball valve was added to the system after the design team finished construction of the hybrid rocket to facilitate easier pressure testing. Before, standard procedure called for loosening one of the feed hoses to depressurize the system.

4.5. Instrumentation

4.5.1. Load Cell

The hybrid rocket sits on a set of linear bearings that allow it to move freely. When the rocket is under thrust, it pushes into the load cell. The load cell that has been used to measure the thrust output of the hybrid rocket motor since the summer of 2021 is the FX-1901 25lbf model. After the previous loadcell that was used for the first few tests was damaged, the FX-1901 was selected as a replacement due to its low price of roughly $25 compared to the $250 price tag for the previous load cell. The load cell calibration procedure was as follows. First, the zero offset of the load cell was determined by recording the voltage generated without any load present. This offset was then programmed into LabView to zero the loadcell. A set of weights ranging from 1

to 20 lbf was then used to generate a calibration curve in 1 lbf increments. Figure 4.3 shows the weights that were used.

Figure 4.3. Calibration Weights

Of course, since the FX-1901 has a tiny load connection, it was necessary to carefully balance the weights on the load cell. In the future, a more sophisticated calibration setup will be needed so that the weight of the person's hand balancing the weights doesn't introduce error in the measurements. The load cell voltage response for each weight was recorded with LabView and then averaged. A weight-voltage plot was generated and a linear regression was run to determine the calibration coefficient. This coefficient was then programmed into LabView. Later on, it was found that using so many weights for the calibration didn't necessarily improve the accuracy of the calibration, so the number of datapoints was dropped to 5. After the first FX-1901 load cell was broken by inadvertently pushing the hybrid rocket into it too hard, the backup FX-1901 was calibrated using a two-point calibration, where the 1st point was the zero offset, and the 2nd point was close to 25 lbf. Figure 4.4 shows one of the calibration plots. The full calibration process can be found in the Appendix section.

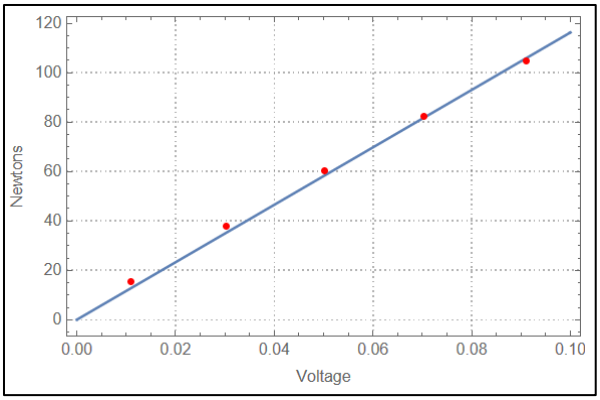

Figure 4.4. One of the Calibration Curves for the FX-1901

4.5.2. Pressure Transducers

One of the improvements made to the test stand over the summer of 2022 was the addition of more digital pressure transducers. The pressure transducer model used for all pressure measurements was the ProSense SPT-25. At the beginning, there was only one in use and it was used to measure the pre-combustion pressure. The rest of the pressure measurement points, such as the post-combustion chamber, used analog pressure gauges. These were not ideal, as the brightness of the fuel grain combusting made them difficult to see, especially on video recordings of the hot-fires. In order to accurately characterize the performance of the hybrid rocket, the oxygen mass flow rate needed to be known. That's why the two analog pressure gauges that were used to measure the upstream and downstream pressures of the orifice device were replaced with digital pressure transducers. This allows for the oxygen mass flow rate to be precisely calculated as a function of time. As for the post-combustion chamber, there was initially some concern about a digital pressure transducer being subjected to extreme conditions. However, given that an analog pressure gauge was used multiple times for post-combustion pressure measurements and survived, it was thought that there was a good chance that the post-combustion digital pressure transducer would survive as well. It turns out that digital pressure transducers are less robust than analog pressure gauges, and the post-combustion digital pressure

transducer only worked for 3 hot-fires before breaking. The calibration process for the SPT-25 transducer is simple. The SPT-25 produces a voltage signal that is linearly proportional to the pressure measured. The SPT-25 produces an output voltage in the range of 0-10 VDC. Each model also has a specified pressure range. So, the calibration coefficient is calculated by dividing the max value of the pressure range by the max value of the voltage range. Additionally, the pressure transducer output is measured at zero load to determine the zero offset so that they can be zeroed. The pressure transducers were then validated by comparing their measurements to the measurements produced by analog pressure gauges and they were found to produce good results.

4.5.3. Thermocouples

All thermocouples used in the course of testing were type-K. Initially, the test stand had 3 temperature measurement points. These were the pre-combustion, post-combustion, and exhaust regions. Being able to measure the post-combustion temperature would allow for the total mass flow rate to be calculated using Equation 2.10. If both the chamber temperature and the chamber pressure were known over time, and the oxygen mass flow rate were also known over time, then the instantaneous fuel mass flow rate of the fuel grain could be calculated. However, it is nearly impossible to directly measure the post-combustion temperature because the combustion process with pure oxygen produces temperatures well over 3000 K, which exceeds the melting point of most known materials. Figure 4.5 shows the state of a thermocouple probe after it was inserted into the post-combustion region of the hybrid rocket. The thermocouple was a Type-K thermocouple probe with an Inconel sheath.

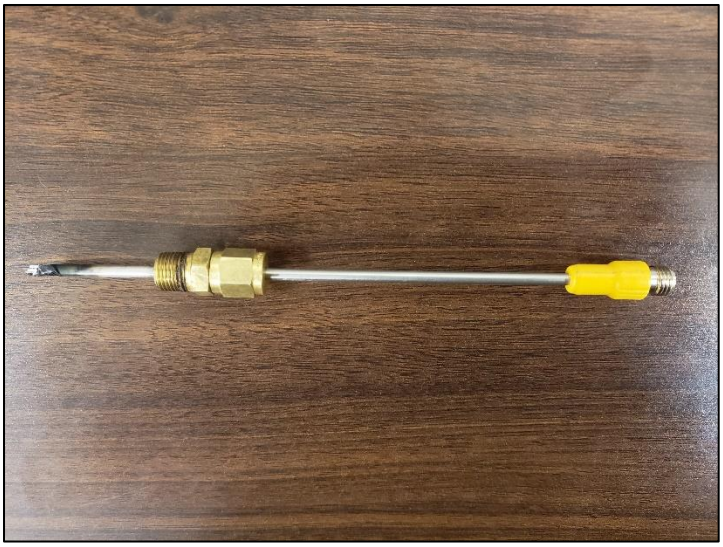

Figure 4.5. Thermocouple Probe After Insertion Into Post-Combustion Region

It quickly became apparent that directly measuring the chamber temperature was out of the question. Measuring the exhaust temperature also proved to not be useful. At first, a thermocouple probe was placed near the nozzle exit to measure this quantity. It suffered the same fate as the post-combustion thermocouple probe. A new thermocouple probe was then used to measure the exhaust temperature approximately 6 inches away from the nozzle exit. While the thermocouple probe didn't melt, it was clear that it was reaching the end of the type-K temperature range. The exhaust was almost certainly hotter that what the thermocouple probe could measure. The pre-combustion thermocouple probe, however, continued to produce good, if noisy measurements over the course of the testing program. Since there was room on the DAQ for two more thermocouple measurements, it was decided to try and measure the nozzle surface temperature in two places for the rest of the testing program. For a few tests, an off-the-shelf thermocouple reader with a type-K thermocouple wire was also used to measure the surface temperature of the nozzle during the test. The thermocouples were validated by taking measurements of near-boiling water and then comparing their measurements to an off-the-shelf

thermocouple reader. The results were found to be acceptable. One problem with the thermocouples is that the measurements produced from them are very noisy compared to the other measurements such as the load cell and the pressure transducers. The cause of this was never determined. This necessitated the use of aggressive low-pass filtering of the collected data.

4.5.4. Cameras

The purpose of the cameras in the testing program was two-fold. First, cameras were used to record the overall hot-fire process. This proved useful because more than once, camera footage was used to determine what went wrong during a hot-fire. For example, when the hybrid rocket produced dismal thrust during one hot-fire, the footage was analyzed and it was found that the igniting propane caused the burst disc used as a pressure relief device to break, which caused most of the oxygen to leak out uselessly. Second, cameras were the means by which the regression of the fuel grain port was measured. 3 different camera models were used to accomplish this, with varying degrees of success. The first camera model used was LaVision Imager LX PIV camera equipped with a 50 mm fixed-focal length lens. The second camera model was a Samsung Galaxy Note 9 smartphone, and the third was a Photron Fastcam S12 high speed camera. An older high-speed camera, a TSI Nanosense III, was used for a few tests, but the imagery from that was not analyzed.

4.6. Data Acquisition

Data acquisition was accomplished through a National Instruments USB-3008 DAQ, which was used with a LabView program to record all data. The LabView program was originally created by the design team for the rocket, but was modified during the course of the testing program to accommodate more instrumentation. One of the pressing problems with the data acquisition system was the low sampling rate. The DAQ is advertised as being capable of up

to 20 kS/s, but with all the channels in use, the best data sampling rate that could be achieved was ~25 Hz. The problem most likely lies in the LabView program itself, which will need to be addressed in future testing programs. Figure 4.6 shows the LabView Front Panel. Using Labview in this configuration allowed for the rocket performance to be seen in real time, and also enhanced safety because the rocket could be shut down in the event the readings showed something anomalous.

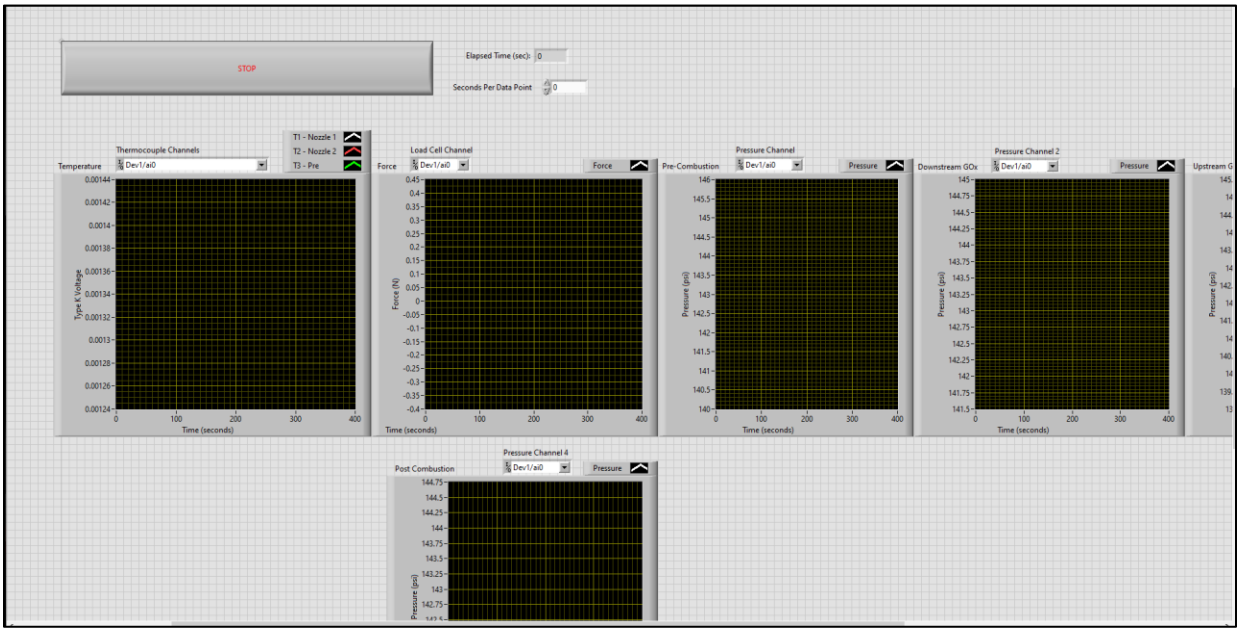

Figure 4.6. LabView Front Panel

4.7. Testing Procedures

Testing was always conducted with at least 3 people for safety reasons. Typically, one person would be responsible for operating the rocket, another would standby with a fire extinguisher in case of a fire, and one would be responsible for operating the imaging equipment, such as the high-speed camera. Before conducting a hot-fire, a pre-test checklist was run through, to make sure that the rocket was safe to test, and that the environment was safe to test in. This included verifying that all bolts were secured with the appropriate amount of torque,

verifying that all gas cylinders were properly affixed to the walls, leak checking the test stand every time a fuel grain was switched out or a major component replaced, and removing all combustibles from the engine bay. After the pre-check list was completed and everyone evacuated from the room, the system was purged with nitrogen for 5 seconds. After the nitrogen purge, the oxygen solenoid would be opened, which would allow oxygen to flow from the tank to the motorized ball valve, which at this point would be closed. The propane solenoid would then be opened to allow a small amount of propane to start flowing through the motor. The stepper motor would then be turned to the "Start" position, which opened the ball valve slightly to allow a small amount of oxygen to start flowing through the motor along with the propane. The ignition switch would then be toggled rapidly to alternatively charge the sparkplug and discharge it until ignition occurred. Once ignition occurred, the propane would be switched off and the stepper motor would be turned to the "Full" position, which allowed for the full mass flow rate of oxygen to be achieved. The rocket would then be run for 10-20 seconds, before being extinguished by hitting the "E-stop" button, which cuts power to the entire system. When this happens, the oxygen solenoid closes, cutting off the flow of oxygen to the motor, and the nitrogen solenoid opens, purging the system with nitrogen to fully extinguish any remaining burning materials. The engine bay exhaust system is then allowed to operate for 5 minutes to ensure that all combustion products have been evacuated from the room. After that, it takes approximately one hour before the rocket is cool enough to handle and disassemble.

5. EXPERIMENTAL RESULTS

5.1. Summary of Results

Including the first two hot-fires conducted in November 2020, a total of 20 hot-fires have been conducted since November 2020. Not all of these generated usable data however. Out of the 20 hot-fires conducted, 6 of them did not generate valid data. One of these was due to forgetting to start the data acquisition on LabView. The rest were due to the relief valve bursting after the propane was ignited. Although data was collected during these tests where the relief valve had burst, these tests were excluded. Table 5.1 summarizes all the data gathered from tests conducted since 07-09-21. The color coding on the table indicates that the same fuel grain was used for multiple tests. For example, the tests conducted on 05-04-22 and 05-16-22 used the same fuel grain. Oxygen mass flow rates that have a tilde next to the figure indicate that the figure is approximate, since those tests were using analog pressure gauges for the upstream and downstream oxygen line pressures. The table shows the calculated average for each instrument and the max value recorded by the instrument. Although the orifice upstream and downstream pressures are not shown, the oxygen mass flow rate for each test was calculated from these measurements according to Equations 2.35 and 2.36, using the absolute pressure. Table 5.2 summarizes the average fuel grain mass flow rates for each test. The fuel grains were weighed before and after they had been used up. The average fuel mass flow rate was then calculated by dividing the difference in weight by the time elapsed for each test. Since the fuel grains were typically used for two hot-fires each, the times for each test were added together.

Table 5.1. Summary of Test Results

Test	Average Thrust (N)	Max Thrust (N)	Average Pre-Combustion Pressure (kPa(g))	Max Pre-Combustion Pressure (kPa(g))	Average Post-Combustion Pressure (kPa(g))	Max Post-Combustion Pressure (kPa(g))	Average O_2 mass flow rate (kg/s)	Average Pre-Combustion Temperature (C)	Max Pre-Combustion Temperature (C)	Time (s)
07-09-21	8.11944	11.9681	350.5	429.565	n/a	n/a	~0.0084	418.622	554.075	n/a
11-29-21	9.87243	12.0603	404.592	446.581	n/a	n/a	~0.0084	406.305	619.241	16.5
12-18-21	28.6886	39.3397	663.811	828.036	n/a	n/a	~0.020	285.631	452.912	5.17
05-04-22	29.9102	35.8758	667.374	783.08	n/a	n/a	~0.020	238.989	364.44	9.72
05-16-22	23.2297	27.5805	498.128	597.321	n/a	n/a	~0.020	117.844	171.31	16.4
08-25-22 1	8.24903	10.4635	365.292	403.602	n/a	n/a	0.009354	437.013	633.583	11.85
08-25-22 2	10.3677	13.4831	347.014	383.335	n/a	n/a	0.009441	200.823	268.656	13.93
09-23-22 1	10.7524	13.2934	408.242	438.424	397.826	436.992	0.01011	417.093	597.449	19.55
09-23-22 2	8.10859	10.9265	356.891	399.18	357.08	394.984	0.009902	152.634	221.867	14.31
10-11-22	27.7733	34.8756	721.966	831.005	695.573	775.883	0.01962	284.381	388.585	9.42
10-13-22	22.3706	26.3059	635.109	666.983	n/a	n/a	0.02135	136.134	176.741	11.46
10-27-22	35.5465	41.5118	667.832	868.954	n/a	n/a	0.02086	226.716	496.157	25.9

Table 5.2. Fuel Grain Mass Flow Rate Summary

Test	Initial Mass	Final Mass	Delta-t	$\overline{\dot{m}_f}$
11-29-21	1596.2 g	1499.8 g	16.5 s	0.005842 kg/s
12-18-21	1603.9 g	1552.6 g	5.17 s	0.009923 kg/s
05-04-22	1535.8 g	1444.4 g	9.72 s	0.00914 kg/s
05-16-22	1444.4 g	1347.1 g	16.4 s	0.006486 kg/s
08-25-22 1&2	1607.7 g	1482.5 g	25.78 s	0.004856 kg/s
09-23-22 1 & 2	1605.8 g	1438.0 g	33.86 s	0.0049557 kg/s
10-11-22 & 10-13-22	1608.4 g	1431.85 g	20.88 s	0.008455 kg/s
10-27-22	1604.9 g	1403.8 g	25.9 s	0.007764 kg/s

5.2. Imagery of Fuel Grain Combustion

Here, images from a hot-fire conducted on October 27th, 2022 are shown. Figure 5.1 shows the hybrid rocket just after ignition has occurred, but before the oxygen is turned up to the full mass flow rate. Figure 5.2 shows the rocket just after the oxygen has been turned up to 100%, Figure 5.3 shows the steady-state operation of the rocket. Figure 5.4 shows the rocket just after shutdown. These images taken from the video footage of the hot-fire conducted on 10-27-22 show the difficulty in capturing the boundaries.

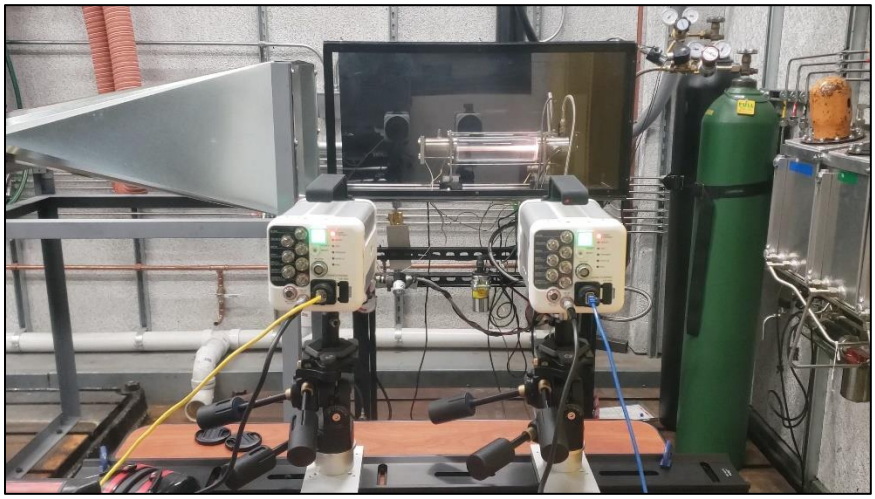

Figure 5.1. Ignition, 10-27-22 Test

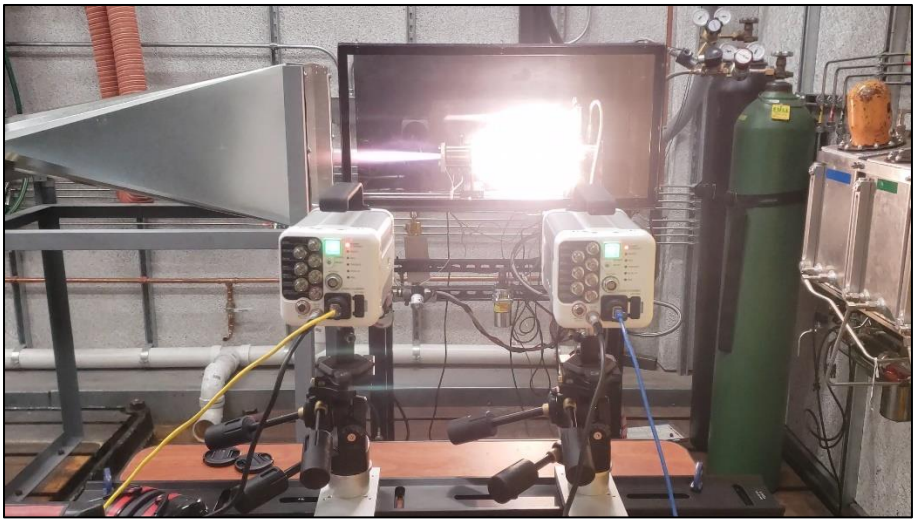

Figure 5.2. The Moment of 100% Oxygen Mass Flow Rate, 10-27-22 Test

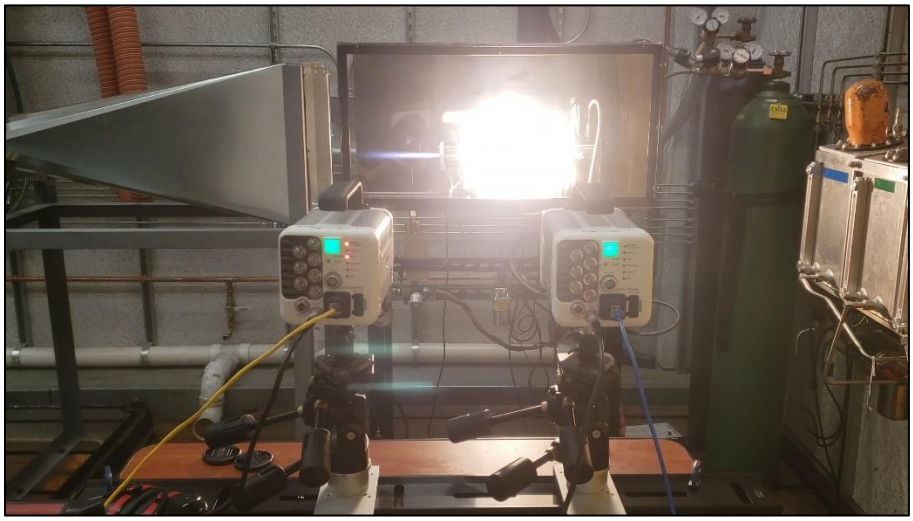

Figure 5.3. Steady State Operation, 10-27-22 Test

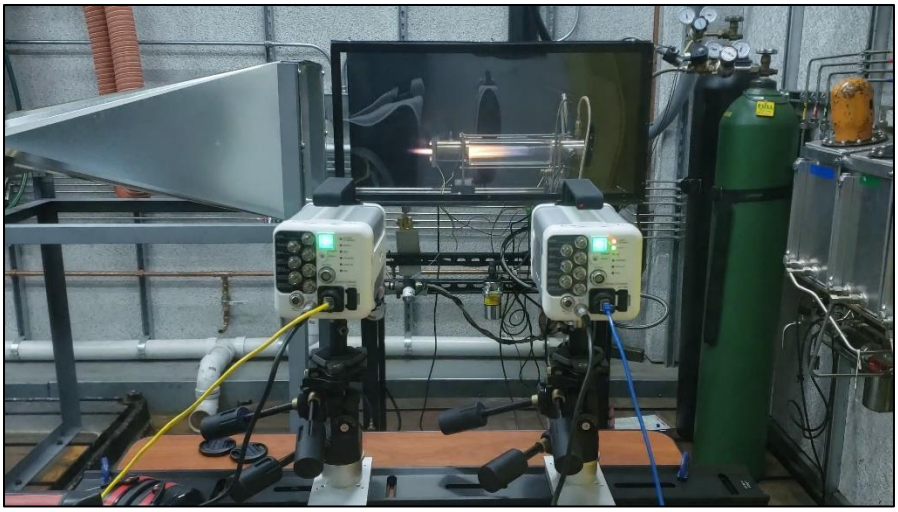

Figure 5.4. Shutdown, 10-27-22 Test

Figure 5.5 is an image taken by the LaVision PIV camera. The PIV camera can be calibration for distance and the images printed with an X & Y scale so that measurements can be taken. Initially, regression measurements were done with these PIV camera image sets, but because the fuel grain boundary is somewhat unclear, it was decided not to use these measurements. Using a very low exposure time, the PIV camera can resolve the flame structures within the fuel port. The PIV camera was used for the hot-fires conducted on 05-04-22 and 05-16-22.

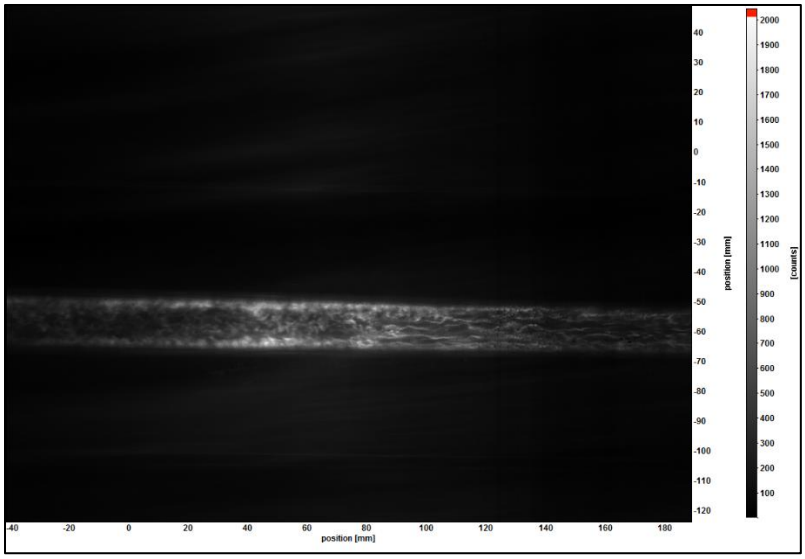

Figure 5.5. PIV Image Capture of Fuel Grain

Figure 5.6 shows an image of the fuel grain burning that was taken with a Samsung Galaxy Note 9 camera. This particular image was taken from 09-23-22 Test #1. Even though it's not a professional solution, the image sets taken with the smartphone turned out surprisingly well. The Samsung Galaxy Note 9 camera app has a professional mode that allows for the shutter speed, aperture, and ISO to be user controlled. The Galaxy Note 9's camera is capable of shutter speeds up to 1/6000 s, which allows for the fuel port boundaries to be clearly seen. Some of the flame structures can even be resolved a little bit. Mach diamonds are also visible in the nozzle exhaust, which indicates that flow is supersonic, and a little over-expanded. All videos were taken using a shutter speed that varied between 1/4000-1/6000 s, the most open aperture setting, and an ISO between 50-100.

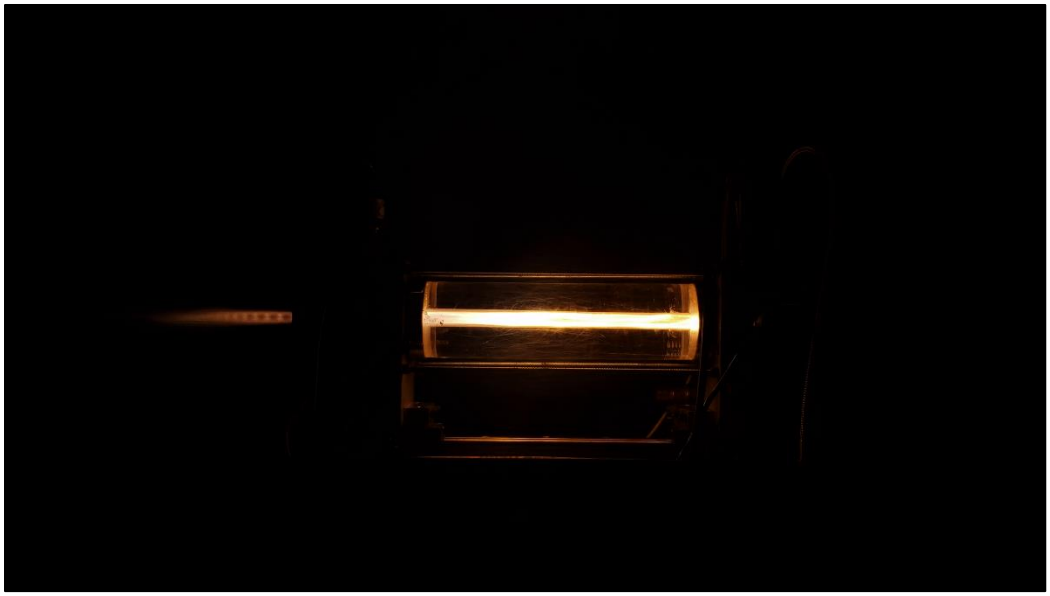

Figure 5.6. Image of Burning Fuel Grain, Taken with Galaxy Note 9 Smartphone

Figures 5.7 and 5.8 show images that were captured from the Photron Highspeed camera. Figure 5.7 is taken from the 10-11-22 Test and Figure 5.8 is taken from the 10-13-22 Test, both used the same fuel grain. The imagery from the 10-11-22 test was somewhat overexposed, while the imagery from the 10-13-22 test was still overexposed, but the fuel port boundaries can be seen clearly. A framerate of 2000 fps was used for the imagery sets generated using the Photron high speed camera, which has a maximum resolution of 1024x1024 pixels at that framerate. What was striking about the high-speed imagery was that near the end of fuel port, a gap between the combusting fuel and the fuel port boundary can be seen for the first couple of seconds the rocket is running.

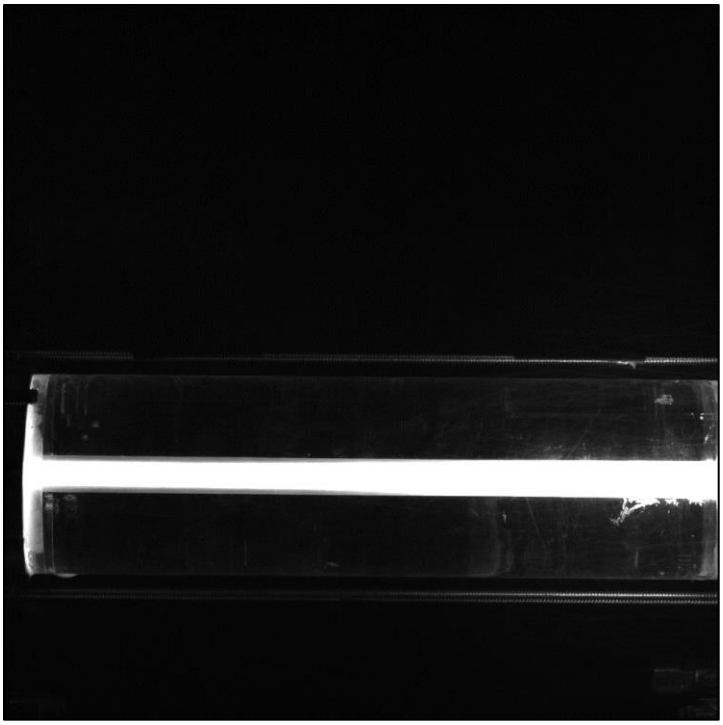

Figure 5.7. Image Taken from High-Speed Recording of Fuel Grain Early in Burn

Figure 5.8. Image Taken from High-Speed Recording of Fuel Grain Late in Burn

5.3. Thrust Measurements

Figure 5.9 shows a thrust profile that is typical for the hybrid rocket operating at an oxygen mass flow rate of ~0.010 kg/s and was taken from the 1st 09-23-22 hot-fire, while Figure 5.10 shows a thrust profile that is typical for the hybrid rocket operating at an oxygen mass flow rate of ~0.020 kg/s, and was taken from the 10-27-22 hot fire. All the thrust plots can be found in Appendix Figure A12. When the rocket was fired with an oxygen mass flow rate of 0.010 kg/s, the thrust typically averaged around 10 N. When the rocket was test fired with an oxygen mass flow rate of 0.020 kg/s, the rocket would usually peak between 30-40 N and would slowly decrease. When a 2nd hot-fire would be conducted with an oxygen mass flow rate of 0.020 kg/s using the same fuel grain, the thrust would average around 25 N. Strangely, a few tests showed the thrust rising over time. The average thrust produced at an oxygen mass flow rate of 0.020 kg/s is somewhat below what was expected in the original design. One hypothesis on this is that the end of the rocket may not be making good contact with load cell, which has a tiny load connection, and any object pressing on it must press on it squarely and not at an angle, or else the load cell will undermeasure the force.

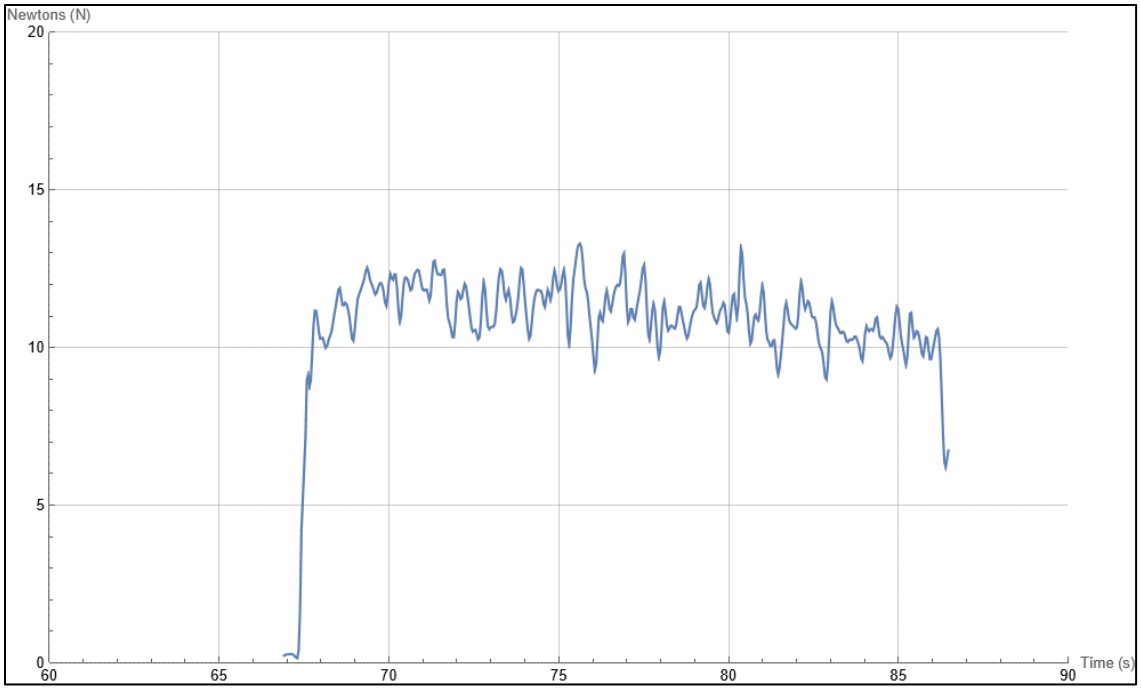

Figure 5.9. Thrust Profile of 09-23-22 Test #1.

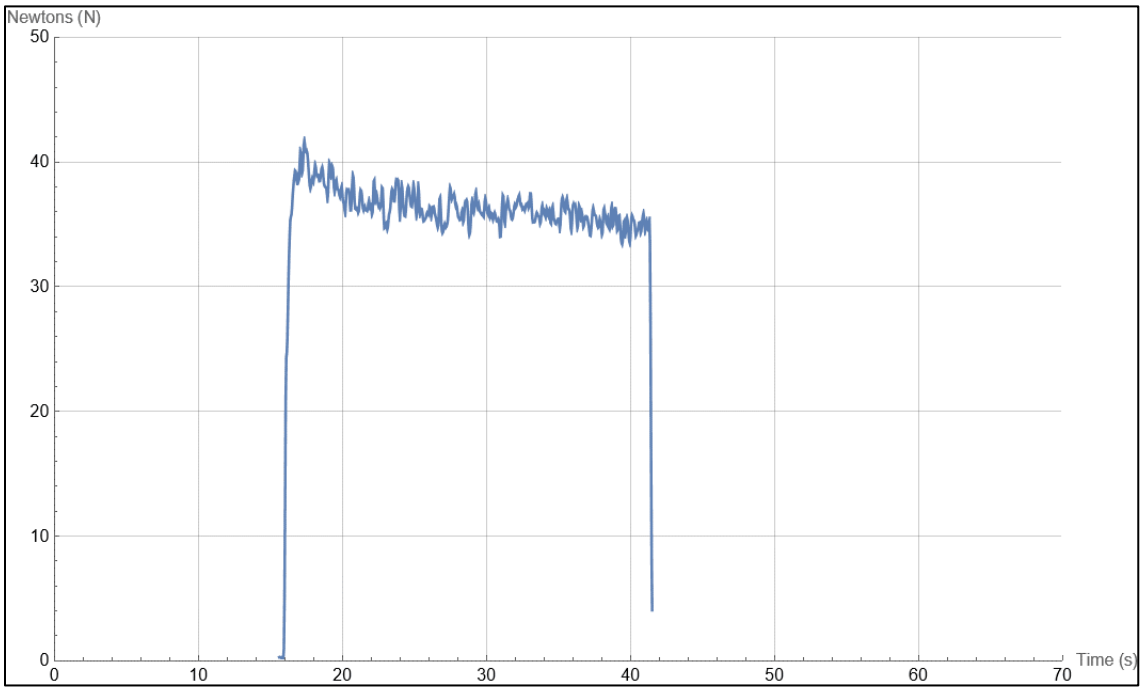

Figure 5.10. Thrust Profile of 10-27-22 Test

5.4. Pressure Measurements

Figure 5.11 shows a pre-combustion pressure profile that was taken from the 09-23-22 1st test fire, where the oxygen mass flow rate was 0.010 kg/s, and Figure 5.12 shows a pre-combustion pressure profile taken from the 10-27-22 test fire. Like the thrust profiles, the pre-combustion pressure generally decreased over time as the hot-fire progressed, although there were a couple of tests where the pressure seemed to rise or stay constant. Generally though, the pre-combustion pressure would peak around 60 psi_g for an oxygen mass flow rate of 0.010 kg/s, and would peak at roughly 120 psi_g for an oxygen mass flow rate of 0.020 kg/s. Figure 5.13 plots both the pre and post combustion pressure profiles together, also from the 09-23-22 1st test fire. The post-combustion pressure starts out lower than the pre-combustion pressure, but as the hot-fire progresses, they both converge together. This behavior seems typical for hybrid rockets. Figure 5.14 shows the pre and post combustion pressure profiles plotted together for a hybrid rocket that was tested by Narsai (Narsai, 2016), which shows similar behavior to the pressure profiles shown in 5.13. Unfortunately, the post-combustion pressure transducer only worked for 3 hot-fires before failing during the 4th hot-fire it was used in. Measuring the temperature of the post-combustion pressure transducer housing after one of the hot-fires showed that the housing was close to 100 °C, and this was roughly 5 minutes after the test, when the rocket had some time to cool off. If the outer housing was getting that hot, then the inner part almost certainly exceeded the maximum operating temperature of 125 °C. Evidently, digital pressure transducers are more sensitive to heat than analog pressure gauges are. These pressure transducers are expensive, so for future post-combustion measurements, it will be necessary to either find another pressure transducer capable of higher operating temperatures, or increase the distance from the post-combustion chamber to the pressure transducer.

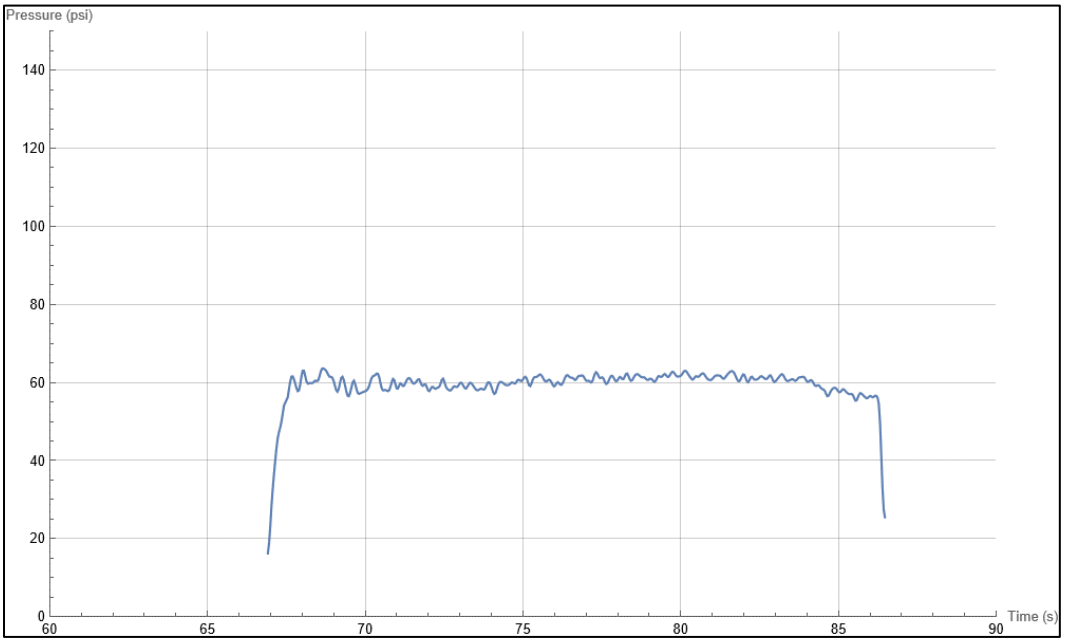

Figure 5.11. Pre-Combustion Pressure Plot of 1st 09-23-22 Hot-Fire

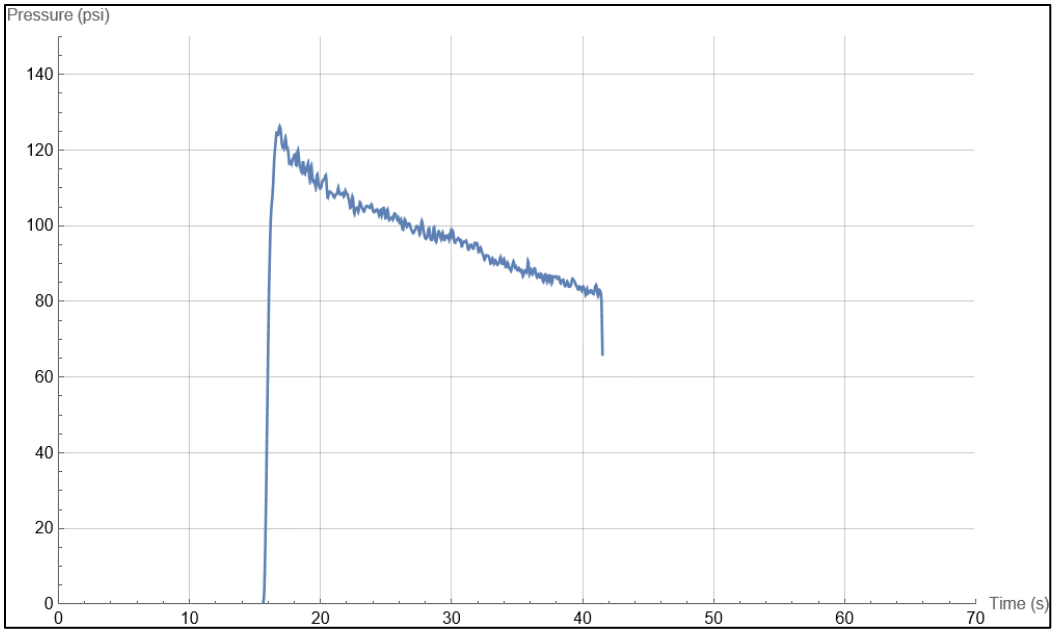

Figure 5.12. Pre-Combustion Pressure Plot of 10-27-22 Hot-Fire

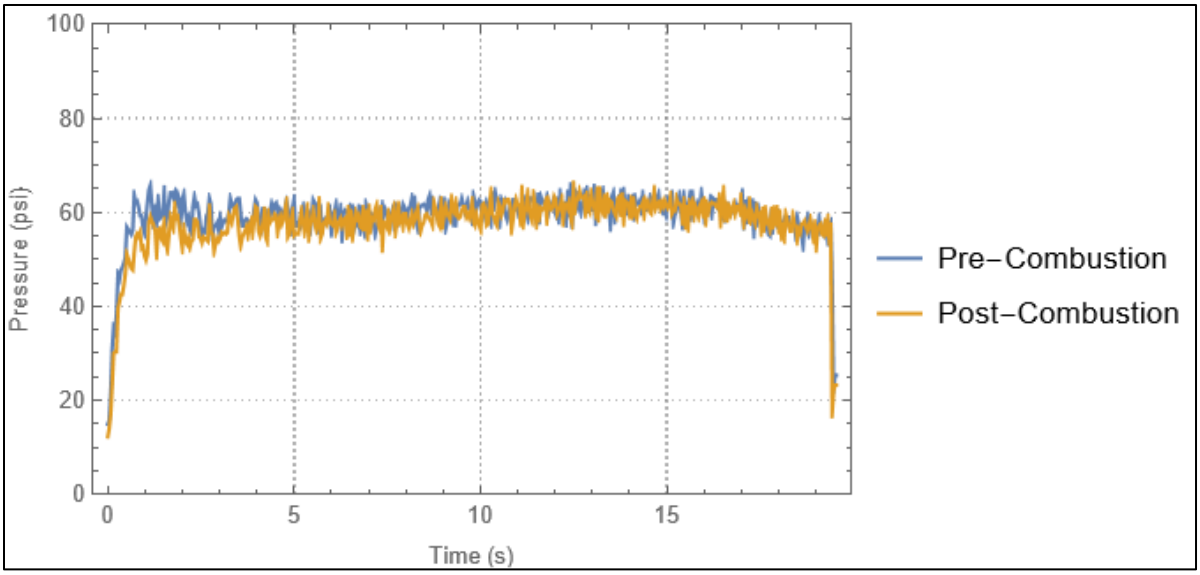

Figure 5.13. Pre and Post Combustion Pressures Plotted Together, 09-23-22 Test #1

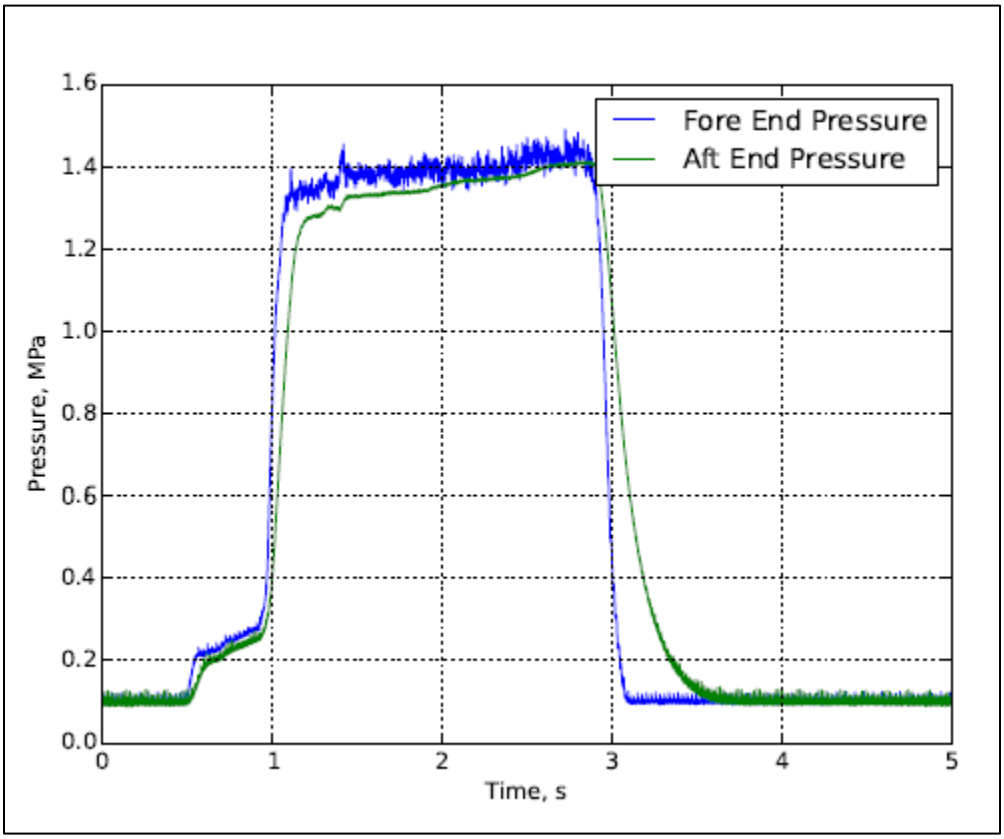

Figure 5.14. Pre and Post Combustion Pressures Plotted Together (Narsai, 2016)

5.5. Temperature Measurements

Of all the temperature measurements taken, the pre-combustion temperature measurements proved the most reliable. Figure 5.15 shows the pre-combustion temperature profile for 09-23-22 Test #1. Figure 5.16 shows the pre-combustion temperature profile for the 10-27-22 Test. For most tests that were conducted with an oxygen mass flow rate of 0.010 kg/s, the pre-combustion temperature typically peaked at 500 to 600 °C, while tests that were conducted with an oxygen mass flow rate of 0.020 kg/s typically showed a lower peak temperature of 400 °C. This is because the oxygen flows directly over the thermocouple probe inside the pre-combustion chamber, and higher oxygen mass flow rates cool the probe via convection. For long tests such as the 10-27-22 test, the temperature tends to drop then settle at a steady state.

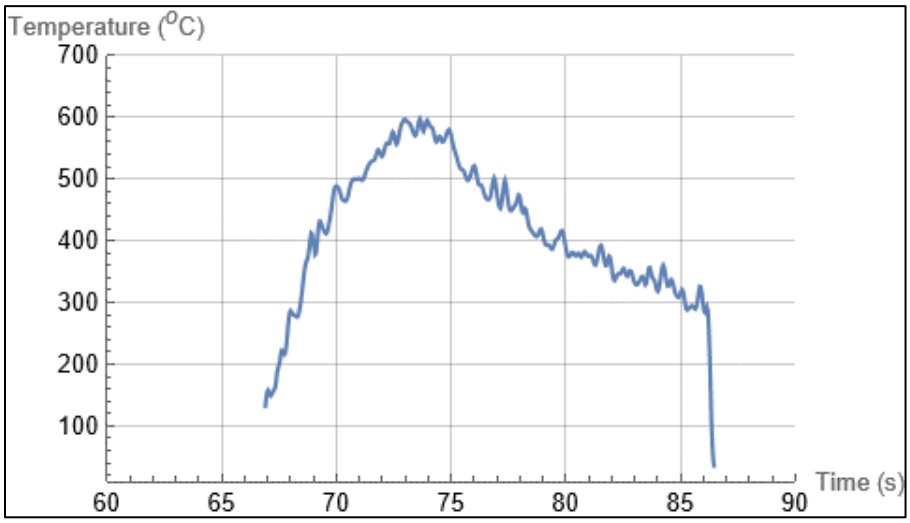

Figure 5.15. Pre-Combustion Temperature Profile, 09-23-22 Test #1

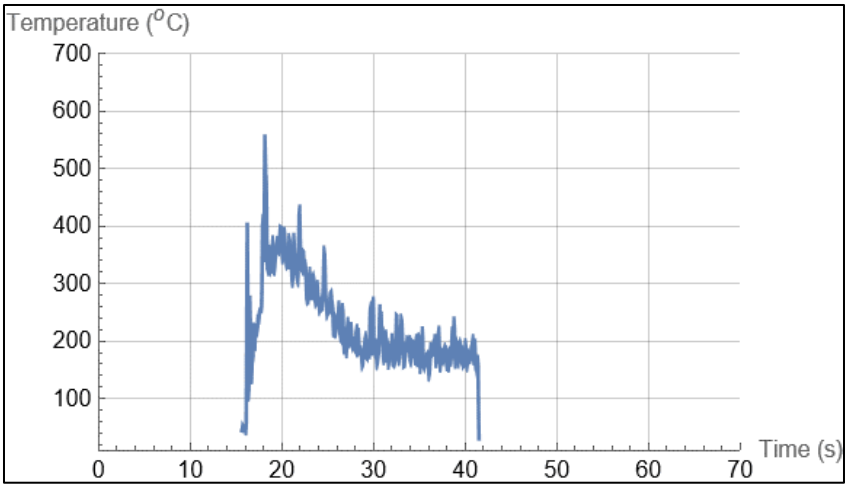

Figure 5.16. Pre-Combustion Temperature Profile, 10-27-22 Test

Unfortunately, the nozzle surface temperature measurements taken through LabView proved to be unreliable. Either the thermocouples wouldn't record anything at all, or they would suddenly start recording temperature data during a test. This might be because the surface probes were not making good contact with the nozzle surface and there wasn't a way to ensure they stayed firmly pressed against the surface. At one point, thermowells were drilled into a graphite nozzle in an attempt to solve this problem, but this nozzle was never used because there was some concern about the nozzle's structural integrity. The peak temperature shown during any of these tests was at most ~150 °C. Figure 5.17 shows the surface temperature profile captured during the 09-23-22 #1 test.

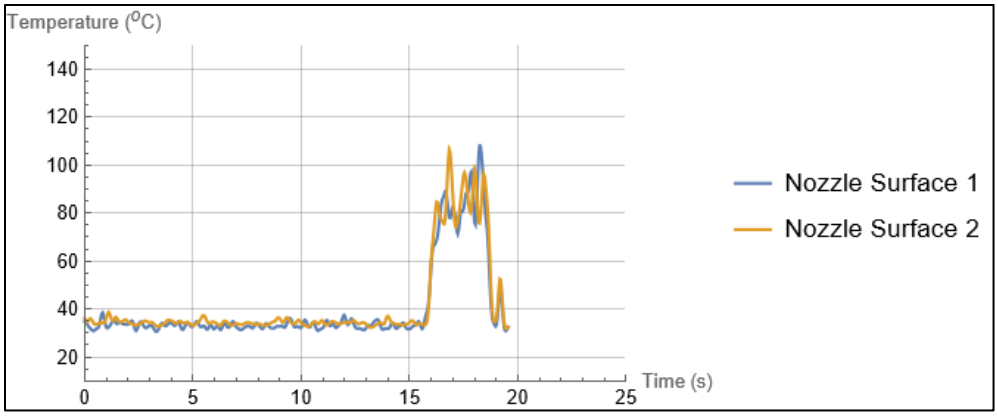

Figure 5.17. Nozzle Surface Temperature, 09-23-22 Test #1

Measurements taken with an off-the-shelf thermocouple reader after some tests showed the nozzle surface temperature was closer to ~250 °C. During the last test, the graphite nozzle reached a temperature of ~450 °C according to the off-the-shelf thermocouple reader taped to the test stand. This was hot enough for the nozzle to catch fire after the rocket had been extinguished. The fire had to be extinguished with a dry-chemical fire extinguisher. Figure 5.18 shows the nozzle burning and 5.19 shows the aftermath. According to the manufacturer data found in Appendix A13, graphite's max temperature in an oxidizing atmosphere is 427 °C. The reason the graphite combusted after this test and none of the others is because the 10-27-22 test was the longest continuous hot-fire that had been conducted with an oxygen mass flow rate of 0.020 kg/s. Because of the higher mass flow rate through the rocket, the average convection coefficient of the combustion products would have increased, and more heat would have been transferred to the nozzle. The solution to this problem is to limit hot-fires to no more 15 seconds when using an oxygen mass flow rate of 0.020 kg/s.

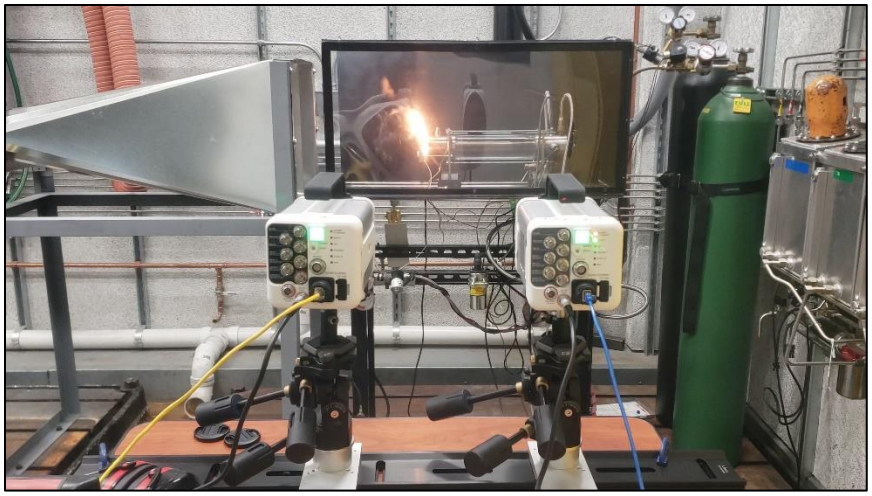

Figure 5.18. Nozzle Burning After Conclusion of Hot-Fire, 10-27-22 Test

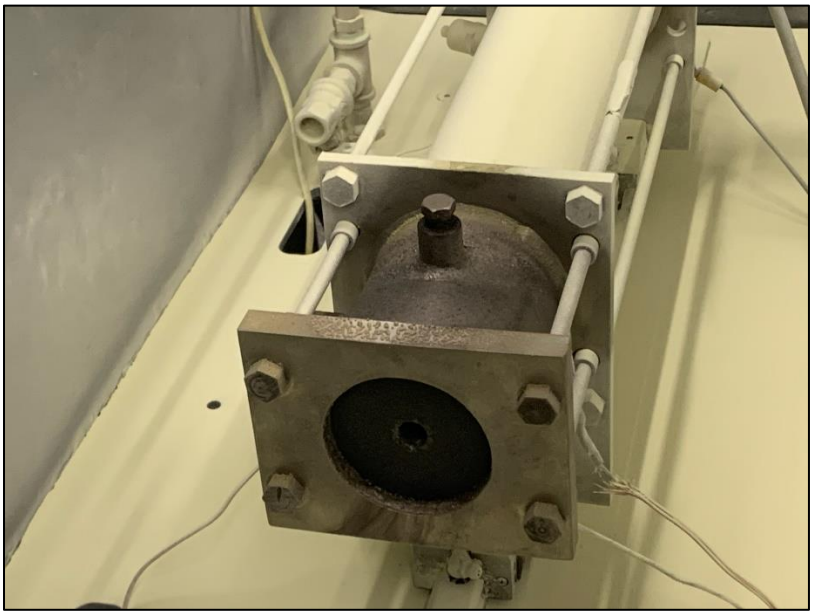

Figure 5.19. Aftermath of Fire

5.6. Performance Calculations

From these experiments, we have the average fuel mass flow rate, the oxygen mass flow rate, and the measured thrust. From these three quantities, we can calculate the exhaust velocity and the specific impulse according to Equation 2.12. To calculate the exhaust velocity, we assume that exit pressure of the nozzle is close to the ambient pressure, so that the pressure term of Equation 2.12 is negligible. Table 5.3 shows the results of these exhaust velocity calculations, along with the specific impulse and the average O/F ratio.

Table 5.3. Exhaust Velocity Calculations

Test	**Total MFR**	$\bar{v}_e$	$\bar{I}_{sp}$	**Average (O/F)**
08-25-22 1 & 2	0.014254 kg/s	653.036 m/s	66.5684 s	6.02694
09-23-22 1 & 2	0.014962	630.309 m/s	64.2517 s	6.31733
10-11-22 & 10-13-22	0.02894 kg/s	866.342 m/s	88.3121 s	7.58054
10-27-22	0.027824 kg/s	1222.75 m/s	130.228 s	7.6935

These results are not great and are the reason why the thrust measurements are thought to be off. Although the flow must be over-expanded due to the clear presence of shock diamonds in the exhaust, it does not look as if flow separation is occurring inside the nozzle. Interestingly, the last test generated an exhaust velocity and specific impulse that are more acceptable, but still way less than what was expected from both the original design team's calculations and the CEA calculations. According to Figure 3.7, we should be getting a specific impulse closer to 200 s. To give some perspective on how low the calculated the specific impulses are, one could expect a specific impulse of 66 s from a cold gas thruster working at room temperature using nitrogen. Table 3.4 shows the c* and coefficient of thrust calculations for the 3 tests where post-combustion pressures were measured.

Table 5.4. Characteristic Velocity and Coefficient of Thrust Calculations

Test	**c***	**C_F**	η_{comb}
09-23-22 #1 and 09-23-22 #2	1518.3 m/s	0.415	~96%
10-11-22	1347.46 m/s	0.734	~85%

The c* values were calculated by taking the average post-combustion pressure from Table 5.1, adding 101325 Pa to convert it to absolute pressure, multiplying it by the design area of the nozzle throat, then dividing the result by the total mass flow rate. The combustion efficiency was calculated by dividing the measured c* value by the theoretical CEA c* value, which was retrieved by looking at the c* plot for the O/F ratio the rocket operated at. A combustion efficiency of 96% is very good. Meanwhile, the coefficient of thrust calculations do not look so good, and are abnormally low. This supports the view that the thrust is being measured incorrectly. If the thrust were being measured correctly, then we would expect the coefficient of thrust to be at least 1.0 or more. The c* and C_F coefficients for the 10-11-22 test should be considered less accurate, since two tests were conducted using the same fuel grain, and the fuel grain wasn't weighed between tests. Therefore, to calculate the c* and C_F values for the 10-11-22 test, the average fuel mass flow rate that was calculated for both tests was used.

5.7. Regression Rate Calculations

To empirically determine the regression coefficients *a* and *n*, footage of the fuel grain was analyzed using ImageJ. First, bitmap images were extracted from the test footage using the command-line tool FFMPEG at intervals of 0.5 seconds for footage captured by the smartphone, and 0.3 seconds for footage captured by the high-speed cameras. Each image was then imported into the ImageJ and the apparent diameter of the fuel port was measured using the line tool. The scale was generally set by measuring either the diameter of the entire fuel grain, which is known to be 3 inches, or measuring the distance on a ruler which was placed in-view. Once the measurements were saved, they were imported into Wolfram Mathematica and a correction factor was applied to each data set based on the ratio of the apparent fuel port diameter and the true fuel port diameter. For all fuel grains that were burned, there were 2 distinct regions that developed inside the fuel port. The fuel port near the exit grew at a faster rate than the fuel port near the entrance did. This can clearly be seen in Figure 5.8. So, the rate of regression was not spatially uniform along the fuel grain axis. It was decided to take two sets of measurements of each image set, one near the entrance, and one near the exit, and determine regression coefficients from both. Equation 2.23 was the equation used to perform the fits. The Mathematica function FindFit was used to determine the coefficients, with *a* being in the range of 0 to 1, and *n* being in the range of 0 to 1. Table 5.5 shows the calculated coefficients *a* and *n* for each data set, as well as the mean for each. Additionally, Figures 5.20-5.22 show the regression data plots along with their fitted functions.

Table 5.5. Regression Coefficients

Test	*a*	*n*
08-25-22 D_1	4.07877E-5	0.380172
08-25-22 D_2	1.3261E-5	0.7724
09-23-22 D_1	6.07212E-6	0.772844
09-23-22 D_2	8.91039E-6	0.821787
10-11-22 D_1	1.33644E-5	0.616098
10-11-22 D_2	1.34607E-5	0.72647
Mean	1.609272E-5	0.681629

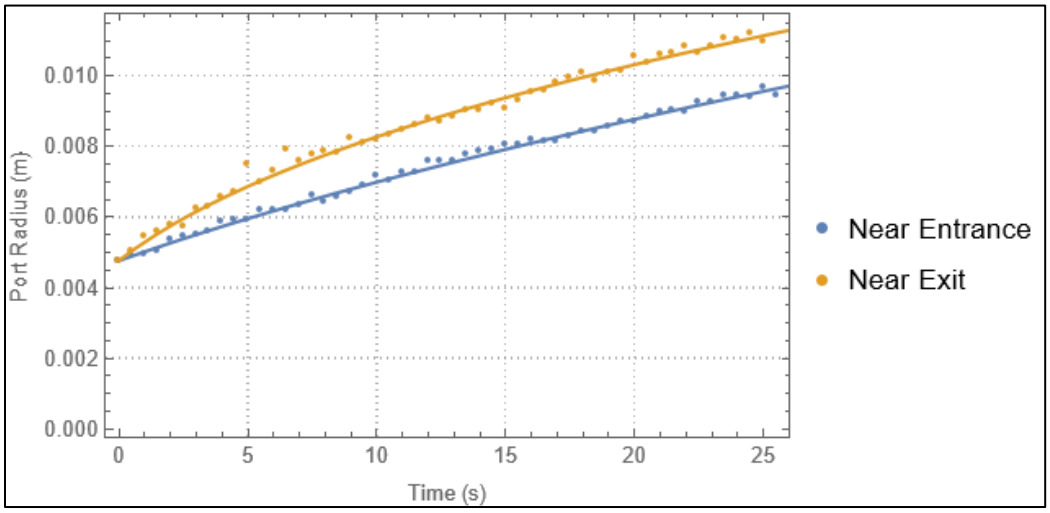

Figure 5.20. Regression Plot with Fitted Functions, 08-25-22 Tests

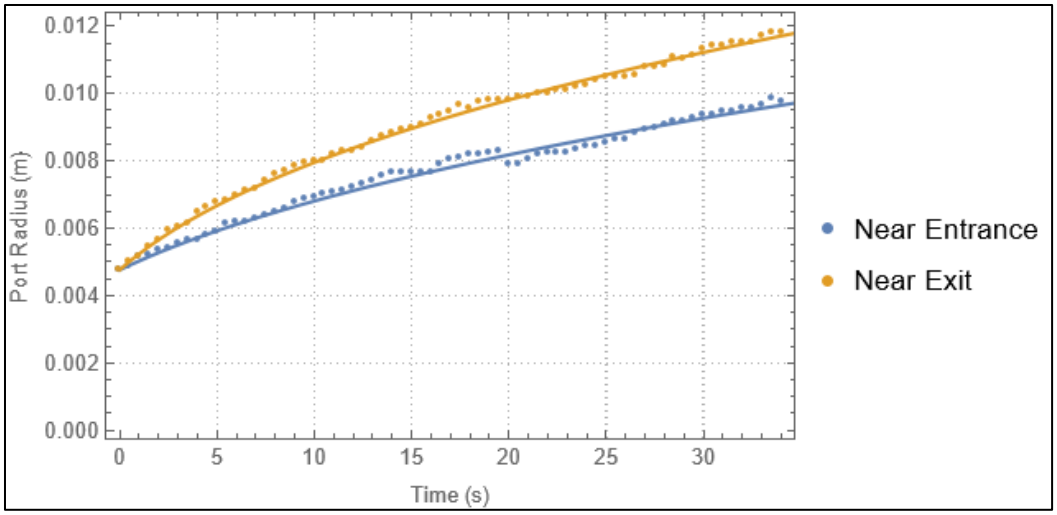

Figure 5.21. Regression Plot with Fitted Functions, 09-23-22 Tests

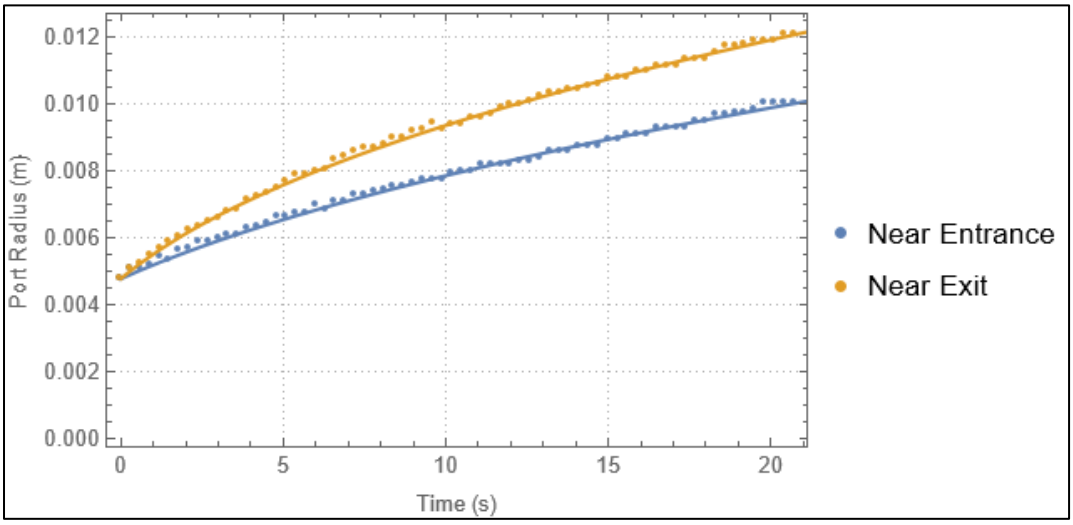

Figure 5.22. Regression Plots with Fitted Functions, 10-11-22 Tests

The calculated regression coefficients were higher than reported in the literature. This could be for a couple of reasons. If one looks at the enclosure window in Figures 5.1 through 5.4, the reflections of the high-speed cameras become extremely distorted due to the heat given off by the rocket exhaust. This could mean that the image of the fuel grain as viewed through the enclosure might be becoming distorted. Additionally, the PMMA cylinder distorts images that are viewed through it. One more factor to consider is that the index of refraction changes as the

fuel grain heats up. Mechentel et al. reported this in their paper where they report on their calculation of regression coefficients for PMMA, although in their case, they used a square fuel grain with a circular fuel port (Mechentel et al, 2019).

5.8. Nozzle Erosion

As mentioned earlier, 3 nozzle types were used with the NDSU hybrid rocket and they were stainless steel, coarse graphite, and ultrafine graphite. For each test, the nozzle's throat diameter was measured under a visual microscope. After each test, the nozzle's throat diameter was measured again, to determine the extent of nozzle erosion taking place. Table 5.6 summarizes these measurements.

Table 5.6. Summary of Nozzle Erosion Measurements

Test	Nozzle Material	Initial Diameter	Final Diameter
05-04-22 & 05-16-22	Coarse Graphite	0.3060 in	0.3475 in
08-25-22 1 & 2	Stainless Steel	0.3045 in	0.2880 in
10-11-22 & 10-13-22	Ultrafine Graphite	0.3031 in	0.3092 in
10-27-22	Ultrafine Graphite	0.2995 in	0.3228 in

Figure 5.23 shows what the throat of a coarse graphite nozzle looks like before a test, and Figure 5.24 shows the same nozzle after a test fire. Meanwhile, Figure 5.25 shows what an ultrafine graphite nozzle throat looks like after a test. It's clear that ultrafine graphite is a better choice for rocket nozzles, because while both undergo throat erosion, ultrafine graphite retains its smoothness while coarse graphite does not. For tests that last less than 20 seconds and use an oxygen mass flow rate of 0.010 kg/s, stainless steel will work fine, and can even be reused for multiple tests. However, using stainless steel at an oxygen mass flow rate of 0.020 kg/s is not advised, as the nozzle will start melting in seconds. At first, this was thought to be due to higher

combustion temperatures, but running at 0.020 kg/s should actually decrease the combustion temperature a little bit, since running at 0.010 kg/s should equate to a molar O/F ratio of around 6. So, stainless steel melts quickly at 0.020 kg/s because of the increased convection coefficient. Figure 5.26 shows the result of using a stainless steel nozzle at an oxygen mass flow rate of 0.020 kg/s.

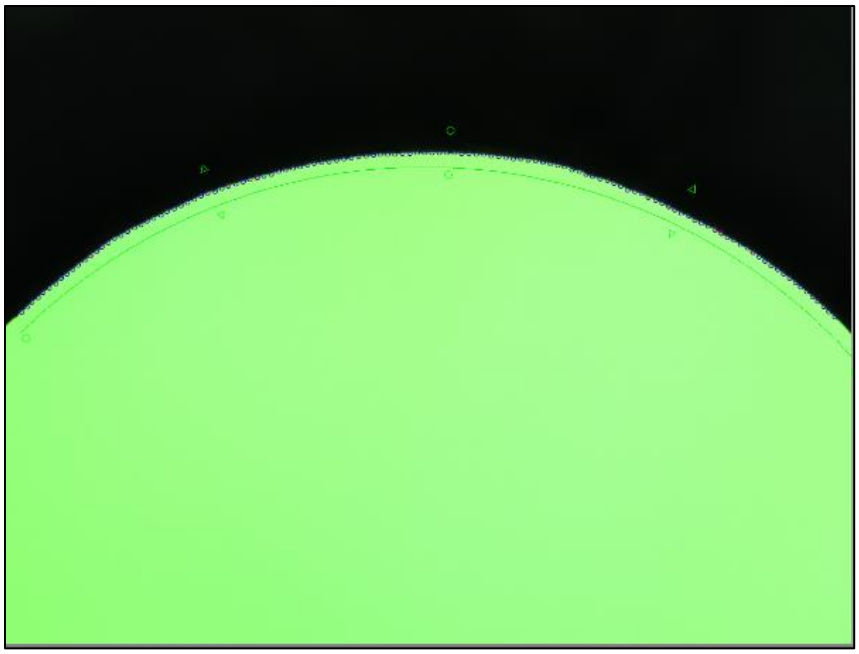

Figure 5.23. Coarse Graphite Nozzle Before Test

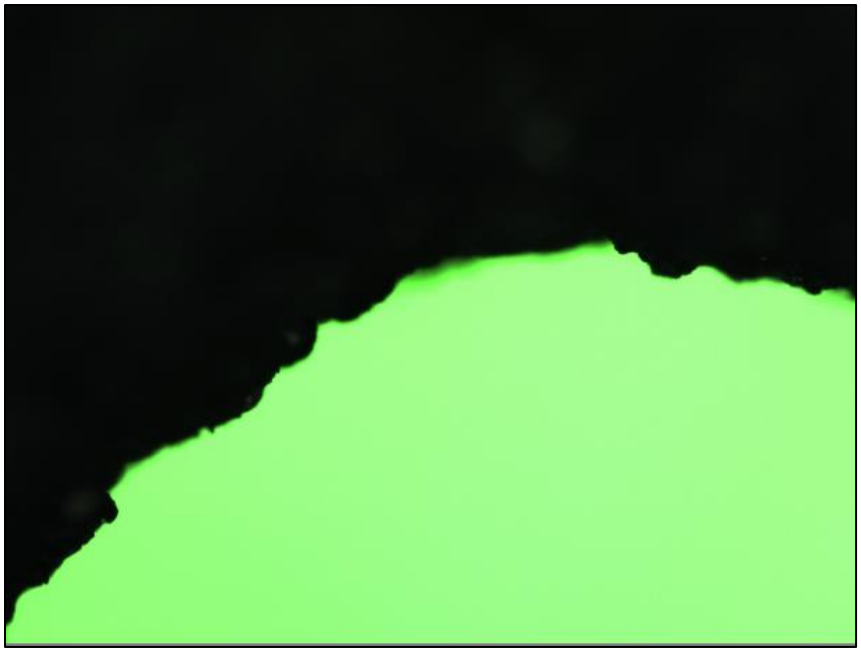

Figure 5.24. Coarse Graphite Nozzle Throat After Test

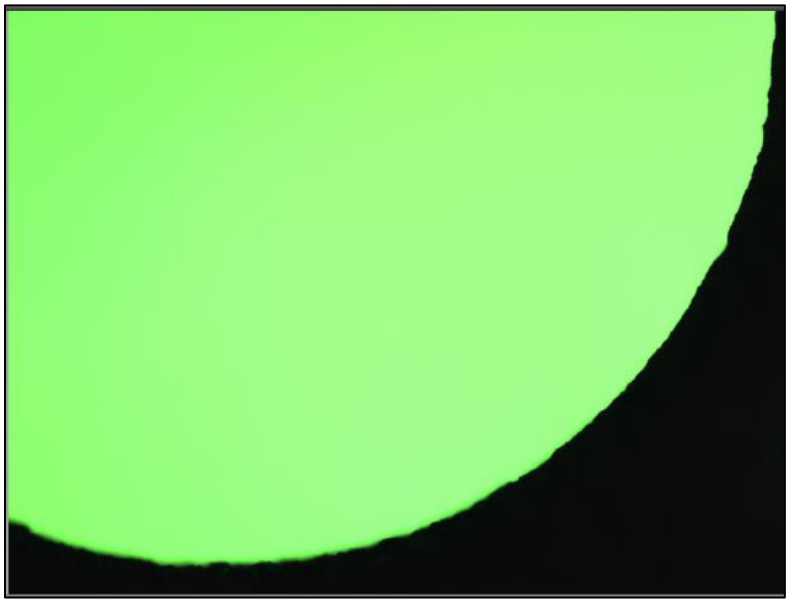

Figure 5.25. Ultrafine Graphite Nozzle Throat After Test

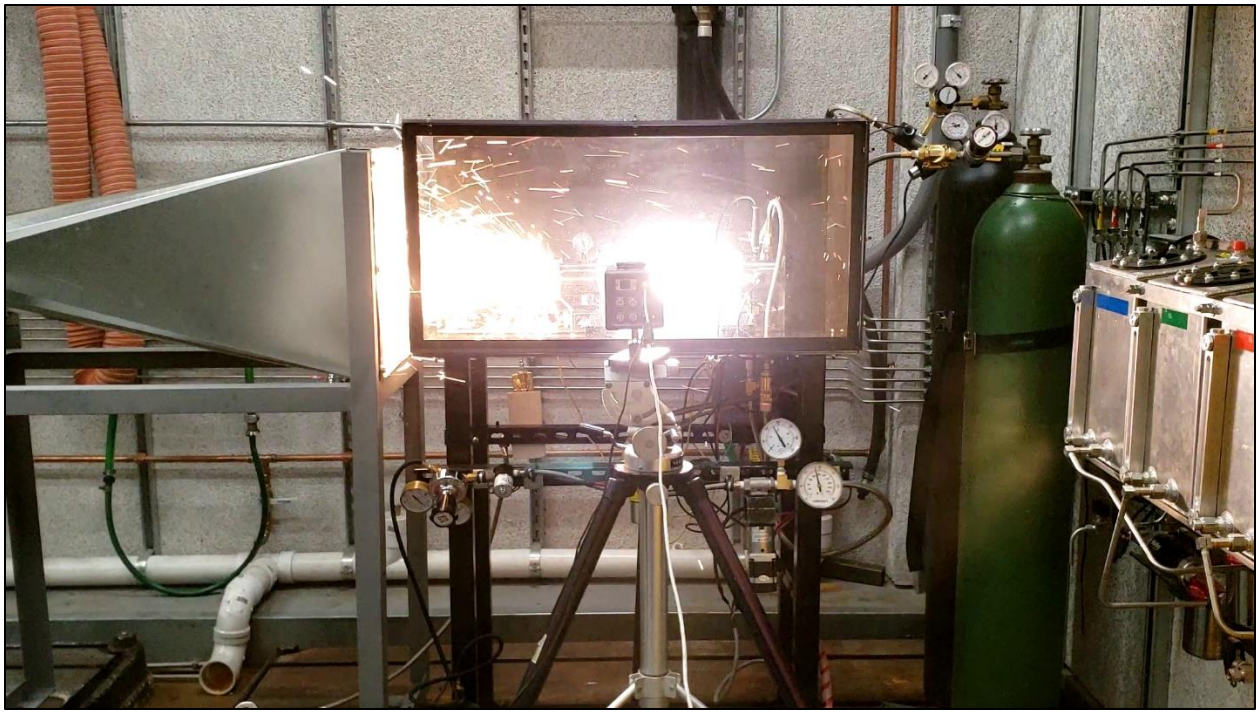

Figure 5.26. Stainless Steel Nozzle with High Oxygen Mass Flow Rate

6. CONCLUSIONS AND FURTHER WORK

This thesis sought to characterize the performance of the NDSU hybrid rocket. The following findings were made; c* calculations show that we are getting a reasonable combustion efficiency, and that we are probably getting the expected exhaust velocity out of the hybrid rocket. However, because the thrust is probably being underestimated by the load cell, the calculated exhaust velocity and specific impulse are much lower than expected. Therefore, the load cell instrumentation needs to be investigated further, to determine if the rocket really is producing a lower-than-expected thrust, or if the load cell just isn't measuring the thrust correctly, either due to a calibration error, or because the rocket isn't making good contact with the load connection. Calculating the regression coefficients can in principle be done by taking pictures of the fuel grain as it burns, but there are several factors that need to be considered, such as the image distortion caused the fuel grain itself, and the image distortion caused by the enclosure. As for future work, a great way to measure the fuel mass flow rate over time would be to place the test stand on 4 load cells and measure how lighter it gets over the course of the test. As for the exhaust, taking high-speed footage as the rocket starts and runs would be great. Overall, the hybrid rocket testing program at NDSU was successful at estimating the c* and combustion efficiency of the rocket and showing that hybrids can be run safely and successfully numerous times, but more work is needed to accurately characterize the exhaust velocity and the specific impulse.

REFERENCES

"A brief history of hybrid rocket technology" Space Propulsion Group, Inc. Available: https://web.archive.org/web/20110716115139/http://www.spg-corp.com/News_12.php

Anderson, J.D., "Fundamentals of Aerodynamics", 6th edition, 2017.

Benson, T., "Rocket Thrust Summary*", NASA Glenn Research Center Online Publication*, 2021. Available: https://www.grc.nasa.gov/www/k-12/rocket/rktthsum.html

Campbell, J., Macklin, F., and Thicksten, Z., "Handling Considerations of Nitrous Oxide in Hybrid Rocket Motor Testing," *44th AIAA/ASME/SAE/ASEE Joint Propulsion Conference & Exhibit,* 2008.

Clark, J.D., "Ignition!: An Informal History Of Liquid Rocket Propellants" 2nd ed., Rutgers University Press Classics, 2018 (1st edition published 1972)

Dhandapani, C., Rabinovitch, J., & Blanquart, G., "Combustion Studies of MMA/GOx for a Hybrid Rocket Motor", *AIAA AVIATION 2020 FORUM,* 2020

Dixon, P.W., "Estimation of Hybrid Rocket Chamber Temperature Via Nozzle Wall Temperature Measurements" Thermal & Fluids Analysis Workshop, August 24th-26th, 2021

Dixon, P.W., Fabijanic, C., Refling, W., Yurek, J., and Estevadeordal, J., "Advanced Characterization of a Lab-Scale PMMA/GOx Hybrid Rocket" *AIAA Scitech*, 2023

Dyer, J., "Conceptual schematic of a hybrid rocket propulsion system", April 2009. Available: https://commons.wikimedia.org/wiki/File:Hybrids_big.png

Estevadeordal, J., Miller, H., Yurek, J., Omerza, E., Ullah, A. H., Fabijanic, C., Arstein, D., and Lueders, G., "Design and Characterization of Optically Clear PMMA/ Gox Hybrid

Rocket Propulsion System.," *AIAA SciTech Forum*, 2021. Available: https://arc.aiaa.org/doi/abs/10.2514/6.2021-1020.

Gordon, S and McBride B.J "Computer Program for Calculation of Complex Chemical Equilibrium Compositions and Applications. Part 1: Analysis", October 1st 1994. Available: https://ntrs.nasa.gov/api/citations/19950013764/downloads/19950013764.pdf

Graphitestore.com, "Product Data Sheet". Available: https://www.graphitestore.com/core/media/media.nl?id=6310&c=4343521&h=Tz5uoWvr-nhJ13GL1b1lG8HrmYUqV1M_1bOTFQ2MMuiQapxt

Handbook of Chemical Hazard Analysis Procedures, Appendix B, Federal Emergency Management Agency, U.S. Dept. of Transportation, and U.S. Environmental Protection Agency, 1989.

Jens, E.T, "Hybrid Rocket Combustion and Applications to Space Exploration Missions" Dissertation, Stanford University, 2015

Mechentel, F.S., Hord, B.R., Cantwell, B.J. "Optically Resolved Fuel Regression of a Clear PMMA Hybrid Rocket Motor" *AIAA Propulsion and Energy Forum*, 2019.

Narsai, P., "Nozzle Erosion in Hybrid Rocket Motors" Dissertation. Stanford University, 2016. Available: https://web.stanford.edu/~cantwell/AA284A_Course_Material/AA284A_Resources/Narsai,%20P.,%20Nozzle%20Erosion%20in%20Hybrid%20Rocket%20Motors%20PhD%20thesis%20Stanford%202015.pdf

Palateerdham, S. K., "Experimental Investigation of the Paraffin Thermomechanical Properties and Hybrid Rocket Engine Performance for Different Fuel Grain Formulations," Thesis, 2020. Available:

https://www.researchgate.net/publication/344085977_Experimental_Investigation_of_the_Paraffin_Thermomechanical_Properties_and_Hybrid_Rocket_Engine_Performance_for_Different_Fuel_Grain_Formulations/link/5fd885d792851c13fe895017/download

Rabinovitch, J., Jens, E.T., Karp, A.C., Nakazono, B., Conte, A., Vaughan, D.A., and Inoue, H., "Characterization of Polymethylmethacrylate as a Fuel for Hybrid Rocket Motors", *AIAA Propulsion and Energy Forum*, 2018

Shariatzadeh, O.J., Abrishamkar, A., and Jafari, A.J., "Computational Modeling of a Typical Supersonic Converging-Diverging Nozzle and Validation by Real Measured Data" *Journal of Clean Energy Technologies*, January 2015. Available: https://www.researchgate.net/publication/271293536_Computational_Modeling_of_a_Typical_Supersonic_Converging-Diverging_Nozzle_and_Validation_by_Real_Measured_Data

Sharp, T., "SpaceShipOne: The first private spacecraft," *Space.com* Available: https://www.space.com/16769-spaceshipone-first-private-spacecraft.html.

Story, G., and Arves, J., "Chapter 14: Flight Testing of Hybrid Powered Vehicles", Feb. 2006. Available: https://ntrs.nasa.gov/api/citations/20060048274/downloads/20060048274.pdf

Sutton, G. P., and Biblarz, O., "Rocket Propulsion Elements", 8th ed., Hoboken, New Jersey: John Wiley & Sons, Inc., 2010.

Tarifa, C.M. and Pizzuti, L., "Theoretical Performance Analysis of Hybrid Rocket Propellants Aiming at the Design of a Test Bench and a Propulsive System" *8th European Conference for Aeronautics and Space Sciences (EUCASS)*, 2019.

te.com "FX19 Datasheet" Available: https://www.te.com/commerce/DocumentDelivery/DDEController?Action=showdoc&Do

cId=Data+Sheet%7FFX19%7FA13%7Fpdf%7FEnglish%7FENG_DS_FX19_A13.pdf%7FFX1901-0001-0025-L

Werling, L., Hörger, T., Ciezki, H., and Schlechtriem, S. "Experimental and Theoretical Analysis of the Combustion Efficiency and the Heat Loads on a N_2O/C_2H_4 Green Propellant Combustion Chamber" *8th European Conference for Aeronautics and Aerospace Sciences (EUCASS),* 2019. Available: https://elib.dlr.de/128360/1/EUCASS2019-0142%20Werling.pdf

Zilliac, G. and Karabeyoglu, M.A, "Hybrid Rocket Fuel Regression Rata Data and Modeling" *42nd AIAA/ASME/SAE/ASEE Joint Propulsion Conference & Exhibit,* 2006. Available: https://web.stanford.edu/~cantwell/AA284A_Course_Material/AA284A_Resources/Zilliac%20and%20Karabeyoglu%20AIAA%202006-4504%20Hybrid_Rocket_Fuel_Regression_Rate_Data_and_Modeling.pdf

APPENDIX. CODE AND ADDITONAL DATA

```
int potValue = 0;
int previous = 0;
float alpha = 0.1;
int motorstate = 0; //1 is standby, 2 is start, 3 is full
int counter = 0;
int t = 0;




#define ANALOG_IN A0   //potentiometer signal
#define limit_switch 9 //limit switch on digital pin 9
#define pul 2          //PUL+ input on encoder
#define dir 3          //DIR+ input on encoder
#define pin4 A4
#define pin5 A5


void PulseCW(int halfwidth)
{
  digitalWrite(dir, false);
  digitalWrite(pul, true);
  delayMicroseconds(halfwidth);
  digitalWrite(pul, false);
  delayMicroseconds(halfwidth);

}

void PulseCCW(int halfwidth)
{
  digitalWrite(dir, true);
  digitalWrite(pul, true);
  delayMicroseconds(halfwidth);
  digitalWrite(pul, false);
  delayMicroseconds(halfwidth);
}

void setup()
{
  Serial.begin(9600);     //Start the serial monitor with speed of 9600 bauds
  pinMode(pul, OUTPUT);   //PUL+ input on encoder
  pinMode(dir, OUTPUT);   //DIR+ input on encoder
  pinMode(limit_switch, INPUT_PULLUP);
  digitalWrite(dir, true);


  Serial.println("Stepper is homing.....................");

  while(!digitalRead(limit_switch))
  {

  digitalWrite(pul, true);
  delayMicroseconds(1000);
  digitalWrite(pul, false);
  delayMicroseconds(1000);
  }

Serial.println("Homing Completed.....................");

previous = potValue;



while(analogRead(A0) != 0) //ensure that the potentiometer is set to zero before moving to the control loop
{

  Serial.println("Potentiometer is not set to zero!");
  delay(1000);

}

}
```

Figure A1. Stepper Motor Arduino Code, Part 1

```
void loop()
{

//Serial.println(potValue);

potValue = analogRead(A0);

if(potValue == 500 && potValue>previous) //advance from standby to start
{
  while(counter<=550) // 12,260 pulses equals 1 full rotation.
  {
    PulseCW(100);
    counter++;
  }
  counter = 0;
  previous = potValue;
}

else if(potValue == 1000 && potValue>previous) //advance from start to full
{
  while(counter<=2510)
  {
    PulseCW(500);
    counter++;
  }
  counter = 0;
  previous = potValue;
  motorstate = 3;
}

else if(potValue == 0 && potValue<previous && motorstate != 3) //advance from start to standby
{
while(counter<=550)
  {
    PulseCCW(100);
    counter++;
  }
  counter = 0;
  previous = potValue;
}

else if(potValue == 0 && potValue<previous && motorstate == 3) //advance from full to standby
{
  while(counter<=3060)
  {
    PulseCCW(100);
    counter++;
  }
  counter = 0;
  previous = potValue;
  motorstate = 1;
}


}
```

Figure A2. Stepper Motor Arduino Code, Part 2

```
ClearAll["Global`*"];

Manipulate[

 A2 := π/4 * (d * 0.0254)^2;
 ρ1 := (P1 * 6895)/(R * T1);

 PR := P2/P1;
 MFRunchoked := c * A2 * √(2 * ρ1 * (P1 * 6895) * (γ/(γ - 1)) ((PR)^(2/γ) - (PR)^((γ+1)/γ)));

 MFRchoked := c * A2 * √(γ * (P1 * 6895) * ρ1 * (2/(γ + 1))^((γ+1)/(γ-1)));

 MFRchokedError := 6895 A2 Sqrt[(2^((1 + γ)/(-1 + γ)) P1^2 γ (1/(1 + γ))^((1 + γ)/(-1 + γ)))/(R T1)] δc +
   (6895 × 2^((1 + γ)/(-1 + γ)) A2 c P1 γ (1/(1 + γ))^((1 + γ)/(-1 + γ)) δP)/
    (R T1 Sqrt[(2^((1 + γ)/(-1 + γ)) P1^2 γ (1/(1 + γ))^((1 + γ)/(-1 + γ)))/(R T1)]);

 MFRunchokedError := 6895 Sqrt[2] A2 Sqrt[(P1^2 ((P2/P1)^(2/γ) - (P2/P1)^((1 + γ)/γ)) γ)/(R T1 (-1 + γ))] δc +
   (6895 A2 c P1^2 γ ((2 (P2/P1)^(-1 + 2/γ))/(P1 γ) - ((P2/P1)^(-1 + (1 + γ)/γ) (1 + γ))/(P1 γ)) δP)/
    (Sqrt[2] R T1 (-1 + γ) Sqrt[(P1^2 ((P2/P1)^(2/γ) - (P2/P1)^((1 + γ)/γ)) γ)/(R T1 (-1 + γ))]) +
   (6895 A2 c ((2 P1 ((P2/P1)^(2/γ) - (P2/P1)^((1 + γ)/γ)) γ)/(R T1 (-1 + γ))) +
        (P1^2 γ (-((2 P2 (P2/P1)^(-1 + 2/γ))/(P1^2 γ)) + (P2 (P2/P1)^(-1 + (1 + γ)/γ) (1 + γ))/(P1^2 γ)))/(R T1 (-1 + γ))) δP)/
    (Sqrt[2] Sqrt[(P1^2 ((P2/P1)^(2/γ) - (P2/P1)^((1 + γ)/γ)) γ)/(R T1 (-1 + γ))]);
```

Figure A3. Oxygen Mass Flow Rate Calculation Program, Part 1

```
Column[{
  Text@Row[{"Mass flow rate, unchoked = ", MFRunchoked, " kg/s"}],
  Text@Row[{"Mass flow rate, choked = ", MFRchoked, " kg/s"}],
  Text@Row[{"Pressure Ratio = ", N[PR]}],
  Text@Row[{"Choked Flow = ", PR ≤ 0.529 }],
  Text@Row[{"Unchoked Flow Error = ", MFRunchokedError, "kg/s"}],
  Text@Row[{"Choked Flow Error = ", MFRchokedError, "kg/s"}]}]


], {{d, 0.096}, 0.001, 1}, {{P1, 300}, 1, 10000000}, {{P2, 150}, 1, 10000000}, {{T1, 298}, 1, 1000}, {{γ, 1.397}, 1.001, 2},
{{R, 259.8}, 1, 10000}, {{c, 0.935622}, 0.01, 1}, {{δP, 2.5}, 0, 10}, {{δc, 0.07}, 0, 0.5}, ControlType → InputField]
```

d	0.0955
P1	127.135
P2	73.52
T1	298
γ	1.397
R	259.8
c	0.935622
δP	2.5
δc	0.05

Mass flow rate, unchoked = 0.0092699 kg/s
Mass flow rate, choked = 0.0093204 kg/s
Pressure Ratio = 0.578283
Choked Flow = False
Unchoked Flow Error = 0.00066067kg/s
Choked Flow Error = 0.000681364kg/s

Figure A4. Oxygen Mass Flow Rate Calculation Program, Part 2

```
tcConvert[list_] :=
  Table[
   Piecewise[
    {{0 + 2.508355 * 10^01 * list[[i]] + 7.860106 * 10^-02 * list[[i]]^2 - 2.503131 * 10^-01 * list[[i]]^3 + 8.315270 * 10^-02 * list[[i]]^4 - 1.228034 * 10^-02 * list[[i]]^5 +
       9.804036 * 10^-04 * list[[i]]^6 - 4.413030 * 10^-05 * list[[i]]^7 + 1.057734 * 10^-06 * list[[i]]^8 - 1.052755 * 10^-08 * list[[i]]^9, 0 ≤ list[[i]] < 20.644},
     {-1.318058 * 10^2 + 4.830222 * 10^1 * list[[i]] - 1.646031 * 10^0 * list[[i]]^2 + 5.464731 * 10^-2 * list[[i]]^3 - 9.650715 * 10^-04 * list[[i]]^4 +
       8.802193 * 10^-06 * list[[i]]^5 - 3.110810 * 10^-08 * list[[i]]^6, list[[i]] ≥ 20.664}}], {i, 1, Length[list]}];

voltages = Table[x, {x, 0, 55, 0.01}];
LookupTable = Inner[List, voltages, tcConvert[voltages], List];

= Export["C:\\Users\Porter\OneDrive - North Dakota University System\\Hybrid Rocket Research\\ITS-90 Type K Lookup Table.csv", LookupTable];
```

Figure A5. Type-K Thermocouple Lookup Table Creation Using NIST ITS-90 Coefficients

$$\rho 1 = \frac{P1 * 6895}{R * T1};$$

$$mdotchoked = c * A2 * \sqrt{\gamma * (P1 * 6895) * \rho 1 * \left(\frac{2}{\gamma + 1}\right)^{\frac{\gamma+1}{\gamma-1}}};$$

$$mdotunchoked = c * A2 * \sqrt{2 * \rho 1 * (P1 * 6895) * \left(\frac{\gamma}{\gamma - 1}\right) \left(\left(\frac{P2}{P1}\right)^{\frac{2}{\gamma}} - \left(\frac{P2}{P1}\right)^{\frac{\gamma+1}{\gamma}}\right)};$$

$$mdotchokedError = D[mdotchoked, P1] * \delta P + D[mdotchoked, c] * \delta c$$

$$6895\ A2 \sqrt{\frac{2^{\frac{1+\gamma}{-1+\gamma}}\ P1^2\ \gamma \left(\frac{1}{1+\gamma}\right)^{\frac{1+\gamma}{-1+\gamma}}}{R\ T1}}\ \delta c + \frac{6895 \times 2^{\frac{1+\gamma}{-1+\gamma}}\ A2\ c\ P1\ \gamma \left(\frac{1}{1+\gamma}\right)^{\frac{1+\gamma}{-1+\gamma}}\ \delta P}{R\ T1 \sqrt{\frac{2^{\frac{1+\gamma}{-1+\gamma}}\ P1^2\ \gamma \left(\frac{1}{1+\gamma}\right)^{\frac{1+\gamma}{-1+\gamma}}}{R\ T1}}}$$

$$mdotunchokedError = D[mdotunchoked, P1] * \delta P + D[mdotunchoked, P2] * \delta P + D[mdotunchoked, c] * \delta c$$

$$6895\ \sqrt{2}\ A2 \sqrt{\frac{P1^2 \left(\left(\frac{P2}{P1}\right)^{2/\gamma} - \left(\frac{P2}{P1}\right)^{\frac{1+\gamma}{\gamma}}\right) \gamma}{R\ T1\ (-1+\gamma)}}\ \delta c + \frac{6895\ A2\ c\ P1^2\ \gamma \left(\frac{2\left(\frac{P2}{P1}\right)^{-1+\frac{2}{\gamma}}}{P1\ \gamma} - \frac{\left(\frac{P2}{P1}\right)^{-1+\frac{1+\gamma}{\gamma}}\ (1+\gamma)}{P1\ \gamma}\right) \delta P}{\sqrt{2}\ R\ T1\ (-1+\gamma) \sqrt{\frac{P1^2 \left(\left(\frac{P2}{P1}\right)^{2/\gamma} - \left(\frac{P2}{P1}\right)^{\frac{1+\gamma}{\gamma}}\right) \gamma}{R\ T1\ (-1+\gamma)}}} + \frac{6895\ A2\ c \left(\frac{2\ P1 \left(\left(\frac{P2}{P1}\right)^{2/\gamma} - \left(\frac{P2}{P1}\right)^{\frac{1+\gamma}{\gamma}}\right) \gamma}{R\ T1\ (-1+\gamma)} + \frac{P1^2\ \gamma \left(-\frac{2\ P2 \left(\frac{P2}{P1}\right)^{-1+\frac{2}{\gamma}}}{P1^2\ \gamma} + \frac{P2 \left(\frac{P2}{P1}\right)^{-1+\frac{1+\gamma}{\gamma}}\ (1+\gamma)}{P1^2\ \gamma}\right)}{R\ T1\ (-1+\gamma)}\right) \delta P}{\sqrt{2} \sqrt{\frac{P1^2 \left(\left(\frac{P2}{P1}\right)^{2/\gamma} - \left(\frac{P2}{P1}\right)^{\frac{1+\gamma}{\gamma}}\right) \gamma}{R\ T1\ (-1+\gamma)}}}$$

Figure A6. Orifice Flow Error Analysis

In[795]:= AirFlow = {85.5, 103, 121, 138, 156, 191, 227, 264, 301, 338, 374, 413} * 1.667 * 10^-5; (*Sm^3/s*)
P1 = {69, 103.4, 137.9, 172.4, 206.9, 275.8, 344.8, 413.7, 482.7, 551.6, 620.6, 689.5} * 10^3 + 101 325 (*Pa absolute*)

Out[796]= {170 325, 204 725., 239 225., 273 725., 308 225., 377 125., 446 125., 515 025., 584 025., 652 925., 721 925., 790 825.}

In[797]:= orificedata = Inner[List, P1, AirFlow, List]

Out[797]= {{170 325, 0.00142529}, {204 725., 0.00171701}, {239 225., 0.00201707}, {273 725., 0.00230046}, {308 225., 0.00260052}, {377 125., 0.00318397}, {446 125., 0.00378409}, {515 025., 0.00440088}, {584 025., 0.00501767}, {652 925., 0.00563446}, {721 925., 0.00623458}, {790 825., 0.00688471}}

In[807]:= plot1 = ListPlot[orificedata, PlotRange → {{0, 700 000}, {0, 0.010}}, ImageSize → Medium, PlotTheme → "Detailed"]

Out[807]=

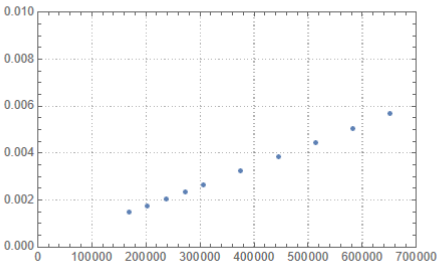

In[799]:= $\rho 1 = \frac{P1}{287.05 * 294.26}$ (*Density of upstream air flow, 70 F assumed*)

Out[799]= {2.01646, 2.42372, 2.83216, 3.2406, 3.64904, 4.46474, 5.28163, 6.09733, 6.91421, 7.72991, 8.5468, 9.3625}

In[800]:= $\rho 1s = \frac{101\,325}{287.05 * 294.26}$ (*Density at standard conditions of 101325 Pa and 70 F*)

Out[800]= 1.19958

Figure A7. Orifice Discharge Coefficient Calculation, Part 1

In[801]:= $\text{TheoreticalMFR} = \frac{\pi}{4} (0.00244)^2 * \sqrt{1.4 * P1 * \rho 1 * \left(\frac{2}{1.4+1}\right)^{\frac{1.4+1}{1.4-1}}}$

Out[801]= {0.00187639, 0.00225536, 0.00263543, 0.0030155, 0.00339557, 0.00415461, 0.00491476, 0.0056738, 0.00643394, 0.00719298, 0.00795312, 0.00871216}

In[802]:= MeasuredMFR = ρ1s * AirFlow

Out[802]= {0.00170974, 0.00205968, 0.00241963, 0.00275958, 0.00311952, 0.00381941, 0.0045393, 0.00527919, 0.00601908, 0.00675896, 0.00747885, 0.00825873}

In[804]:= MFR = Inner[List, TheoreticalMFR, MeasuredMFR, List]

Out[804]= {{0.00187639, 0.00170974}, {0.00225536, 0.00205968}, {0.00263543, 0.00241963}, {0.0030155, 0.00275958}, {0.00339557, 0.00311952}, {0.00415461, 0.00381941}, {0.00491476, 0.0045393}, {0.0056738, 0.00527919}, {0.00643394, 0.00601908}, {0.00719298, 0.00675896}, {0.00795312, 0.00747885}, {0.00871216, 0.00825873}}

In[805]:= NonlinearModelFit[MFR, m * x, {m}, x]

Out[805]= FittedModel[0.935622 x]

Figure A8. Orifice Discharge Coefficient Calculation, Part 2

PERFORMANCE SPECIFICATIONS

Supply Voltage: 5.0V, Ambient Temperature: 25°C (unless otherwise specified)

PARAMETERS	MIN	TYP	MAX	UNITS	NOTES
Recommended Excitation		5		V	
Full Scale Output Span	16	20	24	mV/V	
Full Scale Output Span (200lbf)	34.2	36	37.8	mV/V	
Zero Offset	-15		15	mV/V	
Non-Linearity	-1		1	%Span	
Hysteresis	-0.80		0.80	%Span	
Thermal Zero Shift	-0.05		0.05	%Span / °C	
Thermal Sensitivity Shift	-0.05		0.05	%Span / °C	
Insulation Resistance	50			MΩ	@500V_{DC}
Maximum Overload		250		%FS	
Maximum Overload (200lbf)		150		%FS	
Operating Temperature	0		50	°C	
Storage Temperature	-40		+85	°C	
Creeping			0.5	%Span	F.S. span in 3min
Zero Drift			0.5	%Span	Load F.S. 3min
Zero Return	-0.8		0.8	%Span	
Span Repeat	-0.8		0.8	%Span	
Humidity	0		90	%R.H.	
Deflection		0.05		mm	At Rated Load
Input Resistance	2.4	3	3.6	kΩ	
Output Resistance	1.76	2.2	2.64	kΩ	

Figure A9. Manufacturer-Provided Data Sheet for FX-1901 Compression Load Cell (*te.com)*

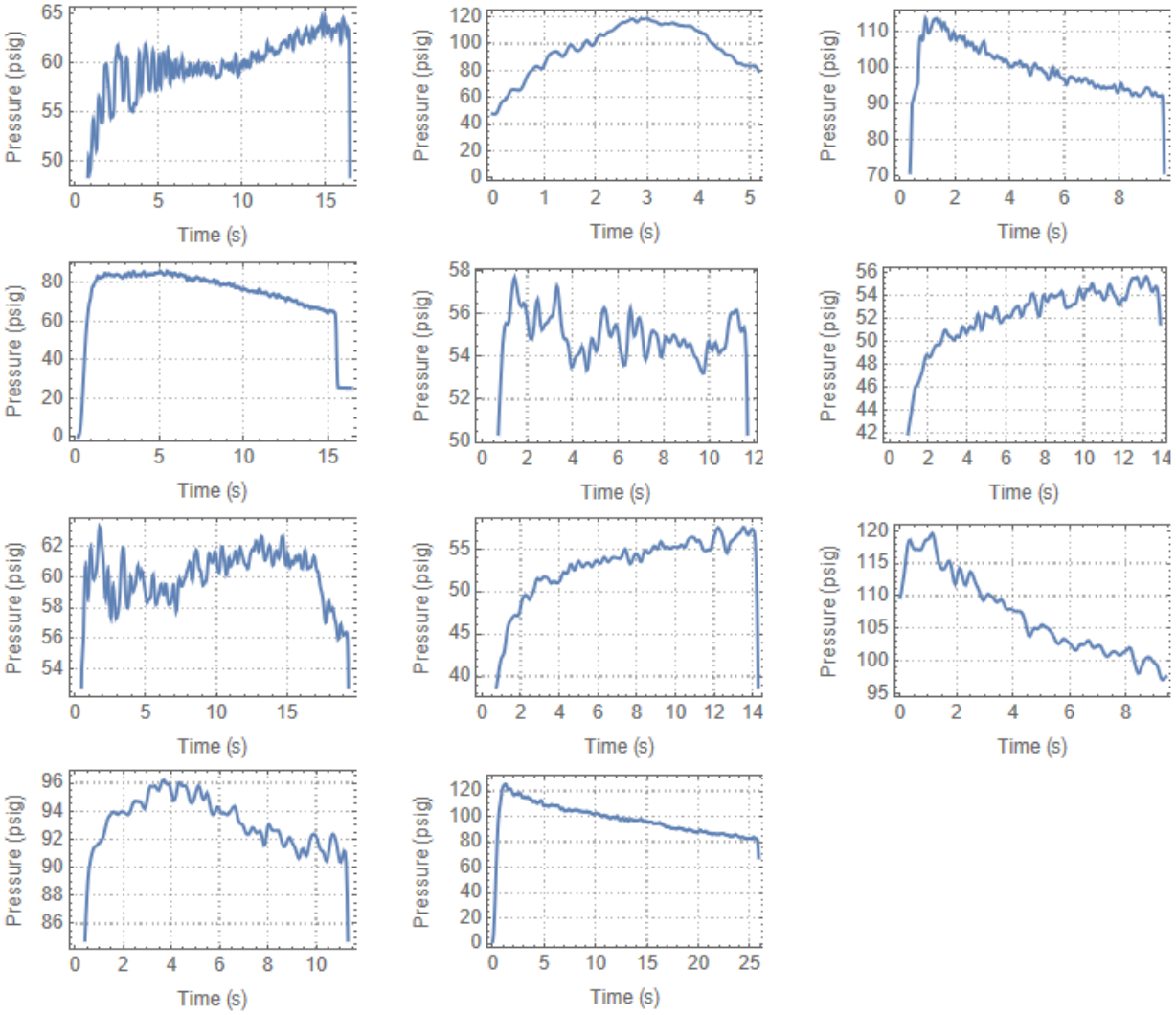

Figure A10. Pre-Combustion Pressure Plots for All Tests Starting From 11-29-22

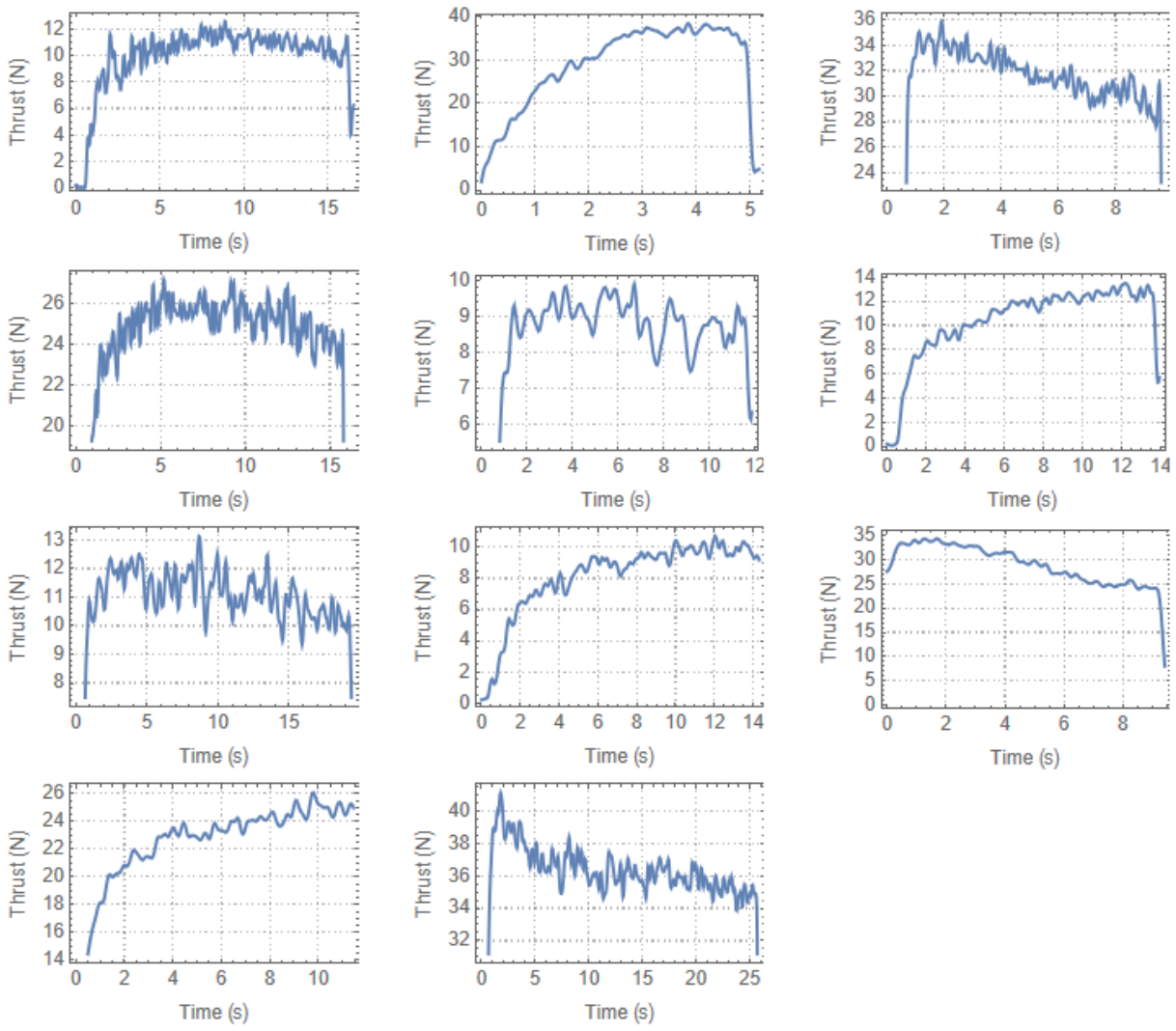

Figure A11. Thrust Plots for All Tests Starting with 11-29-21 Test

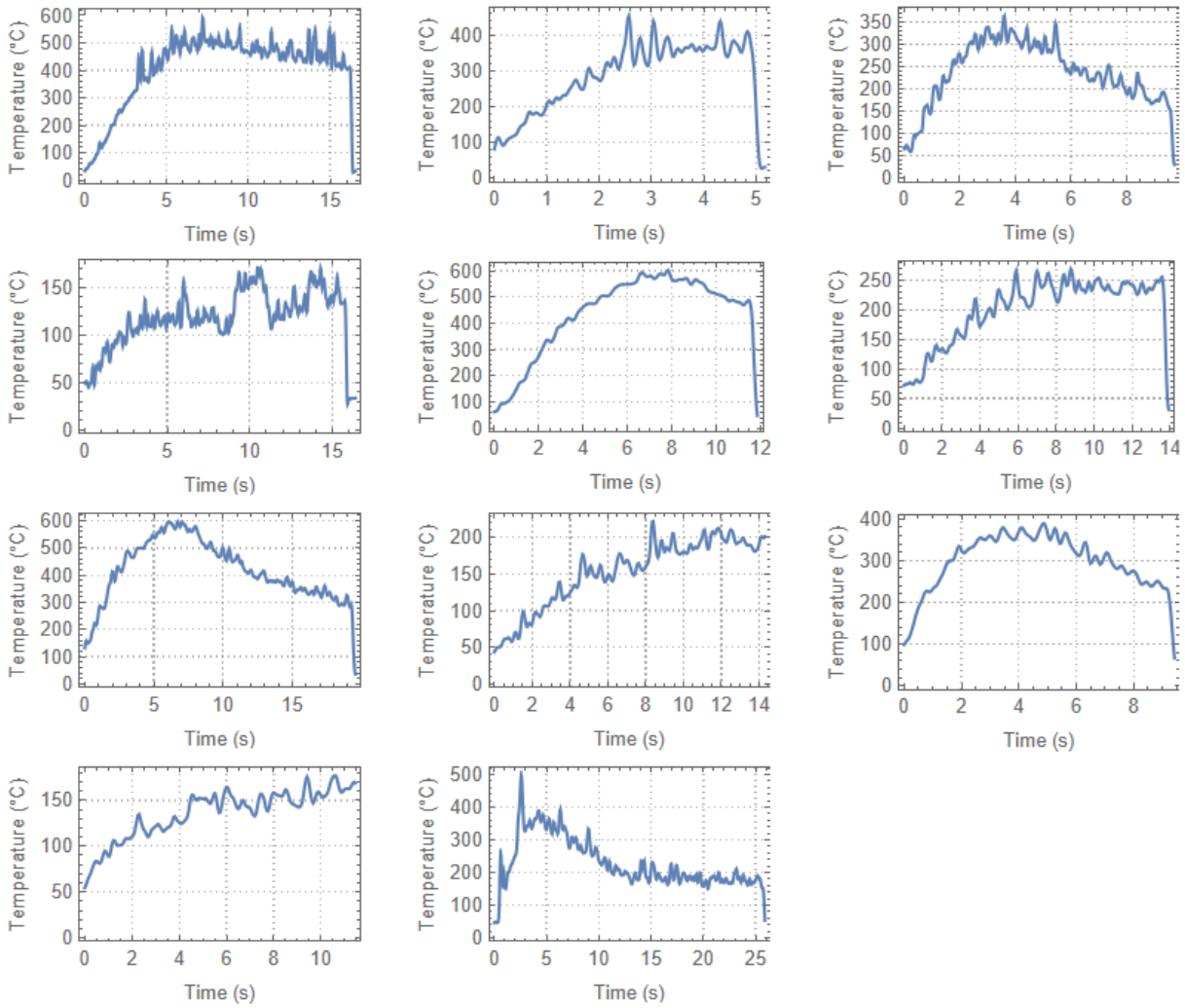

Figure A12. Pre-Combustion Temperature Plots for all Tests Starting With 11-29-21

Grade: GR001CC

Manufacturer: Graphtek LLC
Method of Manufacturing: Isostatically Pressed
Description: High Strength, wear resistant graphite

Property	US Value		Metric Value	
Density	**0.065**	lb/in^3	**1.81**	gr/cm^3
Shore Hardness	**60**			
Flexural Strength	**7250**	psi	**50**	MPa
Oxidizing Atmosphere	**801**	˚F	**427**	˚C
Neutral Atmosphere	**5000**	˚F	**2760**	˚C
Porosity	**12**	% VOL		% VOL
Electrical Resistivity	**0.00055**	Ω·in		Ω·m
Thermal Conductivity	**750**	$BTU/(h.ft^2$ ˚F/ft)	**85**	$W/(m^2.K/m)$
Ash Content	**100**	ppm		
CTE	**2.6**	in/in ˚F$x10^{-6}$	**4.6**	Microns/m ˚C

Figure A13. Ultrafine Graphite Manufacturer Provided Data (*graphitestore.com*)